Non-perturbative lattice approaches to complex path integrals: from non-perturbative saddle points to real-time physics of chiral media

DISSERTATION

zur Erlangung des Doktorgrades der Naturwissenschaften (Dr. rer. nat.) der Fakultät für Physik der Universität Regensburg

vorgelegt von

Semen Valgushev

aus Ulyanovsk, Russland

Regensburg, Oktober 2018

Die Arbeit wurde von Dr. Pavel Buividovich angeleitet.

Das Promotionsgesuch wurde am 28.06.2017 eingereicht.
Das Promotionskolloquium fand am 04.12.2018 statt.

Prüfungsausschuss:

Vorsitzender:	Prof. Dr. Christoph Strunk
1. Gutachter:	Dr. Pavel Buividovich
2. Gutachter:	Prof. Dr. Vladimir Braun
weiterer Prüfer:	Prof. Dr. John Schliemann

Contents

Publications **5**

1 Introduction **9**
1.1 Goals 10
1.1.1 Asymptotically free theories and resurgence theory 10
1.1.2 The sign problem 13
1.1.3 Transport properties of chiral fermions and real-time simulations 13
1.2 Outline 15

2 Complex saddle points in two-dimensional gauge theory **17**
2.1 Introduction 17
2.2 Gross-Witten-Wadia (GWW) model 18
2.3 Complex Saddle Points in the GWW model 19
2.3.1 General features 20
2.3.2 Weak coupling phase 21
2.3.3 Phase transition and instanton condensation 23
2.3.4 Strong coupling phase 24
2.3.5 Spectrum of Gaussian fluctuations 27
2.4 Conclusions 30

3 Lattice study of adiabatic continuity conjecture in two-dimensional Principal Chiral Model **31**
3.1 Introduction 31
3.2 Simulation setup and observables 33
3.3 Periodic boundary conditions and the finite-temperature "deconfinement" transition 36
3.4 Twisted boundary conditions and the transition to Ünsal-Dunne regime . 39
3.5 Non-perturbative saddle points 41
3.6 Conclusions 48

4 Lefschetz thimbles and the sign problem in two-dimensional Hubbard model **51**
4.1 Introduction . . . 51
4.2 Basic definitions . . . 53
4.2.1 The model . . . 53
4.2.2 Lefschetz thimbles method . . . 58
4.2.3 Hybrid Monte Carlo and problems with ergodicity . . . 60
4.3 Lefschetz thimbles and Gaussian Hubbard-Stratonovich transformation . 62
4.3.1 Gaussian HS transformation with only complex exponents . . . 64
4.3.2 Gaussian HS transformation with only real exponents . . . 71
4.3.3 Gaussian HS transformation in mixed regime . . . 75
4.4 Results from test HMC simulations . . . 76
4.5 Non-Gaussian representation for the interaction term . . . 81
4.5.1 One-site Hubbard model . . . 81
4.5.2 Few-site Hubbard model . . . 87
4.6 Conclusions . . . 88

5 Overlap fermions in real-time lattice simulations of anomalous transport **91**
5.1 Introduction . . . 91
5.2 Anomalous transport of chiral fermions . . . 92
5.2.1 Chiral symmetry and Axial anomaly . . . 92
5.2.2 Chiral Magnetic Effect and anomalous transport . . . 95
5.3 Lattice fermions and problem of doublers . . . 98
5.3.1 Naive lattice fermions . . . 98
5.3.2 Wilson-Dirac fermions . . . 99
5.3.3 Overlap fermions . . . 100
5.4 Chirality pumping, Chiral Magnetic Wave and plasmon . . . 102
5.5 Lattice chiral fermions within the classical-statistical field theory approximation . . . 103
5.6 Comparison of numerical results from Wilson-Dirac and overlap fermions 105
5.7 Conclusions . . . 108

6 Conclusions **111**

I Appendix **115**

A Details of numerical study of two-dimensional lattice gauge theory **117**
A.1 Halley method . . . 117

Bibliography **119**

Publications

The list of publications related to this thesis is the following:

[1] P.V. Buividovich, Gerald V. Dunne, and S.N. Valgushev. "Complex Path Integrals and Saddles in Two-Dimensional Gauge Theory". *Phys. Rev. Lett.* 116 (2016), 132001. arXiv: 1505.04582.

[2] P.V. Buividovich, M. Puhr, and S.N. Valgushev. "Chiral magnetic conductivity in an interacting lattice model of parity-breaking Weyl semimetal". *Phys. Rev. B* 92 (2015), 205122. arXiv: 1505.04582.

[3] P.V. Buividovich and S.N. Valgushev. "Lattice study of continuity and finite-temperature transition in two-dimensional $SU(N) \times SU(N)$ Principal Chiral Model". *Submitted to Phys. Rev. D* (2017). arXiv: 1706.08954.

[4] M.V. Ulybyshev and S.N. Valgushev. "Path integral representation for the Hubbard model with reduced number of Lefschetz thimbles" (2017). arXiv: 1712.02188.

[5] P.V. Buividovich and S.N. Valgushev. "First experience with classical-statistical real-time simulations of anomalous transport with overlap fermions". *PoS LATTICE* (2016), 253. arXiv: 1611.05294.

[6] S.N. Valgushev, M. Puhr, and P.V. Buividovich. "Chiral Magnetic Effect in finite-size samples of parity-breaking Weyl semimetals". *PoS LATTICE* (2015), 043. arXiv: 1512.01405.

Acknowledgments

I would like to thank my supervisor Dr. Pavel Buividovich for giving me opportunity to work on exciting problems here, in Regensburg, and for guiding me.

Many thanks go to my wonderful colleagues Makism Ulybyshev, Oleg Kochetkov, Arthur Dromard, Matthias Puhr and Ali Davody. Creative and pleasant atmosphere of our group has always encouraged and inspired me.

I would like to especially thank Gerald Dunne for very exciting collaboration and his support. I am grateful to Mithat Unsal, Alexei Cherman, Tin Sulejmanpasic, Ariel Zhitnitsky, Dmitri Kharzeev, Edward Shuryak, Leonid Glozman, Alexander Turbiner, Victor Braguta and Andrey Kotov for very interesting and fruitful discussions.

I indebted to my brother and mother for their unconditional support and belief in me. Without their endless support this work would have never been done. I am also grateful to all my friends who stayed with me, encouraged me when things seemed gloomy and shared my bright days.

Chapter 1

Introduction

According to modern scientific knowledge, there are four types of force governing the matter in the Nature: electromagnetic, weak, strong and the gravity. Description of the first three ones is based on the principles of quantum field theory (QFT) and is summarized in a gauge theory known as the Standard Model. Physics of electromagnetic and weak forces is relatively well understood since in many physically important cases (but not in all) interactions are sufficiently weak such that one can use well-developed methods of perturbation theory. In the case of strong force situation is drastically different. Theory of strong force, the Quantum Chromodynamics (QCD), is non-Abelian gauge theory which is believed to describe rich phenomenology of hadrons (protons, neutrons, pions, etc.) and their interactions. The fact that gauge symmetry is non-Abelian implies that QCD is *asymptotically free* theory [1, 2]: interaction strength tends to vanish in the limit of very high energies. Thus theory becomes effectively free and some problems can be systematically studied with the help of perturbation theory in high energy regime. On the other hand, in the domain of low energy physics, which is in many respects the most interesting one, the coupling constant becomes large and standard perturbative approach is not applicable. Due to breakdown of perturbation theory which happens at the dynamically generated strong scale Λ, finding a reliable approach to such system is major theoretical problem nowadays.

Multiple experimental evidences such as Bjorken scaling in high energy collisions confirm asymptotically free nature of the strong force and physical existence of quarks and gluons in terms of which QCD Lagrangian is formulated. However, neither quarks nor gluons have ever been observed directly in experiments. The reason for that is that quarks are always confined inside hadrons (which are bound states in QCD) due to strong attractive force between them. This phenomenon is known as *confinement*. Observable properties of hadron spectra are consistent with existence of some sort of string stretched between quarks [3, 4], such that energy of the string growths with the distance and quarks cannot be separated apart. The tension of the string extracted from experimental data is

$\sqrt{\sigma} \approx 440\mathrm{MeV}$. The phenomenon of quark confinement cannot not be seen at any order of perturbation theory due to large characteristic distances comparable to typical hadron radius $r \sim 1\mathrm{fm}$ or, in other words, due to small involved momenta smaller that QCD strong scale $\Lambda_{\mathrm{QCD}} \sim 1\,\mathrm{GeV}$.

Due to strongly interacting nature of QCD properties of even lightest hadrons cannot be analytically calculated from the first principles. Since hadrons are basic excitations of strong interactions this causes serious difficulties in all spectrum of related phenomenological problems, ranging from high energy particle collisions and nuclear physics to astrophysics and cosmology. One of the most important is the problem of studying equation of state and phase diagram of hadronic matter at different temperatures, densities and pressure. This question is deeply related to the problem of confinement: when system of baryons and mesons is heated up to temperatures comparable to QCD strong scale $T_c \sim \Lambda_{\mathrm{QCD}}$ it undergoes a deconfinement phase transition after which hadrons "melt down" and quarks and gluons are liberated. This new state of matter is called Quark Gluon Plasma (QGP) which is a subject of intense experimental study in modern heavy ion collision experiments at RHIC and LHC, see [5, 6] for a review. Failure of perturbation theory in describing low energy physics is related to deconfinement phase transition: an appropriate choice of degrees of freedom for describing quarks confined in hadrons would be some sort of string-like collective excitations which bind them together whereas perturbation theory operates in terms of point-like quarks and gluons. Degrees of freedom undergo deep reorganization at the strong scale which is reflected in the presence of the phase transition.

1.1 Goals

This Thesis is an attempt to find a key, an approach, which would allow to understand details of strongly coupled dynamics of asymptotically free theories such as QCD. The source of our inspiration is the observation that non-perturbative phenomena and perturbative expansions are tightly related to each other in a very non-trivial way, so that a complete description of a quantum theory is only possible when both "sectors" are taken into account simultaneously. Such relations is a central subject of the *resurgence theory*. One of the leitmotifs of this theory is the appreciation of physically important role of unstable, non-topological and even complex saddle points of path integrals.

1.1.1 Asymptotically free theories and resurgence theory

Resurgence theory has recently provided new insights into matrix models and string theories [7–12], and has been applied to asymptotically free QFTs and sigma models [13–16], and localizable SUSY QFTs [17]. It appears that aforementioned classes of

saddle points are important for consistent semi-classical description of asymptotically free theories and in the most dramatic scenarios can even be responsible for phase transitions. Such saddles naturally appear in the semi-classical expansion in the framework of the *Lefschetz thimble decomposition* of the path integral [18, 19].

The Lefschetz thimbles decomposition can be obtained by deforming integration contour of the path integral into extended, complex space. Mathematical Morse theory, or Picard-Lefschetz theory, suggests that it is possible to construct such manifold in the complex plane that the path integral is decomposed as:

$$\mathcal{Z}(\lambda) = \sum_{\sigma} k_{\sigma}(\lambda)\, \mathcal{Z}_{\sigma}(\lambda), \tag{1.1}$$

$$\mathcal{Z}_{\sigma}(\lambda) = \int_{\mathcal{I}_{\sigma}(\lambda)} \mathcal{D}[x] e^{-S(\lambda,x)}, \tag{1.2}$$

where σ labels complex saddle points $z_{\sigma}(\lambda) \in \mathbb{C}$ of the action, coefficients $k_{\sigma}(\lambda) \in \mathbb{Z}$ are so-called intersection numbers and $\mathcal{I}_{\sigma}(\lambda)$ are real steepest descent manifolds, or Lefschetz thimbles, originating from σ-th saddle point. One can also define a dual real steepest ascend manifold, or anti-thimble $\mathcal{K}_{\sigma}$, which ends up at the given saddle point. With the help of anti-thimbles one can compute integer-valued coefficients k_{σ} in the expression (1.1) by counting the (oriented) number of intersection of $\mathcal{K}_{\sigma}$ with original integration contour of the path integral. Due to to the fact that imaginary part of the action is constant on both thimble and anti-thimble, one can consider Lefschetz thimbles decomposition as a multi-dimensional generalization of the stationary phase method.

We note that all quantities in the equation (1.1) depend non-trivially on parameters λ. Moreover, the structure of thimbles $\mathcal{I}_{\sigma}$ and anti-thimbles $\mathcal{K}_{\sigma}$ can significantly change as λ is varied, so that Stokes phases are correctly taken into account. In particular, intersection numbers k_{σ} can jump due to movement of anti-thimbles, so that some thimble integrals will appear and some will disappear from the sum (1.1). This is a non-trivial topological manifestation of the fact that contributions of different saddle points are related to each other due to monodromy properties of the path integral as integration runs around singularities.

The connection of non-perturbative saddle points discussed above is reflected in the structure of asymptotic perturbative expansion. Resurgence theory generalizes ordinary perturbative series in powers of some small parameter g^2 to resurgent *trans-series*:

$$\langle\, \mathcal{O} \,\rangle = \sum_{n=0}^{\infty} F_{n,0}^{(0)} g^{2n} + \sum_{n=0}^{\infty} \sum_{k=1}^{\infty} \sum_{l=1}^{k-1} F_{n,l}^{(k)} g^{2n} \left(\exp\left[-\frac{A}{g^2} \right] \right)^k \left(\ln\left[\pm \frac{1}{g^2} \right] \right)^l, \tag{1.3}$$

where exponential factors take into account non-perturbative effects, logarithms take into account contributions of quasi-zero modes and corresponding power series of g^2 describe local quantum fluctuations about the k-th saddle point. Trans-series are called resurgent since the object which is represented by such series "surges up", or resurrects, due to

mechanism of Brezin-Zinn-Justin (BZJ) ambiguity cancellation: Borel resummation of perturbative series about vacuum or k-th saddle point often requires careful regularization due to appearing poles, especially in asymptotically free theories. Regularization, however, leads to exponentially small ambiguities (since poles can be by-passed from below or above), which are exactly cancelled by certain non-perturbative amplitudes, e.g. due to instanton-anti-instanton transitions, which also become ambiguous when regularization is applied. Thus, resulting resummed expression appears well-defined and at the same time takes into account both perturbative and non-perturbative phenomena.

The structure of BZJ cancellation implies that expansion coefficient $F^{(k)}_{n,l}$ are highly correlated and that perturbative series actually contains important information about non-perturbative physics. This information is particularly encoded in the location and residues of the aforementioned poles. The most well known example of such pole is *infrared renormalon* in non-Abelian gauge theory [20–28], see also review [29]. The renormalon appears if one tries to resum important class of Feynman diagrams, so-called "bubble chains", which take into account effect of the running coupling (thus, renormalon is related to renormalization). It is believed that infrared renormalon is tightly related to non-perturbative physics responsible for mass gap generation in non-Abelian gauge theory [20–28].

A complete study of resurgent relations of perturbative and non-perturbative physics is only possible for systems where one can compute any term of the expansion and/or find all saddle points and Lefschetz thimbles. Unfortunately, only very limited information is available in realistic theories. An important step towards realistic systems can be made with the help of special deformations which could bring asymptotically free theory from strongly coupled into weakly coupled regime in a controllable way. For instance, one can make one spatial direction compact and impose specific boundary conditions, so-called Z_N-symmetric twist [14–16, 30, 31]. When the size of compact direction is large, effect of the twist should be negligible, whereas at very small size the theory should become weakly coupled due to asymptotic freedom. The purpose of the twist is to suppress possible phase transition from confined into deconfined phase as the size L of the compact direction is varied from large to small values. If this phase transition is suppressed, then one can perform computations in weakly coupled regime at small L and after analytically continue them into strongly coupled regime at large L. The conjecture that deconfinement phase transition is suppressed is called *adiabatic continuity conjecture*. It is important to study this conjecture since it is a cornerstone ingredient for resurgence studies of two dimensional asymptotically free models where one can find interpretation of renormalon divergence in terms of (unstable) saddle points, which at the same time are responsible for the mass gap generation [14–16, 30, 31]. It is also very important in the light of recent program of applying similar ideas directly to Yang-Mills theory and QCD [32, 33].

In this Thesis we investigate the physical role of non-pertubative phenomena in several problems in the context of resurgence theory. To this end we employ lattice field theory for regularization of the path integrals which allows us to obtain results from first principles with the help of numerical Monte-Carlo simulations and to consider phenomena which cannot be tested by other means.

1.1.2 The sign problem

We are also interested in studying physical origins of so-called *sign problem* in Monte-Carlo simulations: numerical simulations are based on algorithms of importance sampling where field configurations are generated randomly according to distribution given by the Boltzmann weight e^{-S} in the path integral. It is crucial that the action S is real, so that Boltzmann weight can be interpreted as probability density function. However, this is not the case if a system with fermions is considered at the finite chemical potential since fermionic effective action becomes complex with highly oscillating phase. Because of the sign problem it is very challenging to study the phase diagram of QCD at finite density, see reviews [34, 35]. Since the problem affects basically any physical systems with fermions at finite density, we choose two dimensional Hubbard model [36, 37] which is physically very interesting and, at the same time, allows to simplify analysis compared to QCD. It can serve as a model of high-temperature superconductor where superconducting phase is expected to exist at large values of chemical potential [38–40]. In our work we explore an approach to the sign problem based on Lefschetz thimble decomposition. The idea is motivated by the fact that imaginary part of the action is constant on the thimble manifold, thus partition function is given by a sum of integrals each of which can, in principle, be approached by standard Monte-Carlo techniques.

1.1.3 Transport properties of chiral fermions and real-time simulations

Finally, we are interested in studying novel transport phenomena appearing in systems with chiral fermions due to presence of quantum axial anomaly. The axial anomaly, or Adler-Bell-Jackiw (ABJ) anomaly [41, 42], is probably one of the best know ways to relate perturbative and non-perturbative physics:

$$\partial_\mu j_5^\mu = -\frac{N_f}{16\pi^2} F_{\mu\nu}\tilde{F}^{\mu\nu}, \tag{1.4}$$

where $j_5^\mu = \bar{\psi}\gamma^\mu\gamma^5\psi$ is axial current, $F_{\mu\nu} = \partial_\mu A_\nu - \partial_\nu A_\mu$ is the stress-tensor of a (non-Abelian) background gauge field, $\tilde{F}^{\mu\nu} = \frac{1}{2}\epsilon^{\mu\nu\alpha\beta}F_{\alpha\beta}$ is a dual stress-tensor and N_f is number of fermion flavors ($N_f = 3$ in QCD). On the one hand, this equation is exact perturbative result [43]. On the other hand, in the case of non-Abelian gauge theory the

quantity of the r.h.s. of this equation is a total derivative of topological Chern-Simons current K^μ, so that the change of the fermionic axial charge over time ΔQ_5 is related to topological Chern-Simons number $Q_{CS} = \frac{N_f}{32\pi^2}\int \mathrm{d}^4x\, \partial_\mu K^\mu$ of gauge fields:

$$\Delta Q_5 = 2Q_{CS}. \tag{1.5}$$

Thus, in non-Abelian gauge theory fermionic currents reveal non-trivial topological properties of the vacuum. However, even in Abelian case it can have far going consequences.

Axial anomaly drives unusual dissipation-less transport which is often referred to as *anomalous transport*. These effects have multiple manifestations in rich variety of situations ranging from particle [44–46] and condensed matter physics [47–49] to processes in astrophysics and at cosmological level [50–54]. It appears in media which violate P and CP symmetries in one of the possible ways: e.g. one can consider a medium with different number of left and right handed fermions, or consider non-Abelian gauge theory where spaleron transitions can induce local fluctuations of axial charge. A combination of such medium and external magnetic field gives rise to Chiral Magnetic Effect (CME) [45]:

$$\mathbf{j} = \sigma_{CME}\mathbf{B}, \tag{1.6}$$

where $\mathbf{j}$ is electric current and σ_{CME} is so-called chiral magnetic conductivity which is supposedly protected from renormalization due to tight connection to the axial anomaly. In particular, since nuclei in heavy-ion collisions can create very large magnetic fields $eB \sim m_\pi^2$ [55] at the first moments of collision, CME can lead to detectable fluctuations of electric charge asymmetry.

In order to describe anomalous transport it is necessary, however, to go beyond traditional equilibrium paradigm. It is by now commonly accepted that anomalous transport phenomena cannot exist in equilibrium [56], and moreover, at certain circumstances axial anomaly and CME can even drive so-called Chiral Plasma Instability [57] which is expected to play important role in astrophysics and cosmology. Also, in the case of heavy ion collision experiments the expected life-time of strong magnetic field, which is the moment when anomalous effects receive main contributions, is so short ($t \approx 1 fm/c$ [55]) that it poses a question whether quark gluon plasma really succeeds to thermalize within such a short time [58].

Real-time problems are notoriously difficult. From the point of view of first principle numerical computations, they represent an extreme case of the sign problem which can be addressed only on future quantum computers. At the present moment, it is necessary to employ simplifying approximations in order to address realistic problems. In the present work, we use so-called *classical-statistical field theory* (CSFT) approximation, which helps to capture essential non-perturbative effects such as particle pair production, combined with lattice field theory for studying anomalous transport properties of chiral

fermions in non-stationary environment. We are especially interested in studying the performance of overlap fermions, which realize exact lattice chiral symmetry, in real-time simulations.

1.2 Outline

The rest of the thesis is organized as follows:

- In the Chapter 2 we study saddle points structure of two-dimensional lattice gauge theory represented as Gross-Witten-Wadia (GWW) unitary matrix model in the context of the resurgence theory. We express the path integral in terms of fields analytically continued into complex plane in order to explore the physical role of complex saddle points. In the weak coupling phase, we confirm a conventional mechanism of instanton gas condensation which drives the 3rd-order $N = \infty$ phase transition from weak to strong coupling regime. In the strong coupling phase we find a new interpretation of non-perturbative effects in terms of complex saddle points which are obtained by "eigenvalues tunneling" into complex plane. The action of these new saddle points matches predictions of the resurgence theory analysis of the $1/N$ expansion of the free energy.

- In the Chapter 3 we study two-dimensional $SU(N) \times SU(N)$ Principal Chiral Model (PCM) using first-principle lattice simulations. PCM is a confining asymptotically free quantum field theory which can be considered as a toy model of QCD. We explore the validity of adiabatic continuity conjecture and effect of Z_N-symmetric twist on the phase structure and non-perturbative features of PCM. In our work we use lattices of the size $L_0 \times L_1$, where the twist is imposed on the 0-th direction. We compare our result to simulations of PCM with periodic boundary conditions where L_0 can be considered as inverse temperature. For both boundary conditions our numerical results can be interpreted as signatures of a weak crossover or phase transition at $N = \infty$ between the regimes of small and large L_0. In particular, at small L_0 thermodynamic quantities exhibit nontrivial dependence on L_0, and the static correlation length exhibits a weak enhancement at some "critical" value of L_0. We also observe important differences between the two boundary conditions, which indicate that the transition scenario is more likely in the periodic case than in the twisted one. In particular, the enhancement of correlation length for periodic boundary conditions becomes more pronounced at large N, and practically does not depend on N for twisted boundary conditions. Furthermore, using Gradient Flow we study non-perturbative physics of the theory and find that enhancement of the correlation length appears when the length L_0 becomes comparable with the typical size of unitons, unstable non-topological non-

perturbative saddle points of PCM. With twisted boundary conditions these saddle points become effectively stable and one-dimensional in the regime of small NL_0, whereas at large NL_0 they are very similar to the two-dimensional unitons with periodic boundary conditions. In the context of adiabatic continuity conjecture for PCM with twisted boundary conditions, our results suggest that while the effect of the compactification is clearly different for different boundary conditions, one still cannot exclude the possibility of a weak crossover separating the strong-coupling regime at large NL_0 and so-called Dunne-Ünsal regime at small NL_0 with twisted boundary conditions.

- In the Chapter 4 we study the sign problem in two-dimensional Hubbard model at non-zero chemical potential (away from half-filling regime) through the prism of Lefschetz thimble decomposition of the path integral. In this approach the sign problem can be reduced if partition function can be represented as a sum over Lefschetz thimbles with only a few different global phases. We explore the complexity of the sign problem in the few-site Hubbard model on square lattice with the help of semi-analytical study of saddle points and corresponding Lefschetz thimbles. Due to complexity of the problem, we employ small lattices with several steps in the direction of imaginary Euclidean time. We study different variants of the Hubbard-Stratonovich transformation of the interaction term and find representation where a minimal number of thimbles contribute to the partition function in the vicinity of half-filling: there are only two relevant thimbles on few-site lattice in this regime. We also find indirect evidence that this regime can exist in more realistic systems with large sizes. Finally, we derive a novel non-Gaussian representation of the interaction term, where the number of relevant Lefschetz thimbles is significantly reduced in comparison to conventional Gaussian Hubbard-Stratonovich transformation.

- In the Chapter 5 we present first results of classical-statistical real-time simulations of transport phenomena of chiral fermions modelled by overlap fermions. We find that even on small lattices overlap fermions reproduce the real-time anomaly equation with much better precision than Wilson-Dirac fermions on significantly bigger lattices. The difference becomes much more pronounced for quickly changing electromagnetic fields, especially if one takes into account the back-reaction of fermions on electromagnetic fields. As test cases, we consider chirality pumping in parallel electric and magnetic fields and mixing between the plasmon and the Chiral Magnetic Wave.

Chapter 2

Complex saddle points in two-dimensional gauge theory

2.1 Introduction

In gauge theories, there are two physical parameters which control the strength of fluctuations around the saddle points and enter the resurgent trans-series expansion: the rank N of the gauge group and the t'Hooft coupling $\lambda \equiv Ng^2$, with gauge coupling g^2 [59]. The interplay between the dependence on N and λ leads to novel effects [7, 8, 12] which we explore here. An important goal would be to construct uniform resurgent approximations [60] (with respect to λ and $1/N$) which analytically relate the weak and strong coupling phases. For gauge theories, such a relation would certainly improve our understanding of confinement and dynamical mass gap generation. It would also extend the applicability of Diagrammatic Monte-Carlo studies of non-Abelian lattice gauge theories, which are so far limited to the regime of unphysically strong bare coupling constants [61].

The difference between weak and strong coupling phases is particularly dramatic in the large-N limit of 2D gauge theories, where they are separated by a third-order phase transition with respect to the t'Hooft coupling λ [62–65] and/or the manifold area A [66, 67]. Physically, on the weak coupling side this large-N phase transition in 2D gauge theory is related to the condensation of instantons [65, 67, 68], which are exponentially suppressed at large N away from the transition point. Much less is known about the role of instantons (or other saddles) on the strong coupling side of this transition, except in the double scaling limit. Here we study the simplest example of 2D lattice gauge theory, the Gross-Witten-Wadia unitary matrix model [62–64], to demonstrate the novel properties of complex saddles in the strong coupling phase as well as their relation to the resurgent structure of the $1/N$ expansion.

2.2 Gross-Witten-Wadia (GWW) model

Gross-Witten-Wadia (GWW) model [62, 63] is a matrix model representation of two-dimensional $U(N)$ lattice gauge theory which is given by standard action:

$$S_{lat} = \frac{1}{g^2}\sum_x \mathrm{Tr}\, P_x, \qquad P_x = U_{x,0}U_{x+e_0,1}U^\dagger_{x+e_1,0}U^\dagger_{x,1}, \tag{2.1}$$

where $U_{x,\mu} \in U(N)$ are lattice gauge fields, P_x is a plaquette operator and e_μ is a unit lattice vector in direction $\mu = 0, 1$. In order to derive partiton function of the GWW model one can use gauge freedom and choose axial gauge in which fields in direction $\mu = 0$ are all equal to identity $U_{x,0} = 1$, so that lattice action becomes $S_{lat} = 1/g^2 \sum\limits_x \mathrm{Tr}\,[U_{x,1}U^\dagger_{x+e_0,1}]$. With the help of invariance of the Haar measure of the lattice path integral with respect to shifts $\mathrm{d}[U] = \mathrm{d}[WU]$, where $W \in U(N)$, one can make a change of variables:

$$U_{x+e_0,1} = W_x U_{x,1}, \tag{2.2}$$

after which the partition function of the $2D$ lattice gauge theory takes a simple form:

$$\begin{aligned}\mathcal{Z}_{lat} &= \int \prod_x \mathrm{d}[U_{x,1}]\, e^{-S_{lat}} = \\ &= \int \prod_x \mathrm{d}[W_x] \exp\left(-\frac{N}{\lambda}\mathrm{Tr}\,[W_x + W_x^\dagger]\right),\end{aligned} \tag{2.3}$$

where $\lambda = Ng^2$ is t'Hooft coupling. Hence, partition function factorizes: $\mathcal{Z}_{lat} = \mathcal{Z}^V$, where V is lattice volume and $\mathcal{Z}$ is desired partition function of the GWW matrix model:

$$\mathcal{Z} = \int \mathrm{d}[W] \exp\left(-\frac{N}{\lambda}\mathrm{Tr}\,[W + W^\dagger]\right). \tag{2.4}$$

Thus, all properties of two-dimensional lattice gauge theory can be obtained from a GWW matrix model.

Partition function (2.4) can be expressed in terms of phases z_i of eigenvalues e^{iz_i} of unitary $N \times N$ matrix W:

$$\begin{aligned}&\mathcal{Z} = \prod_{i=1}^N \int_{-\pi}^{\pi} \mathrm{d}z_i\, e^{-S(z_i)}, \qquad S(z_i) = \sum_i V(z_i) - \ln \Delta^2(z_i), \\ &V(z) = -\frac{2N}{\lambda}\cos(z), \qquad \Delta(z_i) = \prod_{i<j} \sin\left(\frac{z_i - z_j}{2}\right).\end{aligned} \tag{2.5}$$

We are interested in the t'Hooft limit: $N \to \infty$, $g^2 \to 0$ while $\lambda = Ng^2$ is kept fixed. In this limit one can introduce normalized density of eigenvalues $\rho(z)$ defined on the unit circle $\mathrm{Re}\, z \in [-\pi,\ \pi)$, $\mathrm{Im}\, z = 0$:

$$N\rho(z)\mathrm{d}z = \mathrm{d}n, \qquad \int_{-\pi}^{\pi} \rho(z)\,\mathrm{d}z = 1, \tag{2.6}$$

where $\mathrm{d}n$ is number of eigenvalues in the segment $[z, z+\mathrm{d}z]$. The action (2.5) is expressed in terms of $\rho(z)$ as:

$$\frac{S}{N^2} = \frac{2}{\lambda}\int\limits_{-\pi}^{\pi} \mathrm{d}z\, \rho(z)\cos(z) - \\ -\frac{1}{2}P.V.\int\limits_{-\pi}^{\pi}\mathrm{d}z\int\limits_{-\pi}^{\pi}\mathrm{d}z'\,\rho(z)\rho(z')\ln\left[\sin^2\left(\frac{z-z'}{2}\right)\right], \tag{2.7}$$

where $P.V.$ refers to Cauchy principle value of the integral. It is clear that one can use N^2 as large parameter and perform saddle point analysis of the path integral. Leading saddle point contribution would correspond to planar limit of the $1/N$ expansion.

At $N=\infty$ this model has a third-order phase transition at $\lambda_c = 2$, where the third derivative of the free energy is discontinuous [62, 63]. In order to see this one can consider saddle points of the least action (vacuum fields) given by the following expressions [62, 63]:

$$\rho^{(w)}(z) = \frac{2}{\lambda\pi}\cos\left(\frac{z}{2}\right)\sqrt{\frac{\lambda}{2}-\sin^2\left(\frac{z}{2}\right)}, \qquad \lambda < 2 \tag{2.8}$$

$$\rho^{(s)}(z) = \frac{1}{2\pi}\left(1+\frac{2}{\lambda}\cos(z)\right), \qquad \lambda > 2. \tag{2.9}$$

In the weak coupling phase $\lambda < 2$ the distribution $\rho^{(w)}(z)$ has a support on semi-circle $z \in [-z_c, z_c]$, where z_c is a solution to the equation $\sin^2(z/2) = \lambda/2$. Hence there is gap in the distribution so that eigenvalues do not occupy the whole unit circle. However, at the critical point $\lambda = \lambda_c$ the gap in the distribution closes and eigenvalues can occupy any point of the unit circle in the strong coupling phase $\lambda > 2$. Explicit computation of the leading saddle point contribution yields the following result for the planar free energy:

$$E_0(\lambda) = -\ln \mathcal{Z}/N^2 = \\ = \begin{cases} \frac{1}{\lambda^2}, & \lambda > 2, \\ \frac{2}{\lambda} + \frac{1}{2}\ln\frac{\lambda}{2} - \frac{3}{4}, & \lambda < 2 \end{cases}. \tag{2.10}$$

Third derivative of $E_0(\lambda)$ is discontinuous at $\lambda_c = 2$, hence there is a phase transition of the third order.

2.3 Complex Saddle Points in the GWW model

In this Section we study saddle points of GWW model in the complex plane. In order to find saddle configurations with *a priori* unknown properties we numerically solve saddle point equations at large but finite N:

$$\frac{\partial S}{\partial z_i} = 0, \tag{2.11}$$

where $z_i \in \mathbb{C}$. Complex eigenvalues can be visualized on the cylinder $S^1 \times \mathbb{R}$, where S^1 is the original unit circle and $\mathbb{R}$ is the imaginary direction.

Since the action $S(z)$ of the GWW model is a holomorphic function of eigenvalues z_i, equations (2.11) can be solved with the help of e.g. Newton iterations. However, in our case the Newton iterations turned out to be unstable in the strong coupling phase for N larger than certain value $N > 20$. Because of that, we employed the Halley method which is next-order improvement of Newton iterations. We describe it in the Appendix A.1. Using this method we were able to solve the saddle-point equations for the values of N up to $N = 400$. As initial conditions for the Halley iterations we chose values $z_i^{(0)}$ randomly distributed in the rectangle $\mathrm{Re}\, z_i \in [-\pi,\ \pi)$, $\mathrm{Im}\, z_i \in [-5.0, 5.0]$, which yielded sufficiently many distinct solutions. We distinguish solutions up to the obvious symmetry of arbitrary permutations of eigenvalues z_i.

2.3.1 General features

We find that all saddle points consist of $(N - m)$ real eigenvalues located on the unit circle $\mathrm{Re}\, z \in [-\pi,\ \pi)$, $\mathrm{Im}\, z = 0$, whereas m eigenvalues reside on the line $z = \pi + iy$, $y \in \mathbb{R}$. We note that both the unit circle and the second complex line are the steepest ascent contours of the potential $V(z)$ originating from its extrema at $z = 0$ and $z = \pi$. The configurations of z_i are all symmetric with respect to these points. Hence, when m is odd there is always one eigenvalue located exactly at $z = \pi$. Some illustrative examples of found saddle points are presented on the Fig. 2.1 for different values of λ and m.

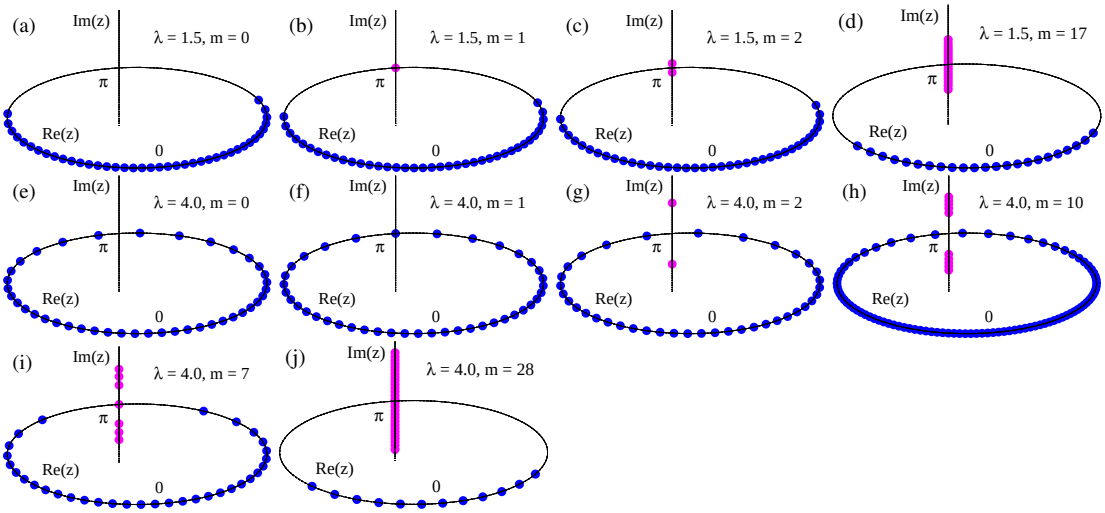

Figure 2.1: Saddle point configurations of eigenvalues z_i in the weak-coupling (plots (a) - (d)), and in the strong-coupling (plots (e) - (j)) phases with different "instanton numbers" m. $N = 40$ on all of the plots except for the plot (h), where we take $N = 100$ in order to illustrate the three-cut solution at large m and strong coupling.

We have checked that in both weak and strong coupled phases the saddle points with $m = 0$ correctly reproduce known results for the planar (vacuum) distribution of

eigenvalues (2.8, 2.9). We present numerical eigenvalue distribution at sufficiently large $N = 400$ compared to theoretical results on the Fig. 2.2 for few values of λ from both phases. Hence, we observe a phenomenon of vanishing gap in the eigenvalue distribution at the critical point $\lambda_c = 2$ which drives the $N = \infty$ phase transition.

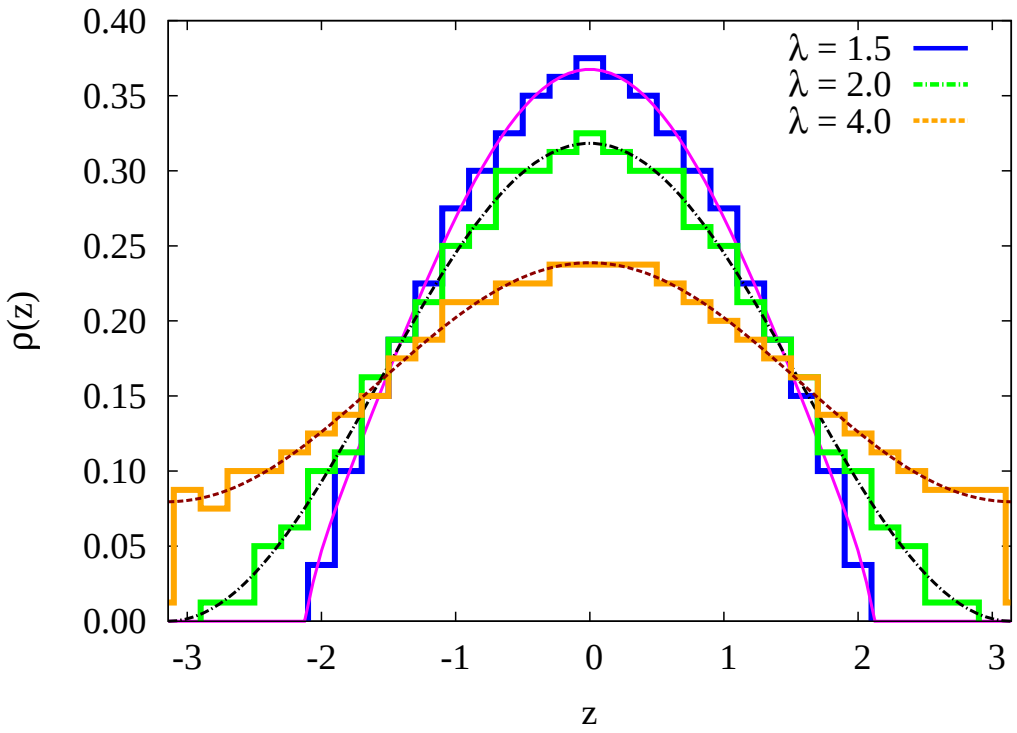

Figure 2.2: Numerical eigenvalue distributions for the $m = 0$ saddle [$N = 400$], compared with the analytic $\rho(z)$ in (2.8, 2.9).

The real part of the action of saddle points is illustrated on the Fig. 2.3 as a function of m for several representative values of λ from both phases. The imaginary part of the action is always a multiple of π:

$$\mathrm{Im}\, S(z) = \pi \lfloor m/2 \rfloor, \tag{2.12}$$

where $\lfloor \cdot \rfloor$ is the floor function. Thus, saddle point contributions e^{-S_m} to the path integral are always real, either positive or negative, although eigenvalues are manifestly complex. This phenomenon can be interpreted as a hidden topological angle [69]. We note that it has the origin in the Vandermonde determinant $\Delta^2(z)$.

2.3.2 Weak coupling phase

The leading non-perturbative saddle point at $\lambda < 2$ is the one with $m = 1$. It can be obtained from the vacuum field configuration by dragging one eigenvalue from the support of the $\rho(z)$ to the point $z = \pi$, as depicted on the Fig. 2.1(b). The action of this saddle, relative to the action of the vacuum $m = 0$, can be obtained analytically [8] with the help of the following electrostatic analogy: all eigenvalues can be though as electric

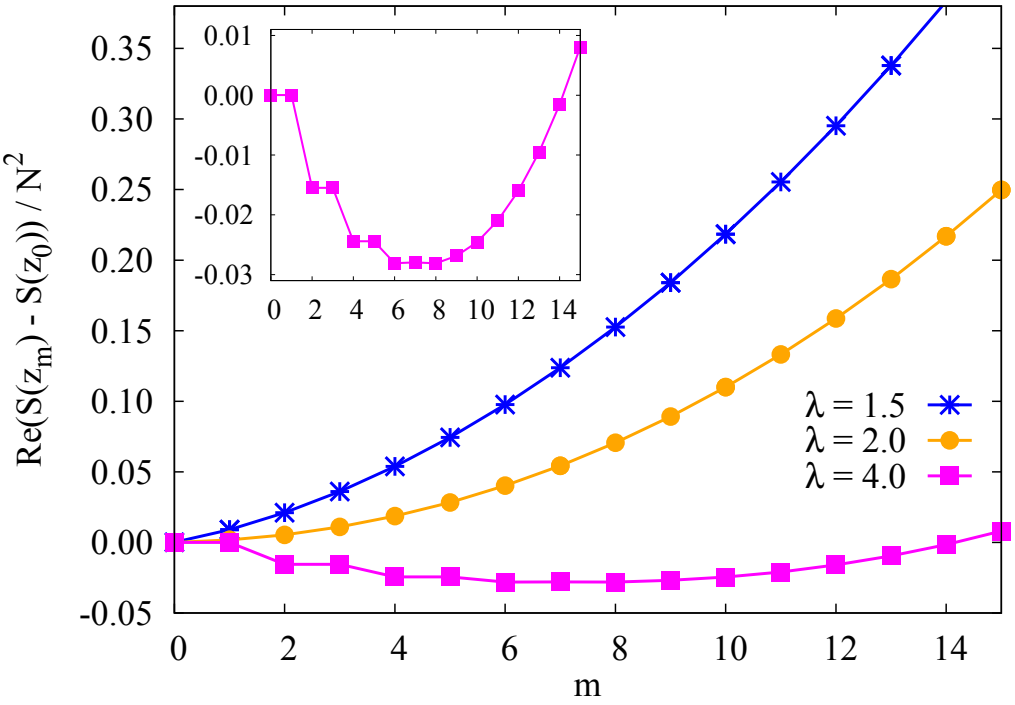

Figure 2.3: Real part of the saddle action, $\mathrm{Re}\, S\,(z)$, versus instanton number m, for different values of λ, at $N = 40$. The inset shows $\mathrm{Re}\, S\,(z)$ vs m at $\lambda = 4$ on a larger scale.

charges placed in the external potential $V(z)$ and repelling each other according to the Vandermonde term $\ln \Delta^2\,(z)$ in the action. One can compute the work needed to move a single charge from the support of $\rho(z)$ to the point $z = \pi$ in the background of the self-consisted electric field created by all other eigenvalues. The resulting $N = \infty$ action is the following:

$$S_I^{(w)} = 4/\lambda\sqrt{1-\lambda/2} - \mathrm{arccosh}\,((4-\lambda)/\lambda)\,, \qquad \lambda < 2. \tag{2.13}$$

We depict numerical action of $m = 1$ saddle at $N = 400$ compared to theoretical result on the Fig. 2.4. We observe a good agreement.

For larger $m > 1$ eigenvalues go into complex plane and arrange themselves along the line $z = \pi + iy$ symmetrically with respect to the point $z = \pi$, see Fig. 2.1(c,d). We interpret this result as "eigenvalue tunneling" where tunneled eigenvalues are complex. As N increases, eigenvalues clearly tend to form a cut.

We note that in the vicinity of the critical point $\lambda \to \lambda_c$ the real part of the action of saddle points with sufficiently small $m \ll N$ scale approximately linearly with m: $\mathrm{Re}\,(S_m - S_0) = m\,N\,S_I^{(w)}$. Thus, one can identify m as number of weakly interacting "instantons" (it is common to refer to such non-perturbative saddle points as instantons). Hence we confirm a conventional picture of dilute instanton gas in the weak coupling phase.

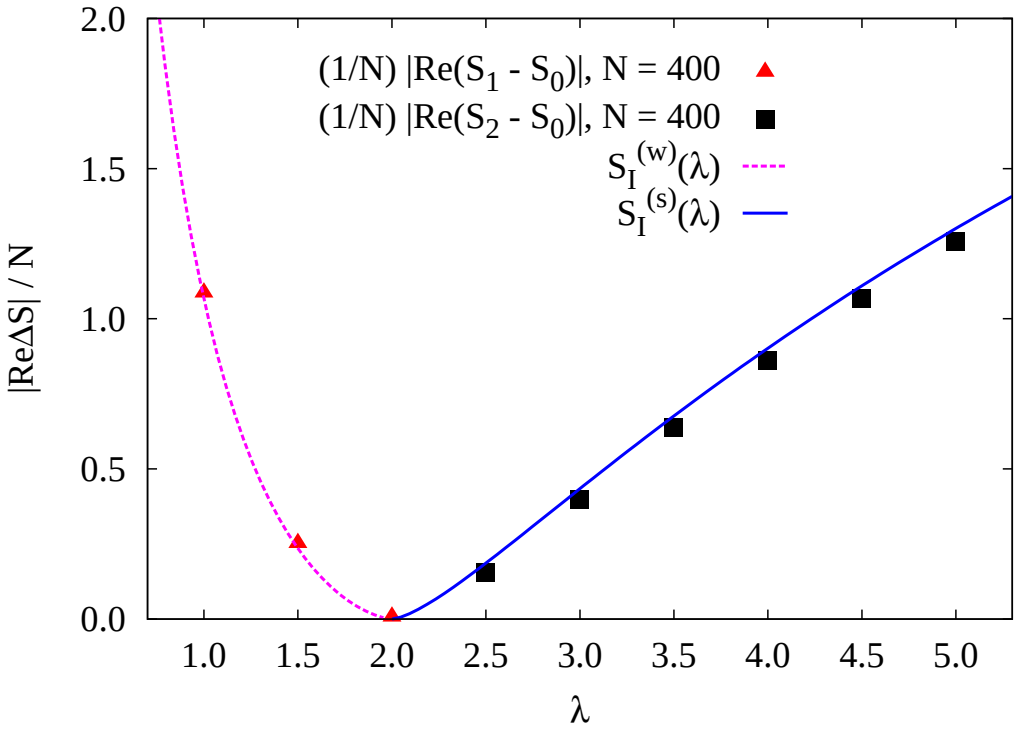

Figure 2.4: Numerical results (dots) for the relative actions of the leading non-vacuum saddles with $m = 1$ (in the weak-coupling phase) and $m = 2$ (in the strong-coupling phase), at $N = 400$. Solid lines are the analytic expressions (2.13) and (2.15).

We also study the spectrum of the Hessian matrix:

$$H_{m,ij} = \frac{\partial^2 S_m}{\partial z_i \, \partial z_j}, \tag{2.14}$$

which describe Gaussian fluctuations about the m-th saddle point. We consider its properties in details in the Subsection 2.3.5. In particular, we find that in the weak coupling regime it has exactly m negative eigenvalues for the m-th saddle point, thus the $m = 1$ saddle point give an imaginary contribution to the saddle point expansion of the free energy. This imaginary contribution is cancelled by imaginary term from the Borel summation of divergent $1/N$ expansion about the $m = 0$ vacuum saddle point. Thus, we observe a clear indication of resurgent cancellations. This can be traced to the resurgent asymptotics of individual Bessel functions, using the determinant representation [62, 63] of the partition function: $\mathcal{Z} = \det\left(I_{j-k}(2N/\lambda)\right)$.

2.3.3 Phase transition and instanton condensation

As $\lambda \to 2$ from the weak-coupling side, the gap in the eigenvalue distribution closes at the point $z = \pi$, see Fig. 2.1 and Fig. 2.2. Furthermore, as seen on the Fig. 2.3, the real part of the saddle action, relative to the vacuum value, tends to zero, so that all instantons with $m \ll N$ become equally important at the transition point, signaling instanton condensation [8, 65, 67].

2.3.4 Strong coupling phase

In the strong coupling phase $\lambda > 2$ the gap in the eigenvalue distribution is closed and the point $z = \pi$ is already in the support of $\rho^{(s)}(z)$. Because of that, non-vacuum saddles can no longer be constructed by dragging eigenvalues to $z = \pi$ as it was possible in the weak coupling phase. Nevertheless, Mariño obtained the following strong-coupling "instanton action" using a trans-series ansatz in the string equation [8] (see also Appendix B in [70]):

$$S_I^{(s)} = 2\text{arccosh}\,(\lambda/2) - 2\sqrt{1 - 4/\lambda^2}, \quad \lambda \geq 2. \tag{2.15}$$

We find a natural interpretation of this "instanton" as a saddle configuration, with complex eigenvalue tunneling from the real to the imaginary axis (see Fig. 2.1). As in the weak coupling phase, m eigenvalues line up along the imaginary direction, but these strong-coupling saddles have some surprising properties.

Quasi-zero mode

First of all, we find that at large N, the $m = 1$ saddle point has real action which differ from that of the $m = 0$ saddle up to exponentially small corrections precisely of the form:

$$\text{Re}\ (S_1 - S_0) \sim \exp\Big(-N/2\, S_I^{(s)}\Big), \tag{2.16}$$

where $S_I^{(s)}(\lambda)$ is the strong-coupling instanton action (2.15). We depict this difference on the Fig. 2.5. Physically, this is due to quasi-zero mode which emerge in the strong-coupling regime: in the limit $\lambda \to \infty$ the potential $V(z)$ becomes irrelevant and saddle point configuration is determined solely by the Vandermonde term $\ln \Delta^2(z)$ in the action (2.5). This term has an extra global $U(1)$ symmetry: all eigenvalues can be rotated by an arbitrary angle simultaneously. The quasi-zero mode is an remnant of this extra symmetry at finite values of $\lambda > 2$, so that eigenvalue medium on the unit circle can support some sort of collective "sound wave".

Because of the quasi-zero mode, the $m = 0$ and $m = 1$ configurations can be transformed into each other by the shift in the flat direction, so that they have the same continuous eigenvalue density, but microscopically differ by the presence or absence of a single eigenvalue at $z = \pi$, see Fig. 2.1, (e) and (f). The shift moves every eigenvalue to the middle of the interval to its neighboring eigenvalue. At large N this interval is inversely proportional to the density function $\rho^{(s)}(z)$, so that flat direction is given by:

$$\delta z_i \sim \frac{1}{\rho^{(s)}(z_i)}. \tag{2.17}$$

Direct substitution of this expression into the integral equation for eigenvectors of the Hessian matrix (2.14) yields that δz is indeed an eigenvector with zero eigenvalue at

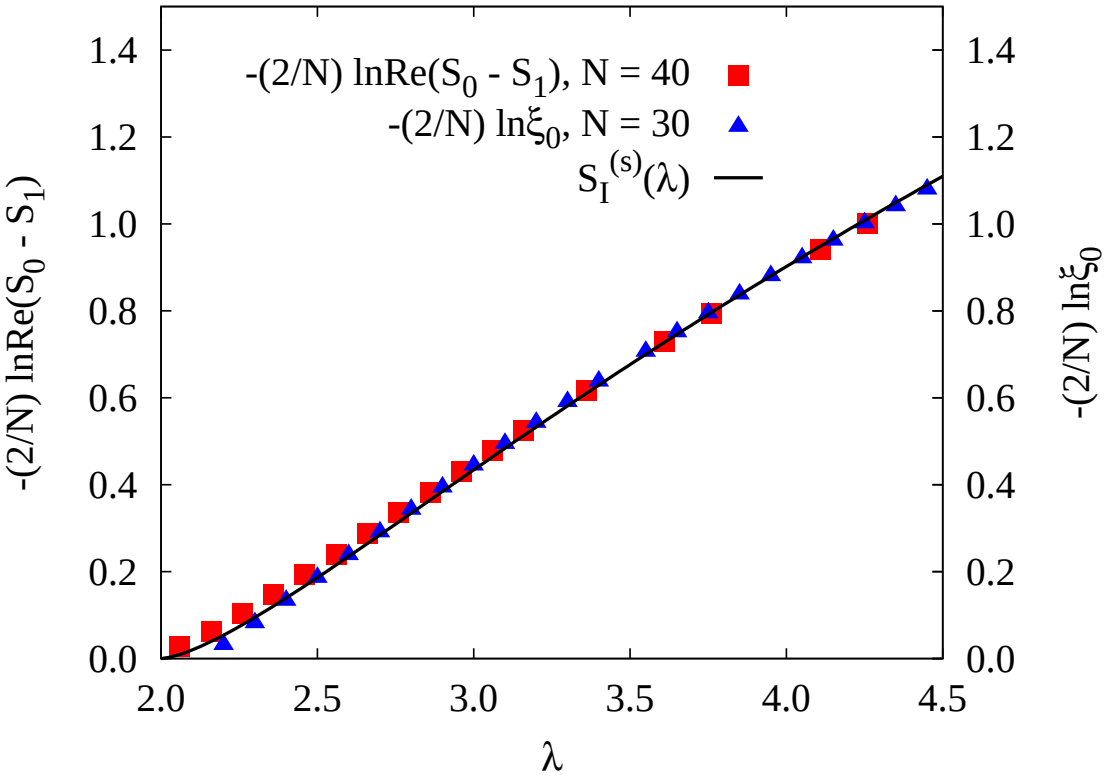

Figure 2.5: Comparison of the log of the difference between the actions of the $m = 0$ and $m = 1$ saddles (left vertical axis), and the log of the lowest Hessian eigenvalue ξ_0 (right vertical axis), in the strong coupling phase, with half the strong coupling instanton action in (2.15). Both effects are governed by the same exponential.

$N = \infty$:

$$[H\delta z](z) = -\frac{2}{\lambda}\cos(z)\,\delta z(z) - P.V.\int_{-\pi}^{\pi} \mathrm{d}z'\rho^{(s)}(z')\,\frac{\delta z(z) - \delta z(z')}{\sin^2\left(\frac{z-z'}{2}\right)} = 0, \qquad (2.18)$$

where H is the Hessian operator and $P.V.$ refers to the Cauchy principal value of the integral. Note that since $\delta z(z)$ is analytic for $z \in [-\pi, \pi]$, the integrand in the second term on the right-hand side of (2.18) diverges only as $1/z$ rather than $1/z^2$, thus the integral is well defined in the sense of Cauchy principal value.

Furthermore, we numerically compute eigenvector δz which correspond to the lowest eigenvalue ξ_0 of the Hessian at large but finite $N = 400$. On the Fig. 2.6 we demonstrate a good agreement between the numerical and theoretical result (2.17). We also find that as $N \to \infty$, the lowest eigenvalue ξ_0 vanishes exponentially fast as $\exp\left(-N/2\, S_I^{(s)}\right)$, see Fig. 2.7 and Fig. 2.5. Interestingly, this is the same exponential factor seen in the splitting $\mathrm{Re}\,(S_1 - S_0)$.

Strong coupling "instanton" saddles

In the strong-coupling phase, it is not the $m = 1$ saddle, but rather the $m = 2$ saddle which we identify as the "strong-coupling instanton" configuration. This saddle is manifestly

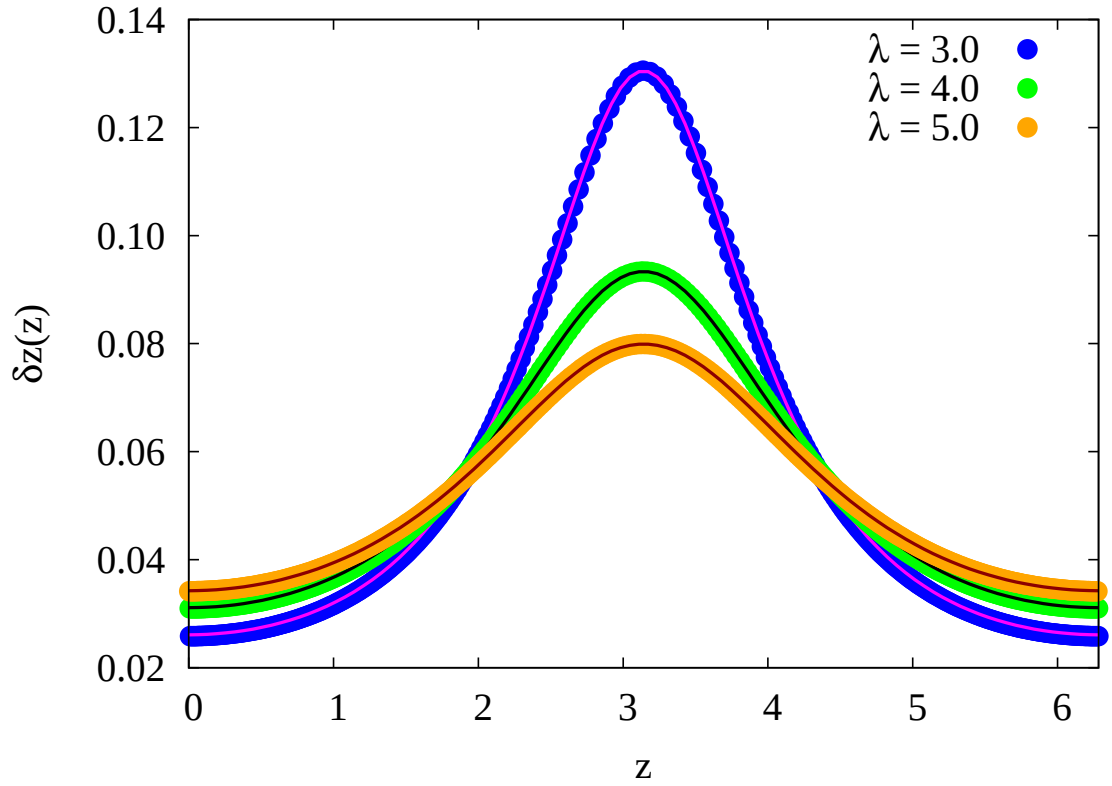

Figure 2.6: Comparison of the analytic expression $\delta z \sim 1/\rho^{(s)}(z)$ for the zero mode of the Hessian matrix H_0 of the $m = 0$ saddle in the strong-coupling phase (solid line) with numerically calculated eigenvector of H_0 which corresponds to the lowest eigenvalue at $N = 400$.

complex, see Fig. 2.1 (g). It has action with real part equal to, as a function of λ, the modulus of the strong-coupling action (2.15): $|\mathrm{Re}\ (S_2 - S_0)\,| = N S_I^{(s)}(\lambda)$, see Fig. 2.4. This reversal of sign is a numerical example of a phenomenon found in the context of the Painlevé equations, where formal trans-series arise with saddles of both signs of the action [10, 11, 71].

As m increases we find that eigenvalues continue to move to complex plane forming a two cut structure on the imaginary axis symmetric with respect to the point $z = \pi$, see Fig. 2.1 (g)-(i). If m is odd then there is always one eigenvalue exactly at the point $z = \pi$. When instanton number m reaches some critical value $m^\star$ the gap between two cuts on the imaginary axis closes and at the same time the gap in the distribution of real eigenvalues on the unit circle opens, see Fig. 2.1 (i),(j).

We find that the real part of the action decreases with m if $m < m^\star$, see Fig. 2.3. Furthermore, we find that the action of saddles $m < m^\star$ with instanton numbers $m = 2n$ and $m = 2n+1$ exhibit quasi-degeneracy similar to that of saddles with $m = 0$ and $m = 1$ (note characteristic "stairs" on the inset of the Fig. 2.3). We also observe corresponding exponentially small quasi-zero mode in the spectrum of Gaussian fluctuations about these saddles.

We find that the saddle point action scales linearly with m for $m \ll m^\star$: $|\mathrm{Re}\ (S_m - S_0)\,| \approx$

$\lfloor m/2 \rfloor \, N \, S_I^{(s)}$, where $S_I^{(s)}$ is the strong-coupling instanton action (2.15). Note the floor function in this expression which takes into account the aforementioned degeneracy of the action.

As in the weak coupling phase, at strong-coupling the Hessian matrix for the m-saddle has m negative modes, see Fig. 2.7. But in the strong-coupling phase, low-lying eigenvalues except the zero-mode become doubly degenerate, with degeneracy splitting governed again by the exponentially small quantity $\exp\Big(-N/2\, S_I^{(s)}(\lambda)\Big)$.

Relation to the trans-series expansion

Our numerical results indicate that the GWW partition function and free energy have trans-series expansions also in the strong-coupling phase due to complex saddle points. This provides a complex saddle interpretation of Mariño's trans-series result from the string equation [8], and is also consistent with the double-scaling limit described by the McLeod-Hastings solution to the Painlevé II equation, valid near the phase transition.

On the weak coupling side this solution has exponential corrections $\sim \exp(-N S_I^{(w)})$, while on the strong-coupling side the leading behavior is already exponential $\exp(-N/2 S_I^{(s)})$. This implies $\exp(-N S_I^{(s)})$ behavior for the free energy [8]. Furthermore, deep in the strong-coupling region, with $\lambda \gg \lambda_c$, and using the method of orthogonal polynomials, Goldschmidt found [70] that corrections behave like:

$$\frac{1}{N^2}\left(\frac{\lambda}{e}\right)^{-2N} \sim \frac{1}{N^2}\exp(-N S_I^{(s)}(\lambda)) \tag{2.19}$$

since the strong coupling instanton action $S_I^{(s)}(\lambda)$ has the following asymptotic expansion for $\lambda \gg \lambda_c$:

$$S_I^{(s)} \sim 2\ln\left(\frac{\lambda}{e}\right) + \frac{2}{\lambda^2} + \dots \tag{2.20}$$

2.3.5 Spectrum of Gaussian fluctuations

Let us consider properties of the spectrum of the Hessian matrix (2.14) and its effect in the saddle point expansion. To this end, we numerically compute eigensystem of the Hessian H at several values of N with the help of the LAPACK linear algebra package.

First of all, we present the flow of few lowest by absolute magnitude eigenvalues as a function of λ on the Fig. 2.7. As we already explained in the previous Subsections, in the weak coupling phase there is always m negative modes for the m-th saddle point. Furthermore, we observe that as system enters strong coupling region $\lambda > \lambda_c$, the lowest by the absolute value mode ξ_0 goes to zero exponentially fast with N, see Fig. 2.5 and Fig. 2.7. Thus, we again find the quasi-zero mode discussed in the previous Subsections.

In the strong coupling phase, low lying eigenvalues become also double-degenerate. Exception is only lowest quasi-zero mode. Interestingly, that at finite N both the quasi-

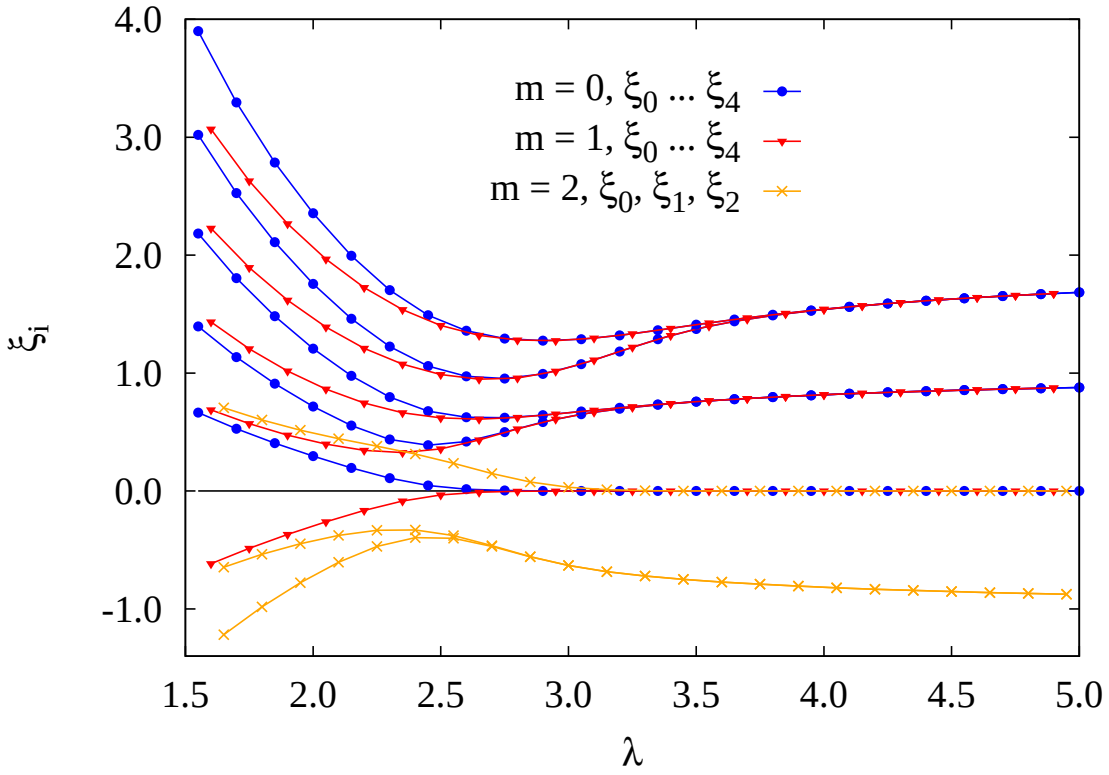

Figure 2.7: Several lowest eigenvalues ξ_i of the Hessian matrix $H_{m,ij} = \frac{\partial^2 S_m}{\partial z_i \, \partial z_j}$ for saddles with $m = 0, 1, 2$ at $N = 40$. There are m negative modes, and at strong coupling all modes, except the quasi-zero-mode, become quasi-degenerate.

zero eigenvalue ξ_0 of the Hessian and the splittings $\xi_1 - \xi_2$, $\xi_3 - \xi_4$, ... between higher eigenvalues are all controlled by the exponential $\exp\left(-N/2\, S_I^{(s)}\right)$ which controls the quasi-zero mode and the splitting of actions $\mathrm{Re}\ (S_1 - S_0)$. This means that eigenvalues become exactly degenerate at $N = \infty$. We depict the splitting at finite N on the left plot on Fig. 2.8.

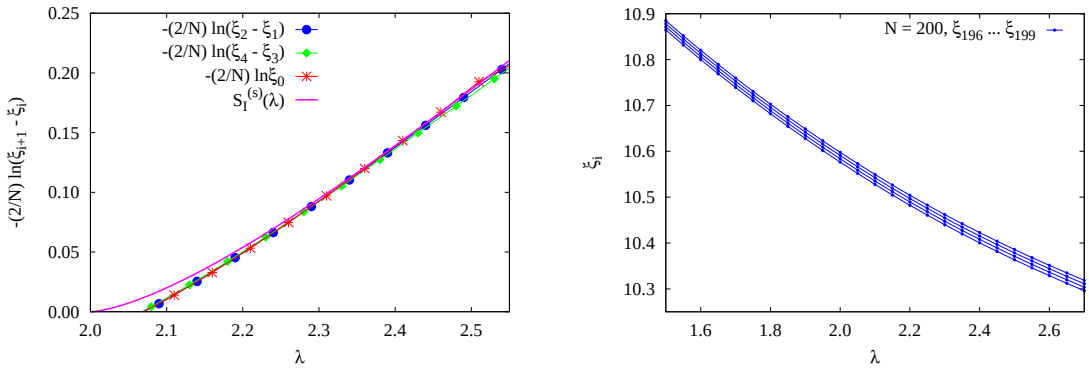

Figure 2.8: Spectral properties of the Hessian matrix H_0 for the saddle point with $m = 0$ in the strong-coupling phase. On the left: logs of the lowest eigenvalue ξ_0 and the spacing between higher eigenvalues for $N = 200$ compared with the strong-coupling instanton action (Eq. (5) in the main text). On the right: 4 highest eigenvalues of H_0.

We also note that apart from the emerging degeneracy, the low-lying eigenvalues of the

Hessian (or the degenerate pairs thereof in the strong-coupling phase) scale approximately as N^1, and the eigenvalues at the upper edge of the spectrum (see the right plot on Fig. 2.8) - approximately as N^2. From the right plot on Fig. 2.8 we see also that the double degeneracy of eigenvalues is absent at the upper edge of the spectrum. This behaviour presumably ensures finite value of the determinant of the Hessian (despite the presence of the quasi-zero mode) as follows from compactness of the $U(N)$ group.

In the saddle-point approximation, the Hessian matrix determines the next-to-leading order correction:

$$\det(H)^{-1/2} = e^{-1/2\mathrm{tr}\,\ln H} \tag{2.21}$$

to the path integral originating from the Gaussian fluctuations around saddle points. It turns out that despite all the interesting properties of the eigenspectrum of the Hessian matrix, the full determinant obtained by multiplying all N eigenvalues appears to be a rather smooth, almost constant function. In particular, it seems that the exponentially small contribution of the lowest eigenvalue is compensated in some way by the product of higher eigenvalues.

In order to illustrate the effect of Hessian determinant, on Fig. 2.9 on the left we plot the Gaussian correction $-1/2\mathrm{tr}\,\ln H$ to the saddle-point free energy and compare it with the leading contribution from the saddle action S_0 at $N = 30$ and $N = 40$. We also plot the analytic result for the planar free energy $E_0(\lambda)$ (2.10) in order to visualize $1/N$ corrections to S_0. One can see that as compared to the leading contribution, the Gaussian correction due to the Hessian is a very slowly changing function of λ. Interestingly, this correction is always negative, thus increasing the saddle point contribution.

Furthermore, on the right plot on Fig. 2.9 we plot the difference of the actions of the $m = 0$ and $m = 1$ (at weak coupling) or $m = 2$ (at strong coupling) saddles, both with and without the Gaussian corrections $1/2\mathrm{tr}\,\ln H$ included:

$$\Delta S = \begin{cases} S_1 - S_0, & \lambda < 2 \\ S_0 - S_2, & \lambda \geq 2 \end{cases}, \quad \Delta H = \begin{cases} H_1 - H_0, & \lambda < 2 \\ H_0 - H_2, & \lambda \geq 2 \end{cases}, \tag{2.22}$$

where H_m denote the Hessian matrices for the saddles with instanton number m. For comparison, we also plot the exact large-N instanton actions (2.13) and (2.15). Again one can see that the Gaussian corrections do not result in any significant modifications of the saddle contributions. We also note that for finite values $N = 30$ and $N = 40$ used for these plots the transition from the weak-coupling to the strong-coupling regime is shifted towards larger λ (of course, at finite N this is no longer a phase transition). Unfortunately, we cannot calculate the Gaussian corrections at significantly larger N and thus enable direct comparison with (2.13) and (2.15), since the calculation of $\det(H)$ becomes numerically unstable at large N and the comparison is anyway impossible due to numerical errors. Nevertheless, for $N = 30,\ 40$ it seems that the effect of the inclusion

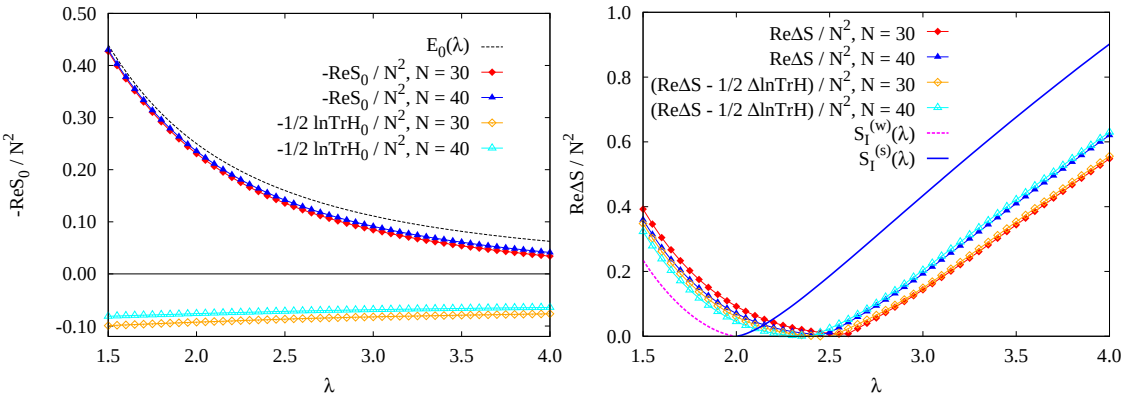

Figure 2.9: The effect of the Gaussian corrections $-1/2\mathrm{tr}\ \ln H$ to the saddle action on the action of the vacuum saddle with $m = 0$ (on the left) and on the difference of the actions of $m = 0$ and $m = 1$ (in the weak-coupling phase) or $m = 2$ (in the strong-coupling phase) saddles. We see that the effect of the Gaussian correction is very small and is hardly distinguishable from finite-N corrections to the actions.

of the Hessian is very minor, and can be hardly distinguished from systematic errors due to finiteness of N. We thus conclude that the fluctuations around nontrivial saddles in the GWW model (2.5) should not change the exponential factors $e^{-m\,N\,S_I}$ in the trans-series.

2.4 Conclusions

Our numerical study reveals a surprisingly rich structure of complex-valued saddles in both the weak- and strong-coupling phases of two-dimensional lattice gauge theory, represented by the Gross-Witten-Wadia unitary matrix model. These complex saddles are intimately related to the resurgent structure of the 1/N expansion. We find a new complex saddle interpretation of Mariño's strong-coupling instanton action, and these saddles have novel physical properties. There is clear numerical evidence for instanton condensation at the transition. In both phases, eigenvalue tunneling produces complex saddles, and these results suggest a Lefschetz thimble interpretation of the saddle point expansion. Given the direct relation between the instanton actions in the matrix model (2.5) and in 2D continuum gauge theory [8], we expect similar results for complex-valued saddles to apply also to continuum 2D gauge theories [66, 67].

Chapter 3

Lattice study of adiabatic continuity conjecture in two-dimensional Principal Chiral Model

3.1 Introduction

The innovative idea of resurgent trans-series has recently allowed to better understand the structure of perturbative expansions for asymptotically free quantum field theories, such as four-dimensional gauge theories and two-dimensional sigma models. In particular, for two-dimensional sigma models resurgent trans-series provide a precise interpretation of the factorial non-Borel-summable infrared renormalon divergences of perturbative series [14–16, 30, 31] in terms of saddle points of the classical action, even if they are non-topological, unstable and/or complex-valued.

However, at present this interpretation of infrared renormalon divergences can be explicitly worked out only for quantum field theories with compactified spatial direction $\mathbb{R}^{d-1} \times S^1$, in which the fields satisfy certain twisted boundary conditions. The compactification length L_0 should be sufficiently small with $NL_0\Lambda \ll 2\pi$, where Λ is the dynamically generated energy scale and N is the rank of the symmetry group. In this limit the theory is in the weakly coupled regime while still exhibiting non-perturbative features such as dynamically generated mass gap. This defines the so-called Ünsal-Dunne regime, which allows for explicit construction of trans-series.

The so-called continuity conjecture states that the Ünsal-Dunne regime at small L_0 is analytically connected to the strongly coupled regime at large L_0 [15, 31], in which boundary conditions become irrelevant and the physics is equivalent to the low-temperature phase with periodic boundary conditions. This conjecture is based on the observation that the physical properties of gauge theories and sigma models appear to be qualitatively very similar in both Ünsal-Dunne regime and in the genuine strong-coupling

regime at small temperatures or large compactification length.

The continuity conjecture is closely related to the Eguchi–Kawai (EK) reduction in lattice field theory [72–74] where the full theory is suggested to be equivalent to twisted single site model in the large N limit. It is known that the original EK reduction without twist [72] does not work due to spontaneous breaking of the center symmetry $\mathbb{Z}_N^d$ [75]. Considering EK reduced model as a result of continuous dimensional reduction from large to very small lattices it is evident that this symmetry breaking is manifestation of deconfinement phase transition happening when the torus is sufficiently small $L_0\Lambda \sim 1$ [76, 77]. A possible solution is to introduce the twisted boundary conditions which preserve center symmetry and prevent it from spontaneous breaking, thus suppressing the deconfinement transition and allowing for analytic (or volume independent) connection between the regimes of small and large L_0. However, lattice simulations of twisted EK reduced model indicate that spontaneous symmetry breaking can still occur and pose the question of the existence of the continuum limit [78], although it seems that these difficulties can be overcome [74]. Possible ways of stabilizing center symmetry in gauge theories are the special deformations of the gauge action [79] or the introduction of adjoint fermions [80], which effectively induce center-preserving holonomies along the compactified directions. These ideas were important to formulate the continuity conjecture in PCM.

In two-dimensional sigma models the prescription for $\mathbb{Z}_N$-preserving twist $\Omega \in SU(N)$ reads as:

$$\operatorname{Tr}\Omega^n = \begin{cases} N, & n \equiv 0 \bmod N \\ 0, & \text{otherwise} \end{cases} . \tag{3.1}$$

This operator either projects excited states out or provides a phase shift which leads to mutual cancellations between distinct states in the partition function. Since a lot of excited states do not contribute at all to the twisted partition function [81], one can hope that the deconfinement transition is eliminated [15, 31]. However, to turn continuity conjecture into a precise statement, one should demonstrate that no phase transition or crossover occur as the compactification length L_0 changes from large values $NL_0\Lambda \gg 2\pi$ to small values with $NL_0\Lambda \ll 2\pi$. At present a rigorous analytic demonstration of this fact is still lacking due to the absence of reliable analytic methods for strongly coupled quantum field theories. Notable exceptions are the exactly solvable large-N $\mathbb{CP}^{N-1}$ and $O(N)$ non-linear sigma-models for which an explicit demonstration has been worked out [81]. However, for Principal Chiral Model (PCM) which is especially interesting due to its matrix-like planar limit very similar to that of QCD the problem clearly calls for first-principle simulations.

Unfortunately, not much is known about thermodynamic properties of PCM in general, although this model is integrable and many exact results can be obtained using bootstrap

techniques [82–86]. One of the reasons is that for PCM there is no obvious local parameter which can be used to characterize the "deconfinement" phase transition, rendering analytic and lattice studies very difficult. Recently a thermodynamic Bethe ansatz has been proposed in order to investigate thermodynamic properties [87], however without definite conclusions so far.

In this work we test continuity conjecture for the two-dimensional $SU(N) \times SU(N)$ PCM using first-principle Monte-Carlo simulations. We study several characteristic quantities such as static correlation length, mean energy and specific heat and demonstrate that they exhibit qualitatively different dependence on the length of the compact direction L_0 with periodic (Section 3.3) and twisted (Section 3.4) boundary conditions. In both cases we find some evidence for a transition/crossover which however posses very different features: while for periodic boundary conditions this might be a finite-temperature transition (probably similar to deconfinement in QCD), for twisted boundary conditions this is at most a crossover with respect to the combined length parameter $\rho \equiv NL_0$.

Furthermore, in Section 3.5 we use Gradient Flow [88] to evolve the field configurations sampled by Monte-Carlo process towards the saddle points of the classical action, and demonstrate that the resulting "almost classical" field configurations feature localized non-perturbative objects which resemble the uniton and fracton saddle points known for continuum PCM [15, 31]. Twisted boundary conditions stabilize those saddle points and, as expected, lead to the emergence of effective topological sectors [15, 31]. We also find that geometric properties of non-perturbative objects strongly change in the region of the possible phase transition or crossover for both boundary conditions.

3.2 Simulation setup and observables

The lattice action of the two-dimensional $SU(N) \times SU(N)$ PCM can be written as:

$$S\left[U\left(\mathbf{x}\right)\right] = -2\beta N \sum_{\mathbf{x},i} \mathrm{Re}\,\mathrm{Tr}\,\left[U\left(\mathbf{x}\right) U^{\dagger}\left(\mathbf{x}+\mathbf{e}_i\right)\right], \tag{3.2}$$

where $\beta \equiv \lambda^{-1} = 1/(g^2 N)$ is an inverse of the t'Hooft coupling λ and $\mathbf{e}_i$ is a unit lattice vector in direction i. We have used lattices of the size $L_0 \times L_1$ with boundary conditions (BC) defined as:

$$\begin{aligned} U\left(x_0+L_0, x_1\right) &= \Omega_0 U\left(x_0, x_1\right) \Omega_0^{\dagger}, \\ U\left(x_0, x_1+L_1\right) &= U\left(x_0, x_1\right), \end{aligned} \tag{3.3}$$

where matrix Ω_0 determines the type of boundary conditions:

$$\Omega_0 = \begin{cases} I, & \text{for periodic BC (PBC)} \\ \Omega, & \text{for twisted BC (TBC)} \end{cases}. \tag{3.4}$$

The twist matrix Ω has the following form:

$$\Omega = e^{i\frac{\pi}{N}\nu}\mathrm{diag}\{1, e^{i\frac{2\pi}{N}}, \cdots, e^{i\frac{2\pi(N-1)}{N}}\}, \tag{3.5}$$

where $\nu = 0, 1$ for N odd, even. It is easy to see that Ω satisfies the equation (3.1).

We employed the standard Cabbibo-Marinari algorithm [89] in order to stochastically sample field configurations $U(\mathbf{x})$ according to Boltzmann weight $\exp\left(-S\left[U\left(\mathbf{x}\right)\right]\right)$ with the action (3.2). One Monte-Carlo update of the field configuration was implemented by applying the heat bath algorithm to all $SU(2)$ subgroups of all $U(\mathbf{x})$ matrices. Each Monte-Carlo step was followed by overrelaxation step [90] in order to decrease auto-correlation time. Error analysis was carried out using jacknife and bootstrap techniques. In order to test our code, we have reproduced several data points from the previous PCM simulations of [91] with very high precision.

We performed calculations for $\beta = 0.332$, $N = 6, 9, 12, 18$ and spatial lattice sizes $L_1 = 108$ and, for $N = 18$, $L_1 = 200$, which we found to be sufficiently large compared to zero-temperature static correlation length taking values in the range $\xi_0 = 10 \ldots 12$ (for different N) in our simulations. For each value of N and type of boundary conditions we have simulated at multiple values of the compactification length L_0 in the intervals $1 \leq L_0 \leq L_1$ for periodic and twisted boundary conditions, respectively.

In order to study basic thermodynamic properties, we have computed the mean energy

$$E = 1 - \frac{1}{4N^2}\frac{\partial F}{\partial \beta} =$$
$$= 1 - \frac{1}{N}\left\langle \mathrm{Re}\,\mathrm{Tr}\,\left[U\left(\mathbf{x}\right)U^{\dagger}\left(\mathbf{x}+\mathbf{e}_i\right)\right]\right\rangle \tag{3.6}$$

and specific heat

$$C = \frac{1}{N}\frac{dE}{dg^2}. \tag{3.7}$$

In order to compute the static correlation length we rely on the observation that in the weak-coupling regime for sufficiently small values of lattice momenta as compared to the dynamically generated mass gap the Fourier transform of the group invariant correlation function $G(\mathbf{x})$ can be with a good precision approximated by the free scalar propagator [91]:

$$\tilde{G}(\mathbf{k}) \simeq \frac{Z_G}{M^2 + 4\sin^2\left(k_0/2\right) + 4\sin^2\left(k_1/2\right)}, \tag{3.8}$$

where Z_G is the wave-function renormalization constant. From this equation one obtains an expression for static correlation length ξ in terms of the momentum-space correlator at the two lowest values of lattice momenta:

$$\xi^2 = \frac{1}{4\sin^2\left(\pi/L\right)}\left[\frac{\tilde{G}(0,0)}{\tilde{G}(0,1)} - 1\right]. \tag{3.9}$$

Alternatively, correlation length can be computed with the standard exponential fits of wall-wall correlators and we have checked that numerical values for ξ obtained in both ways agree with a high precision.

Similarly to the two-dimensional lattice gauge theory [62], lattice PCM undergoes the large N phase transition from strong to weak coupling phase at $\beta_c = 0.305$ [91–93], which in this case is a second-order transition at which the specific heat diverges and the distribution of eigenvalues $\lambda = e^{i\phi}$ of the link matrices $U(\mathbf{x})\, U^{\dagger}(\mathbf{x} + \mathbf{e}_i)$ develops a gap. Continuum scaling of different observables such as mass gap already sets up in the vicinity of the critical coupling $\beta \gtrsim \beta_c$ [91, 92]. For our simulations we have chosen the value $\beta = 0.332$ sufficiently deep in the weak coupling phase. To check that with this value of coupling we are sufficiently to the continuum limit, we have observed the asymptotic scaling of zero-temperature static correlation length ξ_0 (measured on lattices with $L_0 = L_1$ for $N \geq 9$) in the so-called β_E scheme [92]:

$$\xi(E) = \frac{0.991}{16\pi} e^{\frac{2-\pi}{4}} \sqrt{E} e^{\pi/E}. \tag{3.10}$$

While the constraints in CPU time available for our simulations have forced us to work at a single value of β, in future work it would be also desirable to check the continuum scaling of correlation length and thermodynamic observables by performing simulations at several values of β.

In order to exclude possible large N phase transition to physically irrelevant strong coupling phase as the compactification length varies in the range $L_0 = 1 \ldots L_1$, we have studied angle distribution of eigenvalues of link matrices $U(\mathbf{x})\, U^{\dagger}(\mathbf{x} + \mathbf{e}_i)$ and found that it remains gapped and almost unchanged for all directions i and boundary conditions at all values of L_0. This suggests that finite temperature transition which we discuss below has different nature and seems to be a feature of continuum theory.

In order to better visualize important properties of our physical observables we have normalized them with respect to the corresponding zero temperature values at periodic boundary conditions and the same N:

$$O_0 \equiv O(L_0 = L_1, \mathrm{PBC}), \tag{3.11}$$

where O is some physical observable, and depict the relative change rather than the value itself:

$$\frac{\Delta O(L_0)}{O_0} \equiv \frac{O(L_0) - O_0}{O_0}. \tag{3.12}$$

This normalization is motivated by the fact that all observables admit non-trivial $1/N$ corrections which render straightforward comparison at different N not very illustrative. Note also that identical normalization allows to conveniently compare the physics for both types of boundary conditions. We have also performed fits to the lowest-order $1/N$

expansion:

$$O(L_0, N) = \tilde{O}(L_0) + c_1/N^2 \tag{3.13}$$

in order to estimate infinite N values $\tilde{O}(L_0)$, which are also presented on our figures. Very high precision of the numerical data for the mean energy also allowed us to include the terms of order $1/N^4$ into the fitting function (3.13) for this observable. In order to calculate the relative changes (3.12) in the limit $N \to \infty$, we perform separate large-N extrapolations of the form (3.13) both for $O_0 \equiv O(L_0 = L_1, \mathrm{PBC})$ in the denominator and for the finite-temperature value $O(L_0)$ in the numerator, which typically results in a smoother extrapolation. Furthermore, when plotting the data points as functions of the compactification length L_0, we express L_0 in units of zero-temperature static correlation length ξ_0 calculated with the same N as the data. This rescaling should allow to compare our current data with prospective simulations at other values of coupling as well as with calculations for continuum PCM.

3.3 Periodic boundary conditions and the finite-temperature "deconfinement" transition

To study possible transition between low-temperature and high-temperature regimes, which correspond to large and small compactification length L_0 with periodic boundary conditions, on Fig. 3.1(a) we first illustrate the dependence of the static correlation length ξ on L_0. At all values of N the correlation length stays almost constant for large values of L_0, then exhibits statistically significant growth in the range $L_0/\xi_0 = 3 \ldots 5$, and finally decreases for smaller L_0, seemingly reaching some finite value at $L_0 \to 0$. The position of the maximum of correlation length slowly shifts to smaller values when N is increased. For the data points extrapolated to infinite N the peak lies approximately at $L_0^c/\xi_0 \approx 3.5$. An important point to stress that in contrast to e.g. CP^N sigma model, for the principal chiral model the transition temperature remains finite in the large-N limit, as also indicated by the recent Diagrammatic Monte-Carlo simulations directly in the large-N limit [94]. This property is also expected for large-N gauge theories [95].

At the same time, the maximal value of the peak shows tendency to grow with N and its width seems to decrease. Extrapolations to the large-N limit using the fits of the form (3.13) at fixed values of L_0 suggest that the maximal value of ξ remains finite in the large N limit. Furthermore, even upon the large-N extrapolation the enhancement of the correlation length appears to be very weakly pronounced: the relative change in ξ is of order of 5%. Simulations at larger volumes ($L_1 = 200$) also reveal a rather small ($\sim 2\%$) enhancement of ξ with volume, see the left plot on Fig. 3.2.

The emergence of such a peak structure and clearly distinct behaviour of correlation length at small and large L_0 are suggestive of a finite-temperature phase transition or

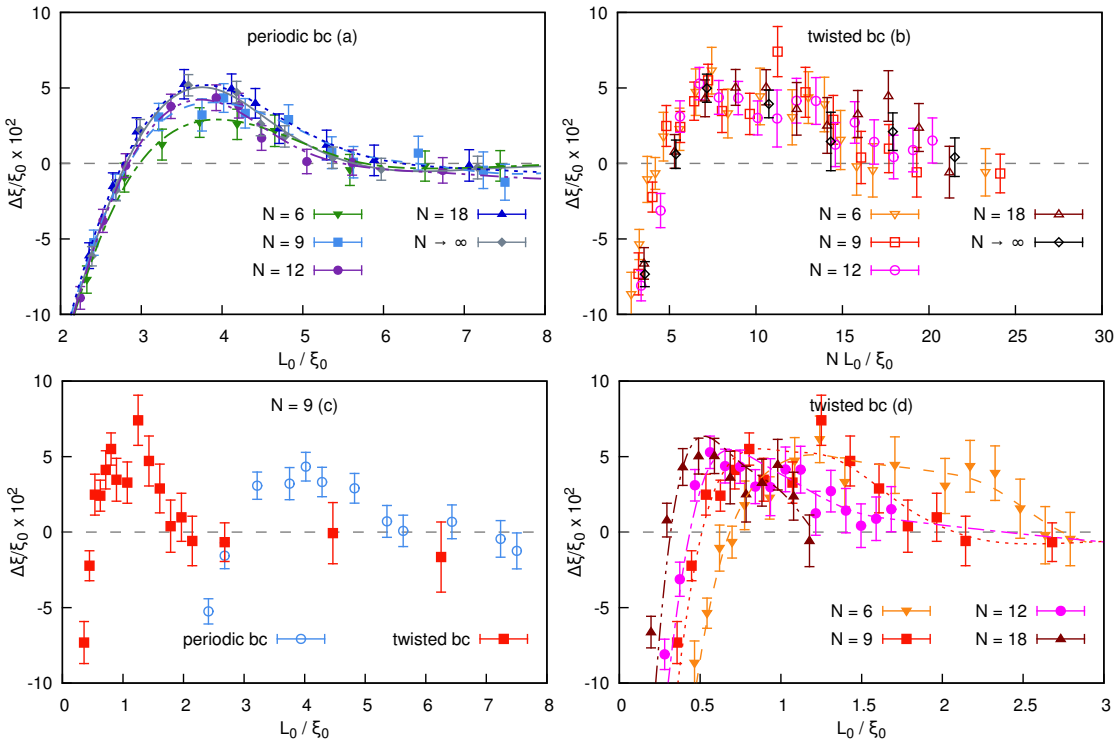

Figure 3.1: Relative change of correlation length $\Delta\xi/\xi_0$ as a function of compactification length L_0 for different boundary conditions and values of N. In the plots at the top, we illustrate the dependence of the correlation length on the natural compactification scales: L_0 for PBC and NL_0 for TBC. The plots at the bottom illustrate how the peak in the correlation length with TBC shifts to smaller L_0 as N is increased. For periodic boundary conditions, extrapolations to infinite N are obtained using the fits of the form (3.13).

crossover. This transition also manifests itself in the distinct behaviour of thermodynamic observables at low and high temperatures. In particular, both the mean energy $E(L_0)$ and the specific heat C take almost constant values when $L_0 > L_0^c$ and then decrease in the region $L_0 < L_0^c$, see Fig. 3.3 for illustration.

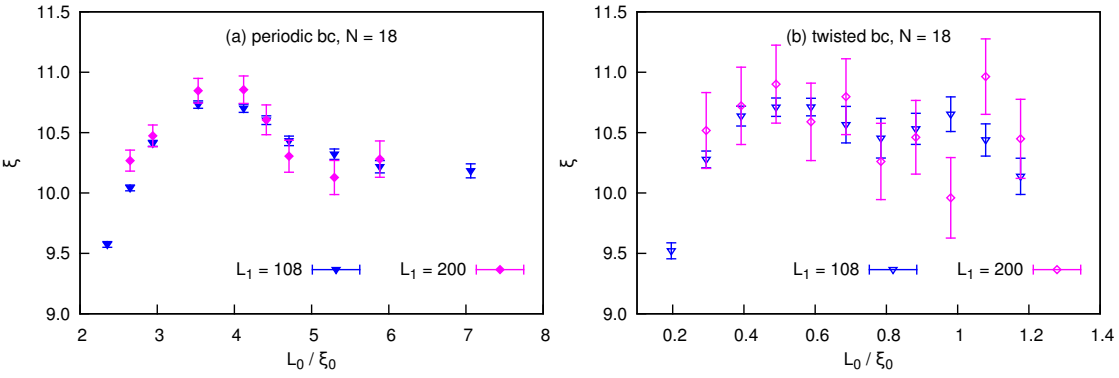

Figure 3.2: Volume dependence of the correlation length ξ in the vicinity of the peak for periodic and twisted boundary conditions for $N = 18$.

However, not much is known on the nature of this transition. The observed scaling with N and L_1 suggest that the finite-temperature transition is rather weak, but cannot

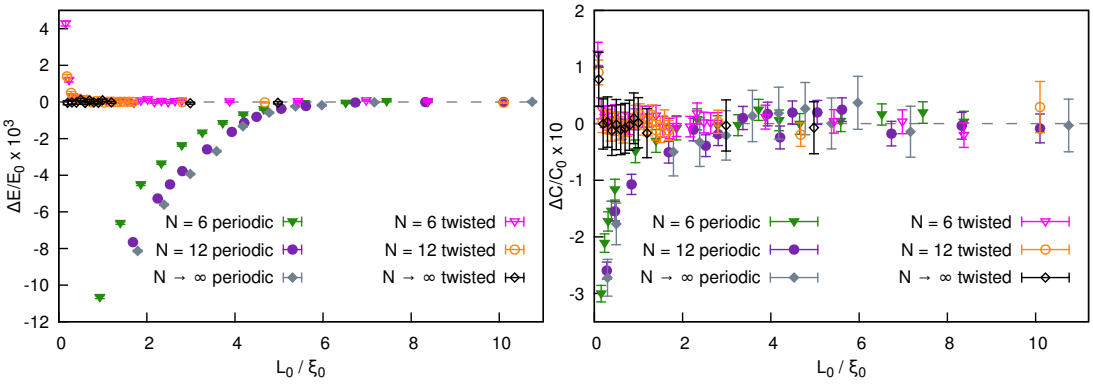

Figure 3.3: Relative changes of the mean energy $\Delta E/E_0$ (left plot) and the specific heat $\Delta C/C_0$ (right plot) as functions of compactification length L_0 for different values of N and boundary conditions. The $N \to \infty$ data for the mean energy are obtained using extrapolations of the form $E(N) = \tilde{E} + c_1/N^2 + c_2/N^4$ at fixed L_0.

completely distinguish between the weak phase transition and crossover. A more detailed combined study of the finite-volume and finite-N scaling is required to make a definite conclusion about the order of this finite-temperature transition, which we leave for future work. A recent Diagrammatic Monte-Carlo study [94] at $N \to \infty$ limit also indicated the relatively weak enhancement of correlation length at the same critical value of L_0, but did not completely exclude the possibility of divergent correlation length at the transition point.

On the general grounds in analogy with other asymptotically free theories one might expect a "deconfinement" phase transition associated with effective liberation of $SU(N)$ degrees of freedom at sufficiently high temperature. For gauge theories, the deconfinement transition is typically associated with the breaking of the global Z_N^d center symmetry, with Polyakov loop being the local order parameter. In contrast, for principal chiral model even an approximate local order parameter which would allow to distinguish the "confinement" and the "deconfinement" phases is not known. In principle, any kind of phase transition should result in a non-analytic behavior of the free energy $\mathcal{F} \sim -\ln \mathcal{Z}$, which for the deconfinement transition in PCM is expected to behave as [31]

$$\lim_{N\to\infty} \mathcal{F}/N^2 \sim \begin{cases} 1, & L_0\Lambda \ll 1, \\ 0 & L_0\Lambda \gg 1. \end{cases} \tag{3.14}$$

While a direct calculation of the free energy is nontrivial in Monte-Carlo simulations, first-order transitions typically result in a characteristic double-peak structure of the action probability distribution with unequal peak heights [96]. Our numerical data for the mean energy does not exhibit any double-peak structure, which disfavours the first-order phase transition scenario (although not excluding it completely, as one might need very high statistics to distinguish the two peaks).

In the context of large-N volume independence our results suggest that correlation

length, mean energy and specific heat do not depend on the lattice size as long as it is much larger than the typical correlation length, in close analogy with large-N gauge theories [76, 77]. The deviations from volume independence only become significant in the vicinity of the transition point or crossover.

3.4 Twisted boundary conditions and the transition to Ünsal-Dunne regime

We start the discussion of the principal chiral model with twisted boundary conditions (3.3) by presenting our results for the static correlation length (3.9) on Fig. 3.1(b). If we plot ξ as a function of L_0, we again clearly see two distinct regions separated by a peak of ξ: when L_0 is large the correlation length $\xi(L_0)$ coincides with zero-temperature value ξ_0 (3.11). At intermediate values of L_0 ξ exhibits a statistically significant growth, and in the region of small L_0 it decreases again, finally reaching some finite value. Note that the maximal relative change of ξ is of the same order as in the case of periodic BC: approximately 5%. However, apart from the existence of the peak, the dependence of correlation length on L_0 and N seems to be very different from the case of periodic BC. In particular, the peak height does not depend on N within statistical errors, and its position shifts to smaller L_0 as N is increased. The fits of the form (3.13) have rather poor quality for data points with fixed L_0.

Let us now recall that due to the properties (3.1) of the twist matrix the group-invariant correlation function are periodic on the cylinder $\mathbb{R} \times S^1$ with effective size of S^1

$$\rho \equiv N L_0. \tag{3.15}$$

In other words, the twist effectively increases the volume accessible to the system by a factor of N and lowers the "temperature", which is a pre-requisite for the twisted Eguchi-Kawai reduction [79]. This property suggests that one should compare the data for twisted and periodic boundary conditions by identifying the compactification lengths as $N L_0^{TBC} = L_0^{PBC}$.

Plotting the static correlation length as a function of ρ on the right plot on the top of Fig. 3.1, we observe a rather clear collapse of data points with different N towards a single curve, which features a peak at $\rho_c/\xi_0 \approx 9$. At $\rho > \rho_c$ we find good agreement with data for periodic BC at zero temperature. Infinite-N extrapolations using the fits (3.13) yield only very minor corrections to this picture. Increasing the spatial lattice size to $L_1 = 200$ at $N = 18$, we do not observe a significant enhancement of the correlation length beyond statistical errors, see the right plot on Fig. 3.2. We note here that the statistical errors in the correlation length appear to be larger for the twisted case, although we have almost two times more data points in this case. Unfortunately, large statistical

errors do not allow us to make a definite conclusion on whether the enhancement of correlation length at $L_1 = 200$ is larger for periodic or for twisted boundary conditions. We can only say that for twisted case the change in the correlation length cannot be much larger than for periodic case.

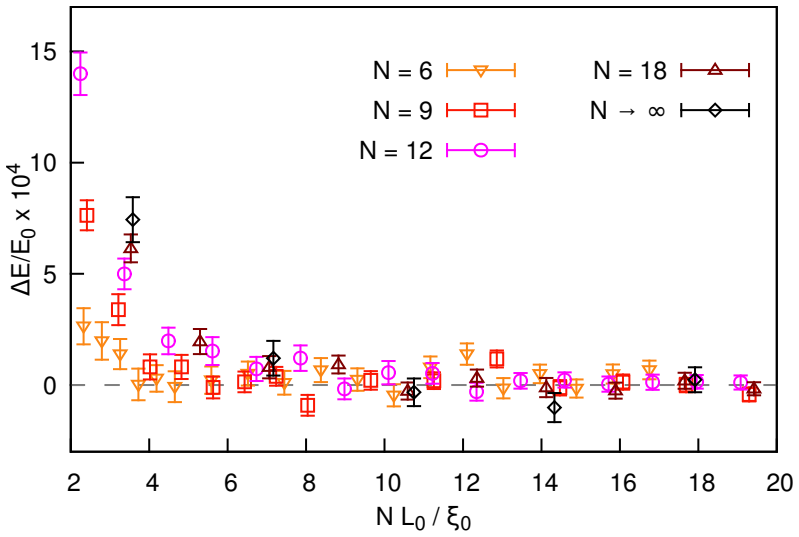

Figure 3.4: Relative change of mean energy $\Delta E/E_0$ for twisted boundary conditions and different values of N represented as a function of $\rho \equiv NL_0$.

As one can see from Fig. 3.3, with twisted boundary conditions the mean energy and the specific heat practically do not depend on the compactification length down to the values of L_0 which roughly correspond to the position of the peak on Fig. 3.1(b). In contrast to the case of periodic boundary conditions, at small L_0 the mean energy $E(L_0)$ increases. The data for specific heat $C(L_0)$ has quite large statistical errors which probably do not allow to see non-trivial behavior on lattices $L_0 > 1$. Nevertheless, with smallest compactification length $L_0 = 1$ we again observe an increase of C compared to zero temperature.

If we fix L_0 and fit the N dependence of $\Delta E/E_0$ using (3.13), it extrapolates to zero in the large-N limit for all values of L_0 which we consider ($L_0 \geq 2$). This observation supports the volume independence property at $\rho > \rho_c$. On Fig. 3.4 we also plot the mean energy as a function of ρ. In agreement with volume independence property, for $\rho > \rho_c$ the values of $\Delta E/E_0$ are consistent with zero within statistical errors. However, in contrast to correlation length, for smaller values of ρ different data points for the mean energy do not collapse. This suggests that for small values of ρ long-distance quantities such as correlation length and local quantities such as mean energy might exhibit different scaling with N.

To summarize, with twisted boundary conditions we also observe some signatures of a nontrivial transition between the regimes of small and large compactification lengths which is controlled by a combined parameter $\rho \equiv NL_0$. Considered as a function of the compactification length L_0, this transition shifts to smaller and smaller L_0 as N is

increased (see the left plot in the bottom of Fig. 3.1), eventually approaching the zero radius limit at $N \to \infty$ and thus effectively disappearing. A similar behavior was found for the scale of dynamical symmetry breaking in gauge theories with unbroken center symmetry [97]. At $\rho > \rho_c$ physical observables practically do not depend on the lattice size, as could be expected for twisted Eguchi-Kawai reduction. The most important differences with the finite-temperature transition considered in the previous Section 3.3 are, first, the independence of the height of the peak in the correlation length on N, and, second, the growth of the mean energy at small ρ, along with its nontrivial scaling with N. We will discuss these differences in more details in the concluding Section 3.6.

3.5 Non-perturbative saddle points

Non-perturbative saddle points of the action in the path integral are one of the cornerstones of the physical applications of resurgence theory. In particular, factorial divergences in perturbative series which characterize small field fluctuations around non-perturbative saddles cancel similar divergences in perturbative expansion around the trivial vacuum saddle, thus allowing to complete the so-called resurgent triangle. To ensure that resurgent trans-series of the twisted compactified PCM in the Ünsal-Dunne regime can be analytically continued to the low-temperature strongly coupled regime, it is also important to understand how the saddle points which dominate the path integral and enter the resurgent triangle change in the process of compactification from $L_0 \to \infty$ to $L_0 \ll 2\pi \left(\Lambda N\right)^{-1}$.

To study the features of the dominant saddle points in the path integral, we select randomly the field configurations generated in Monte-Carlo simulations, and evolve them along the path of the steepest descent towards one of the saddle points in its vicinity using the Gradient Flow equations [88]:

$$\frac{\partial U\left(\mathbf{x},\tau\right)}{\partial \tau} = -\frac{i}{\beta N}\,\nabla^a_{\mathbf{x}} S\left[U\left(\mathbf{x},\tau\right)\right]\, T_a\, U\left(\mathbf{x},\tau\right), \qquad U\left(\mathbf{x},\tau=0\right) \equiv U(\mathbf{x}), \tag{3.16}$$

where τ is the flow time and $\nabla^a_{\mathbf{x}}$ is the $SU\left(N\right)$ Lie derivative with respect to $U\left(\mathbf{x}\right)$:

$$\nabla^a_{\mathbf{x}} f\left[U\left(\mathbf{y},\tau\right)\right] = \frac{d}{ds} f\left[e^{isT_a\delta_{\mathbf{x},\mathbf{y}}} U\left(\mathbf{y},\tau\right)\right]\Big|_{s\to 0}. \tag{3.17}$$

Here the $SU\left(N\right)$ group generators T^a are Hermitian and traceless matrices normalized as $\mathrm{tr}\,\left(T_a T_b\right) = \delta_{ab}$. The advantage of using the Gradient Flow instead of other smoothing procedures such as smearing or cooling is that the Gradient Flow is continuous and reversible with respect to the flow time τ, therefore it can be considered as a well defined change of the variables in the partition function which preserves all physical information encoded in the initial field configuration and at the same time ensures that in terms

of the flow-evolved variables $U(\mathbf{x},\tau)$ the partition function is dominated by smooth configurations [88].

We have numerically solved equations (3.16) using Runge–Kutta discretization scheme described in [88] with the time step $d\tau = 0.1$ and initial conditions $U(\mathbf{x},\tau=0)$ selected randomly from field configuration generated by Monte-Carlo process. We have continued the Gradient Flow up to the final flow time $\tau_f = 1.5\times 10^3$.

In order to characterize the features of smoothed configurations we have considered the total action S given by (3.2), as well as the local action density

$$S(\mathbf{x},\tau) = \\ = \beta N \sum_i \left(N - \mathrm{Re}\,\mathrm{Tr}\,\left[U(\mathbf{x},\tau)\,U^\dagger(\mathbf{x}\pm\mathbf{e}_i,\tau)\right]\right) \tag{3.18}$$

normalized such that it is zero for vacuum configuration with $U(\mathbf{x}) = I$.

Since on a finite lattice the continuum saddle points such as unitons and fractons [15] are only approximate solutions to the saddle point equations, during the Gradient Flow evolution they appear as meta-stable states which are eventually destroyed. Nevertheless, within characteristic plateaus and not very large flow times the smoothed fields are expected to properly reflect the basic properties of the continuum saddle points (such as e.g. Z_N-valued holonomies or phases, or topology in gauge theories). For instance, point-like objects should appear in the profile of the actions density as pronounced lumps of action density on the smooth background. For very large flow times and in a finite volume this correspondence between smoothed fields and continuum saddle points is lost since Gradient Flow can be considered as a diffusion process which strongly entangles all degrees of freedom and spreads them uniformly on the lattice.

The fracton and uniton saddles which appear in the path integral of continuum two-dimensional PCM do not have an intrinsic topological structure due to the fact that $\pi_2[SU(N)] = 0$, in contrast to QCD and non-linear $\mathbb{CP}^{N-1}$ model. The absence of topological charge makes lattice studies of these non-perturbative objects more difficult and leaves the local action density (3.18) as the only scalar field which can characterize them in a simple and universal way.

In order to characterize the localization of action density for saddle point solutions, we have used the inverse participation ratio (IPR):

$$\mathrm{IPR}(\tau) = V\left\langle \frac{\sum_{\mathbf{x}} \tilde{S}^2(\mathbf{x},\tau)}{\left(\sum_{\mathbf{x}} \tilde{S}(\mathbf{x},\tau)\right)^2}\right\rangle, \tag{3.19}$$

$$\tilde{S}(\mathbf{x},\tau) = S(\mathbf{x},\tau) - \min_{\mathbf{x}} S(\mathbf{x},\tau), \tag{3.20}$$

where $\tilde{S}(\mathbf{x},\tau)$ is the action with subtracted constant background, $V = L_0 L_1$ is the lattice volume and averaging over smoothed field configurations at the same flow time is implied.

By construction, this quantity takes the maximal value $\mathrm{IPR} = V$ when the action density is localized on a single lattice site and reaches the minimal value $\mathrm{IPR} = 1$ when it is everywhere constant. A very useful property of IPR is that it scales as $1/n$ if there are n similar localized objects in the action density. In general, it gives the inverse fraction of the volume occupied by the support of $S(\mathbf{x}, \tau)$, thus it can serve as a measure of action density localization.

To present our results for periodic boundary conditions, on Fig. 3.5 we first plot a typical dependence of the total action $S\left[U\left(\mathbf{x}, \tau\right)\right]$ of smoothed field configurations $U\left(\mathbf{x}, \tau\right)$ on the Gradient Flow time τ, where several different lines represent independent Gradient Flows with different initial conditions $U\left(\mathbf{x}, \tau = 0\right) \equiv U\left(\mathbf{x}\right)$. We observe that the total action starts from large values at initial moment of time and then rapidly decreases down to zero approximately at $\tau \approx 1.5 \times 10^3$. For some initial conditions, the decay of the action with the flow time becomes somewhat slower in the range $\tau = (0.4 \ldots 0.8) \times 10^3$, so that sometimes a kind of "plateau" is formed.

Typical profiles of the action density of the smoothed fields taken at the characteristic "plateau" time $\tau = 0.5 \times 10^3$ are presented on the Fig. 3.8(a) and Fig. 3.8(c) for large and small compactification lengths L_0, accordingly. For large compactification length L_0 the action density indicates the presence of some point-like objects which manifest themselves in pronounced action lumps with the size smaller than the length of the compact direction, whereas at compactification lengths smaller than the critical length as defined by the enhancement of static correlation length the saddle points become effectively flat along the compact direction.

Presumably, the particle-like objects which we observe in the large volumes can be associated with unitons, the well know unstable saddle points of the PCM. Unitons are harmonic maps $S^2 \to SU(N)$ [98], where S^2 is obtained from $\mathbb{R}^2$ by including the point at infinity. Uniton solutions have the action which is quantized in units of

$$S_u = \frac{8\pi}{g^2} = 8\pi\beta N \tag{3.21}$$

even in the absence of any well-defined topological charge. Within characteristic plateaus during the Gradient Flow evolution, the action is clearly proportional to N (see Fig. 3.5 for illustration), and agrees with $8\pi\beta N$ ($8\pi\beta = 8.34$ for our $\beta = 0.332$) within approximately 30% uncertainty. In fact, one can't expect much better agreement due to non-zero contribution of ultraviolet fluctuations and renormalization of the coupling β along the flow time. Here we do not consider the effect of this renormalization, since numerical extraction of renormalized β would be quite complicated technically and is out of the scope of this work. The unstable nature of the uniton saddles qualitatively agrees with relatively short "life-time" of the non-perturbative objects which our Gradient Flow study reveals in the path integral of the PCM.

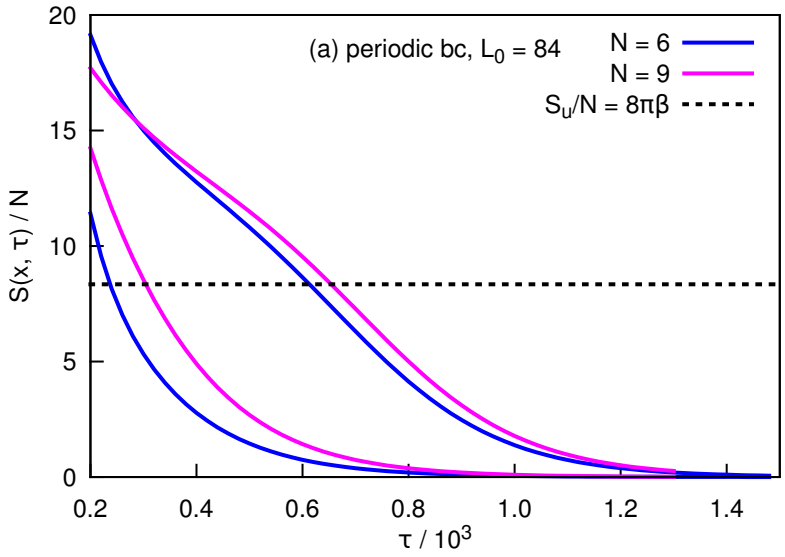

Figure 3.5: Dependence of the total action S of smoothed configurations $U(\mathbf{x}, \tau)$ (3.16) on the Gradient Flow time τ with periodic boundary conditions for $N = 6, 9$. Multiple solid lines represent independent Gradient Flows with different initial conditions $U(\mathbf{x}, \tau = 0) = U(\mathbf{x})$ chosen randomly from field configurations generated by Monte-Carlo process. The black dashed line represents the continuum action $S_u = 8\pi\beta N$ of the uniton.

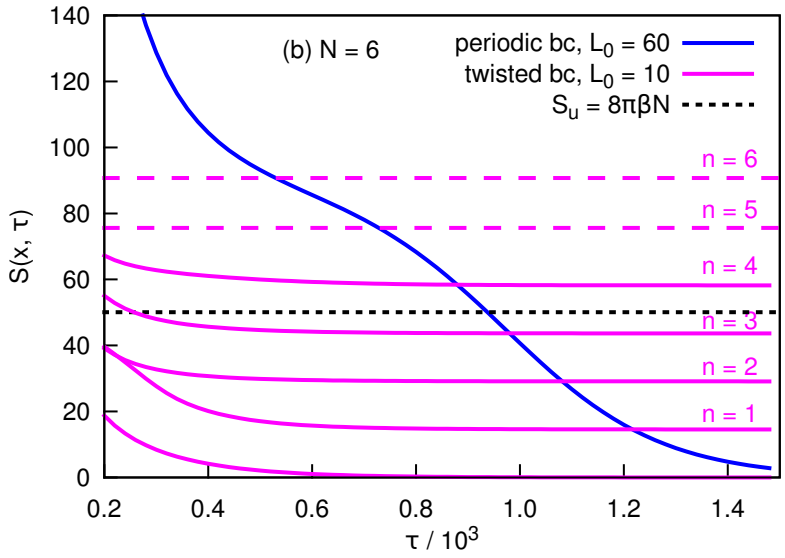

Figure 3.6: Comparison of the total action S of smoothed configurations $U(\mathbf{x}, \tau)$ (3.16) as a function of the Gradient Flow time τ for periodic and twisted boundary conditions at $N = 6$ and compactification length satisfying $NL_0^{\mathrm{TBC}} = L_0^{\mathrm{PBC}}$. Multiple solid lines represent independent Gradient Flows with different initial conditions $U(\mathbf{x}, \tau = 0) = U(\mathbf{x})$ chosen randomly from field configurations generated by Monte-Carlo process. The black dashed line represents the continuum action $S_u = 8\pi\beta$ of the uniton. Long-dashed lines of magenta color represent extrapolated plateau values $S_p(n) = nS_p(n = 1)$ for twisted boundary conditions, which presumably correspond to fracton saddle points with the action $S_f = S_u/N$.

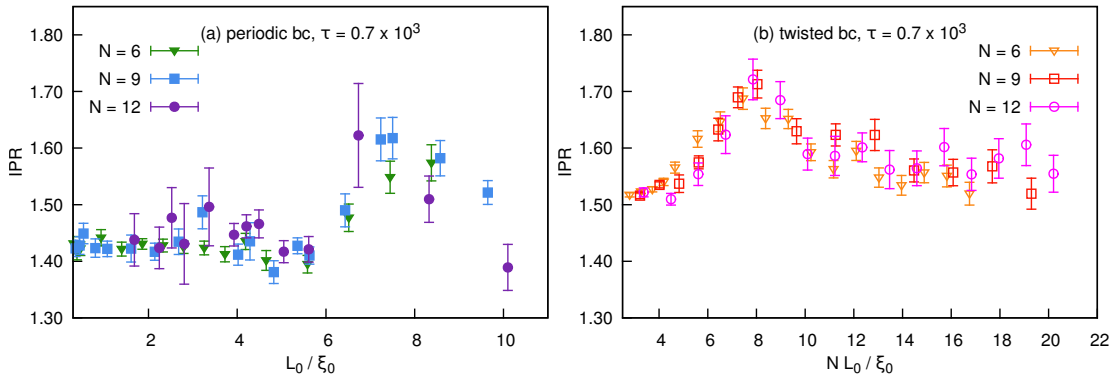

Figure 3.7: IPR (3.19) for smoothed field configurations at Gradient Flow time $\tau = 0.7 \times 10^3$ with periodic and twisted boundary conditions at different N.

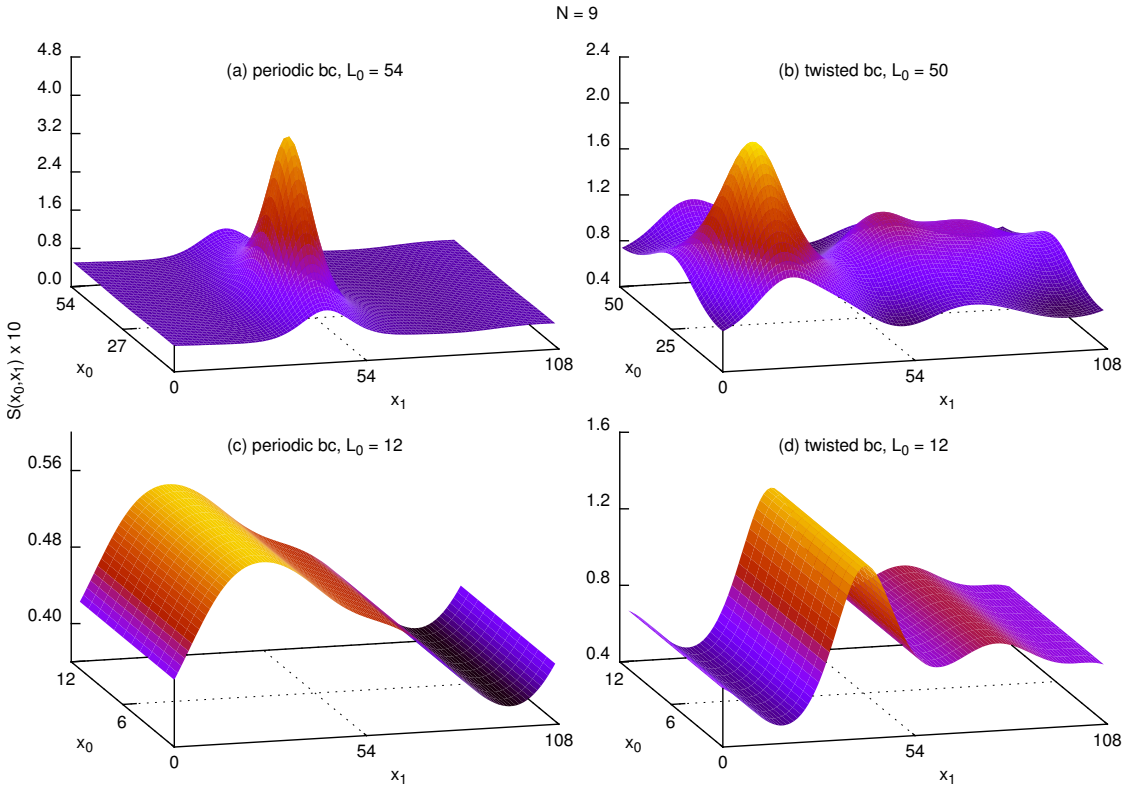

Figure 3.8: Typical action density $S(x_0, x_1)$ of smoothed field configurations $U(\mathbf{x}, \tau)$ (3.16) taken at Gradient Flow time $\tau = 0.5 \times 10^3$ with periodic and twisted boundary conditions and different compactification length L_0 at $N = 9$.

We further illustrate the dependence of the IPR (3.19) on N and L_0 with periodic boundary conditions on Fig. 3.7(a). The Gradient Flow time is fixed to $\tau = 0.7 \times 10^3$. In the low temperature region the IPR features a rather wide peak, and takes larger values as compared to high temperature phase. The presence of the peak suggests that non-perturbative objects become more localized at these values of L_0. The maximum location strongly depends on N and the flow time: we find that for larger flow times the peak moves towards larger L_0 with the shift being stronger for smaller N, which suggests that it is not directly related to the possible "deconfinement" transition discussed in Section 3.3.

Let us now turn to the Gradient Flow analysis of field configurations with twisted boundary conditions. We find that in large volume the picture is similar to the one for periodic boundary conditions. For Ünsal-Dunne regime at small L_0 we present the total action of smoothed field configurations as a function of the Gradient Flow time on Fig. 3.6 where we observe an important difference: there appear a number of well separated and very stable plateaus in the dependence of the action on the flow time, with very few transitions between them. With a rather good precision the action on these plateaus appears to linearly proportional to the plateau number, $S_p(n) = nS_p(n = 1)$, which hints at the emergence of effectively stable non-perturbative saddle points with quantized action. As for Monte-Carlo configurations the number of non-perturbative objects and hence plateaus which we observe is typically random, on Fig. 3.6 we also plot some extrapolated plateau values for larger n.

The emergence of the new type of non-perturbative objects for twisted boundary conditions could be expected, since the twist introduces non-trivial potential on $SU(N)$ manifold effectively modifying it to the maximal torus $U(1)^{N-1}$ at low energies smaller that $1/(L_0 N)$. This potential has isolated minima with associated tunneling events between them which should appear as stable saddle points in Euclidean semi-classical description where stability is ensured by winding on the maximal torus [15, 31]. These winding numbers are responsible for the emergent topological structure and the stability of non-perturbative saddles in the Ünsal-Dunne regime.

If we follow the twisted Eguchi-Kawai reduction prescription and identify compactification lengths with periodic and twisted boundary conditions as $L_0^{PBC} = NL_0^{TBC} \equiv \rho$, then from Fig. 3.6 we find that lowest plateau action in twisted case is approximately N times smaller than the uniton plateau action. Taking into account that uniton action is proportional to N, one can conclude that the lowest plateau actions is independent of N with

$$S_p^{\mathrm{TBC}}(NL_0) = S_p^{\mathrm{PBC}}(L_0)/N \tag{3.22}$$

at fixed L_0. This suggests the identification of these plateaus in the action with fracton

saddle points, which are expected to carry the action

$$S_f = S_u/N = 8\pi\beta \tag{3.23}$$

and non-trivial Kaluza-Klein (KK) momentum $\xi_{\rm KK} = -2\pi k/L_0$ [15, 31]. Counterparts of these stable fracton saddle points are well known in twisted $\mathbb{CP}^{N-1}$ model [99]: while in the large volume limit the details of boundary conditions should be irrelevant for instantons, with compactification length smaller than the size of instanton they split up to N fracton constituents which carry fractional topological charge proportional to $1/N$. Solutions of $\mathbb{CP}^{N-1}$ equation of motions can be lifted to solutions of PCM equations of motion, therefore applying this procedure to $\mathbb{CP}^{N-1}$ instanton one yields in compactified Ünsal-Dunne regime PCM unitons fractionalized into N effectively stable constituents [15, 31].

Typical action density profiles of non-perturbative objects by the Gradient Flow are given on Fig. 3.8(b) and Fig. 3.8(d) for large and small compactification length, correspondingly. As expected, we find that in the large volume non-perturbative objects are very similar to those with periodic boundary conditions. In contrast, saddles in the Ünsal-Dunne regime with twisted boundary conditions are characterized by a much larger action than in the case of periodic boundary conditions with the same L_0, and are quite strongly localized.

However, we could not clearly observed the predicted fractionalization of unitons into N fractons in the Ünsal-Dunne regime. Rather, the maximal number of peaks which we have found in smoothed configurations have never exceeded ~ 3 regardless of N. As such, however, this is not a contradiction, since the number of peaks in the action density of smoothed configurations does not necessarily coincide with the number of fractional constituents of non-perturbative saddle points. With unimproved action, these constituents typically attract each other and eventually merge during the smoothing process [100], sometimes before they become visible in the background of ultraviolet fluctuations.

The dependence of the IPR (3.19) of the non-perturbative saddle points with twisted boundary conditions is illustrated on Fig. 3.7(b). The IPR exhibits a rather sharp peak structure at intermediate values of $\rho = NL_0$, with the peak height being approximately independent of N. In contrast to periodic case, this peak moves approximately to the position of the peak in the static correlation length and at the same time becomes smaller and narrower as flow time becomes larger. This coincidence of peaks in IPR and the static correlation length might indicate some nontrivial rearrangement of non-perturbative objects in the process of transition to the Dunne-Ünsal regime. We note, however, that even for the simplest model of the ideal gas of extended non-perturbative objects the IPR might exhibit non-monotonic behavior which is just the reflection of the competition of two scales - the lattice size and the characteristic size of non-perturbative objects. Thus while the sharp peak in the IPR on Fig. 3.7(b) might be an indication of some

nontrivial transition in the structure of non-perturbative saddles, this indication should not be considered as conclusive.

3.6 Conclusions

In this work we have studied possible signatures of a crossover or a phase transition between the regimes of small and large compactification lengths L_0 for the two-dimensional $SU(N) \times SU(N)$ principal chiral model (PCM) both with periodic and with twisted boundary conditions. By analogy with other asymptotically free field theories one expects some kind of "deconfinement" transition for periodic boundary conditions [31]. According to the adiabatic continuity conjecture, the twist is expected to eliminate this transition [15, 31, 81], so that the regimes of small and large compactification lengths can be analytically related.

In the absence of well-defined local order parameters such as e.g. Polyakov loop, we have considered universal physical observables which can characterize phase transitions regardless of the symmetries of the system: mean energy, specific heat and static correlation length. We have found that for both types of boundary conditions these quantities behave in a way which is compatible with the signatures of a rather weak crossover or a phase transition: mean energy and specific heat exhibit monotonic growth/decrease with compactification length once it is sufficiently small, and the static correlation length is enhanced near some "critical" compactification length.

An important difference between the two boundary conditions is that for periodic boundary conditions the peak in the correlation length becomes somewhat higher and narrower as the $SU(N)$ rank N is increased. It also becomes slightly higher for larger lattice volumes. Since the large-N limit can be also considered as thermodynamic limit within the range of validity of Eguchi-Kawai reduction, this behavior suggests that PCM with periodic boundary conditions might indeed feature a finite-temperature phase transition, at least in the large-N limit.

In contrast, for twisted boundary conditions the shape of the peak in the static correlation length is independent of N, once the data is considered as a function of the combined length parameter $\rho = NL_0$. The dependence of the peak height on the spatial lattice size also cannot be distinguished within statistical errors. This behaviour is not typical for a phase transition, but can be still compatible with a weak crossover. If true, the crossover scenario would be a challenge for the continuity conjecture, since the phases separated by the crossover typically cannot be analytically related to each other (a classical example is the Berezinskii–Kosterlitz–Thouless transition).

By using the Gradient Flow, we have also studied the structure of non-perturbative saddle points which dominate the path integral of the PCM with both boundary conditions. We have found localized non-perturbative object with the properties expected for unitons,

the unstable saddle points of the continuum PCM. In particular, these objects have quantized action which scales linearly with N. As expected, they also become effectively stable for twisted boundary conditions, thus exhibiting the phenomenon of emergent topology [15]. We also find that for twisted boundary conditions the geometric properties of non-perturbative saddles change precisely at the position of the possible crossover to the Dunne-Ünsal regime, which is yet another argument that this crossover might be non-trivial.

Chapter 4

Lefschetz thimbles and the sign problem in two-dimensional Hubbard model

4.1 Introduction

The Hubbard model has been the focus of intense theoretical and numerical research for decades since its introduction as a model for strongly-correlated electrons in condensed matter physics [36, 37]. Those studies became especially important when it was realized that the physics of high-temperature superconductors can be approximately described by the two-dimensional Hubbard model with finite chemical potential [38, 39]. However, despite large efforts made in this field [40], there is still no comprehensive analytic or numerical method which can solve the Hubbard model for arbitrary parameters.

In this Chapter, we investigate improvements of the determinantal Quantum Monte Carlo (QMC) method which is one of the most common numerical techniques applied in studies of the Hubbard model. The main advantage of this method is that it does not involve any additional physical assumptions beyond those made to derive the interacting tight-binding Hamiltonian. Thus, QMC results are among the most reliable in the field. However, QMC often suffers from the sign problem, when a strongly fluctuating phase factor appears in the final integrals. In particular, the most interesting case, that of the square lattice Hubbard model away from half filling, suffers from the sign problem which prevents a comprehensive study of the superconducting state.

The most recent approach to the sign problem in Monte Carlo simulations has its origin in the so-called Lefschetz thimble decomposition of the path integral [18, 19], which can be considered as a multidimensional generalization of the stationary phase method. Namely, the integration contour of the partition function is deformed into complex domain such that original integral is represented as a sum of integrals over

steepest descent manifolds ("Lefschetz thimbles") originating from critical points of the action. Complex phases of integrands are constant on those manifolds, thus it is possible to use this property in order to solve or at least soften the sign problem. This approach was first proposed as a possible solutions of the sign problem in lattice Quantum Chromodynamics (QCD) at finite chemical potential [101, 102] and investigated in a number of papers [103–108]. It was also employed for non-perturbative calculation of quantum corrections to mean field solutions in the Hubbard model [109].

The naive Lefschetz thimbles approach requires the knowledge of all saddle points in the space of complex fields and involves integration over non-trivial manifolds, which is typically a very challenging problem. In order to overcome this difficulty it was recently proposed to construct a contour in complex space (the so-called Generalized thimble) which approximates Lefschetz thimbles without *a priory* knowledge of saddle points and thimbles [110–112], and thus reduce fluctuations of the complex phase. This can be achieved with the help of Holomorphic flow [110, 111, 113] or using Machine Learning methods [112, 114, 115]. With these numerical developments it became possible to simulate at least some simple models [112, 116] on relatively small lattices.

One should keep in mind that this is not a complete solution of the sign problem in every case, but a way to make the problem milder by suppressing fluctuations of the phase factor appearing under the integral.

Despite these improvements of numerical algorithms, the number of Lefschetz thimbles needed to approach the true value of the initial integral remains one of the most important characteristics which quantifies the utility of these methods. The reason for that is twofold. First of all, the sign problem might return in the form of the sum over contributions from different Lefschetz thimbles where each term has its own complex phase. As was shown in [117], already on the trivial example of the one-site Hubbard model, this problem can be very dramatic. On the other hand, for the algorithms mentioned above it is important to have as small number of contributing thimbles as possible because the underlying probability distribution appears to be strongly multimodal [118, 119] and the algorithm tends to sample the vicinity of some thimble and does not explore other thimbles.

In this work we explore various variants of the path integral representation of the Hubbard model based on different representations of the four-fermionic interaction term. Some of them are based on a conventional Hubbard-Stratonovich transformation with Gaussian integrals and one is based on a newly developed integral representation which mimics the discrete transformation used in Blankenbecler-Scalapino-Sugar (BSS) QMC. We show that the number of Lefschetz thimbles and thus the complexity of the sign problem is very dependent on the particular representation. On the basis of our analysis we propose the regimes with substantially reduced number of relevant thimbles. These regimes are the most promising for the Generalized thimble algorithm. Combining these

approaches with recently developed algorithms [110, 116], one can try to explore the phase diagram of the Hubbard model at higher chemical potential and lower temperature than was previously possible with existing QMC schemes.

The material is organized as follows. In the first section, we give some basic definitions and make a brief review of the mathematical basis for existing determinantal QMC algorithms. We also give a short introduction to the Lefschetz thimbles method. In the next section we study the scaling of the number of relevant thimbles with increasing lattice size for the few-site Hubbard model in the case when conventional Gaussian Hubbard-Stratonovich (HS) transformation is used for the decomposition of the interaction term. Here we identify the regime with the minimal number of relevant thimbles. In the third section we present results of test QMC calculations complementary to the findings presented in the previous section. The fourth section is devoted to the derivation of an alternative non-Gaussian path integral representation and its application to the simplest examples of the one-site Hubbard model and the few-site Hubbard model.

4.2 Basic definitions

4.2.1 The model

QMC algorithms usually deal with the path integral representation of the partition function

$$\mathcal{Z} = \mathrm{Tr}\, e^{-\beta \hat{H}}, \tag{4.1}$$

and the corresponding thermodynamic averages of observables

$$\langle \hat{O} \rangle = \frac{1}{\mathcal{Z}} \mathrm{Tr}\, (\hat{O} e^{-\beta \hat{H}}). \tag{4.2}$$

Here $\hat{H}$ and $\hat{O}$ are the Hamiltonian and some observable respectively and β is the inverse temperature. The Hamiltonian $\hat{H}$ usually consists of two parts:

$$\begin{aligned} \hat{H} &= \hat{H}_{(2)} + \hat{H}_{(4)} = \\ = \sum_{x,y,\sigma,\sigma'} t_{xy\sigma\sigma'} \hat{c}^{\dagger}_{x\sigma} \hat{c}_{y\sigma'} &+ \sum_{x,y,\sigma,\sigma'} U_{xy\sigma\sigma'} \hat{n}_{x\sigma} \hat{n}_{y\sigma'}, \end{aligned} \tag{4.3}$$

where indexes x and y denote lattice sites, $\sigma, \sigma' = \uparrow, \downarrow$ correspond to spin index and $\hat{n}_{x\sigma} = \hat{c}^{\dagger}_{x\sigma} \hat{c}_{x\sigma}$. The first part contains only bilinear fermionic terms which includes a tight-binding part as well as the chemical potential. The second part contains four-fermionic terms describing electron-electron interaction. We have included in (4.3) the most general interaction term, which can be referred to as the "extended Hubbard model". The Hubbard model itself includes only local on-site interaction $\sum_x U \hat{n_{x\uparrow}} \hat{n_{x\downarrow}}$.

The path integral representation of the partition function (4.1) starts from the Trotter decomposition:

$$\mathrm{Tr}\, e^{-\beta \hat{H}} \approx \mathrm{Tr}\, \left(e^{-\delta \hat{H}_{(2)}} e^{-\delta \hat{H}_{(4)}} e^{-\delta \hat{H}_{(2)}} e^{-\delta \hat{H}_{(4)}} \ldots \right). \tag{4.4}$$

After the decomposition we have a product of N_t exponentials, which constitutes the Euclidean time extent of the lattice. δ is the step in Euclidean time: $N_t\delta = \beta$. To transform the trace to the path integral representation, one introduces Grassmann coherent states $|\xi\rangle$ and Grassmann variables ξ for each creation and annihilation operator. Further details of the construction of the path integral representation can be found in [120–122], where it was done for Hubbard-Coulomb model on hexagonal lattice.

We would like to highlight one stage in this derivation which is important for our study of the sign problem. Namely, the four-fermionic term $\hat{H}_{(4)}$ in the full Hamiltonian (4.3) should be converted into a fermion bilinear. This step is essential, because for the bilinear terms in the exponent we have a simple set of relations which allows us to convert the multidimensional integral over Grassmann variables into the form convenient for a Monte Carlo scheme.

There are two different ways to convert the interaction term into bilinear form. The first scheme is based on discrete auxiliary variables [123, 124]. An example of such a transformation follows from the identity:

$$e^{-\delta U \hat{n}_\uparrow \hat{n}_\downarrow} = \frac{1}{2} \sum_{\nu=\pm 1} e^{2i\xi\nu(\hat{n}_\uparrow + \hat{n}_\downarrow - 1) - \frac{1}{2}\delta U(\hat{n}_\uparrow + \hat{n}_\downarrow - 1)}, \tag{4.5}$$

$$\tan^2 \xi = \tanh(\frac{\delta U}{4}).$$

Note that the exponents on the r.h.s. of this identity are purely imaginary for repulsive interactions $U > 0$. One can also write a variant of this transformation leading to purely real exponents. This and similar representations are used in the Blankenbecler-Scalapino-Sugar (BSS) QMC algorithm which is widely applied to the physics of the Hubbard model [125, 126]. Another variant is based on the usual Gaussian HS transformation:

$$e^{-\frac{\delta}{2}\sum_{x,y} U_{x,y}\hat{n}_x\hat{n}_y} \cong \int D\phi_x e^{-\frac{1}{2\delta}\sum_{x,y}\phi_x U^{-1}_{xy}\phi_y} e^{i\sum_x \phi_x \hat{n}_x}, \tag{4.6}$$

$$e^{\frac{\delta}{2}\sum_{x,y} U_{x,y}\hat{n}_x\hat{n}_y} \cong \int D\phi_x e^{-\frac{1}{2\delta}\sum_{x,y}\phi_x U^{-1}_{xy}\phi_y} e^{\sum_x \phi_x \hat{n}_x}. \tag{4.7}$$

It can be used in two variants leading to real (4.7) and complex (4.6) exponents. This representation has an important advantage in that it also works for non-local interactions, so that we do not need to introduce a new auxiliary field for every pair of interacting electrons. Thus it was used, for instance, for the Hubbard-Coulomb model [121, 127–130]. However, in the case of pure Hubbard model with only on-site interaction the number of discrete auxiliary fields in the first representation (4.5) is equal to the number of continuous fields in (4.6) or (4.7). Thus, due to smaller configuration space, the discrete representation is more advantageous at least if the sign problem is absent.

Now let's turn to the appearance of the sign problem. In special cases where some additional symmetries (e.g. the time-reversal symmetry [131]) exist, the extended Hubbard model is accessible to QMC simulations. In particular, they are possible in the case of a

bipartite lattice. Thus we are going to concentrate on the following Hamiltonian written on a bipartite lattice with only the on-site interaction term:

$$\hat{H} = -\kappa \sum_{\langle x,y\rangle,\sigma} \hat{c}^{\dagger}_{x\sigma}\hat{c}_{y\sigma} \quad + \quad U\sum_{x} \hat{n}_{x\uparrow}\hat{n}_{x\downarrow} - \\ - \left(\frac{U}{2} - \mu\right)\sum_{x}(\hat{n}_{x\uparrow} \quad + \quad \hat{n}_{x\downarrow} - 1). \tag{4.8}$$

The tight-binding part includes only hopping to nearest neighbors. The chemical potential μ defines the shift from half-filling, which corresponds to $\mu = 0.0$ in our notation. QMC algorithms in ideal situation (in the absence of the sign problem) need at least a semi-positive weight for auxiliary fields. The bipartite lattice provides us with this possibility at half-filling, after a well-known trick which transforms spin-up and spin-down electrons ($\hat{c}_{x,\uparrow}$ and $\hat{c}_{x,\downarrow}$) to electrons and holes ($\hat{a}_x$ and $\hat{b}_x$):

$$\begin{cases} \hat{c}_{x,\uparrow}, \hat{c}^{\dagger}_{x,\uparrow} \rightarrow \hat{a}_x, \hat{a}^{\dagger}_x, \\ \hat{c}_{x,\downarrow}, \hat{c}^{\dagger}_{x,\downarrow} \rightarrow \pm\hat{b}^{\dagger}_x, \pm\hat{b}_x \end{cases}, \tag{4.9}$$

where the sign in the second line alternates depending on the sublattice. The Hamiltonian (4.8) acquires the following form after the transition to the new variables :

$$\hat{H} = -\kappa \sum_{\langle x,y\rangle}(\hat{a}^{\dagger}_x\hat{a}_y + \hat{b}^{\dagger}_x\hat{b}_y) \quad + \quad \frac{U}{2}\sum_{x}(\hat{n}_{x,el.} - \hat{n}_{x,h.})^2 + \\ +\mu\sum_{x}(\hat{n}_{x,el.} - \hat{n}_{x,h.}), \tag{4.10}$$

where $\hat{n}_{x,el.} = \hat{a}^{\dagger}_x\hat{a}_x$ and $\hat{n}_{x,h.} = \hat{b}^{\dagger}_x\hat{b}_x$ are the particle number operators for electrons and holes respectively.

Now we should make either the discrete (4.5) or the continuous (eq. (4.6) and (4.7)) transformation for each exponent in the expression (4.4) where the interaction part of the full Hamiltonian appears. Thus, auxiliary fields acquire the Euclidean time index t in addition to the spatial lattice site index x. Since the interaction is local, only one auxiliary field variable will appear per lattice site in both cases. In the case of the discrete transformation (4.5), we arrive at the following representation of the partition function (4.1) as a sum over all possible values of $\nu_{x,t}$:

$$\mathcal{Z}_d = \sum_{\nu_{x,t}} \det\left(D\right)_{el.}(\nu_{x.t})\det\left(D\right)_{h.}(\nu_{x,t}), \tag{4.11}$$

where $D_{el.}$ and $D_{h.}$ are fermionic operators for electrons and holes respectively:

$$D_{el.}(\nu_{x,t}) = I + \prod_{t=1}^{N_t}\left(e^{-\delta(h+\mu)}\mathrm{diag}\left(e^{2i\xi\nu_{x,t}}\right)\right), \\ D_{h.}(\nu_{x,t}) = I + \prod_{t=1}^{N_t}\left(e^{-\delta(h-\mu)}\mathrm{diag}\left(e^{-2i\xi\nu_{x,t}}\right)\right). \tag{4.12}$$

Both fermionic operators are $N_s \times N_s$ matrices where N_s is the number of lattice sites in space, h is the matrix of single-particle Hamiltonian which defines the tight-binding part in the expression (4.10). The diagonal $N_s \times N_s$ matrix $\mathrm{diag}\left(e^{-2i\xi\nu_{x,t}}\right)$ includes all exponents with auxiliary fields belonging to a given Euclidean time slice t.

In the case of continuous auxiliary fields, we will write the HS transformation in more general way employing both real (4.7) and complex (4.6) exponents:

$$\frac{U}{2}(\hat{n}_{el.} - \hat{n}_{h.})^2 = \frac{\alpha U}{2}(\hat{n}_{el.} - \hat{n}_{h.})^2 - \\ -\frac{(1-\alpha)U}{2}(\hat{n}_{el.} + \hat{n}_{h.})^2 + (1-\alpha)U(\hat{n}_{el.} + \hat{n}_{h.}). \tag{4.13}$$

Parameter $\alpha \in [0, 1]$ defines the balance between real and complex exponents in the integral. The first four-fermionic term can be transformed into bilinear using (4.6) and the second using (4.7). This is not the most general possible decomposition of four-fermionic terms into bilinear ones, but the most commonly used in QMC algorithms with continuous auxiliary fields. This representation was first proposed in [132] and was also used in the recent paper [133]. The partition function can be written as the following integral:

$$\mathcal{Z}_c = \int \mathcal{D}\phi_{x,t}\chi_{x,t} e^{-S_\alpha} \det\left(M\right)_{el.} \det\left(M\right)_{h.}, \\ S_\alpha(\phi_{x,t}, \chi_{x,t}) = \sum_{x,t} \frac{\phi_{x,t}^2}{2\alpha\delta U} + \sum_{x,t} \frac{(\chi_{x,t} - (1-\alpha)\delta U)^2}{2(1-\alpha)\delta U}, \tag{4.14}$$

where fermionic operators for continuous auxiliary fields are written as

$$M_{el.} = I + \prod_{t=1}^{N_t} \left(e^{-\delta(h+\mu)} \mathrm{diag}\left(e^{i\phi_{x,t}+\chi_{x,t}}\right)\right), \\ M_{h.} = I + \prod_{t=1}^{N_t} \left(e^{-\delta(h-\mu)} \mathrm{diag}\left(e^{-i\phi_{x,t}+\chi_{x,t}}\right)\right). \tag{4.15}$$

In subsequent derivations we will deal with the full action which includes both quadratic form and the logarithms of the fermionic determinants:

$$S = S_\alpha - \ln(\det\left(M\right)_{el.} \det\left(M\right)_{h.}). \tag{4.16}$$

In all cases, we disregard constant multipliers in the integrals since they are cancelled in the computation of observables (4.2). An important point is that both representations of the partition function reproduce the exact result only in the limit $\delta \to 0$ due to approximations introduced by the Trotter decomposition (4.4).

One can easily see that the fermionic determinants for electrons and holes both in the discrete and the continuous cases are complex conjugated to each other at half filling. This means that we can safely use the expressions under the sum in (4.11) or the integral in (4.14) as the weight for sampling auxiliary fields. Away from half-filling, we should

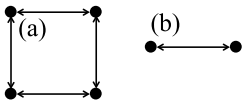

Figure 4.1: Lattices studied in this work: (a) 4-site and (b) two-site. The arrows denote hoppings between lattice sites.

employ "reweighting" where auxiliary fields are sampled according to the modulus of the corresponding expressions in (4.11) or (4.14) and the remaining complex phase factor is included in observable. However, this procedure suffers from cancellation of terms with opposite phases and thus its domain of applicability is limited to rather low values of the chemical potential and rather high temperatures.

Despite being less effective for the pure Hubbard model with only on-site interaction, the second approach has one important advantage away from half-filling. Since it is based on continuous variables, the integration manifold can be shifted from real space to complex space, leading to the "complexification" of the auxiliary fields. If no singular points are crossed during this shift, Cauchy's integral theorem guarantees the same answer. The alternative integration manifold in the complex plane can be chosen in a special way to reduce the fluctuations of the phase of the integrand in eq. (4.14). This is the main idea of the Generalized thimbles algorithm.

Since the finding of Lefschetz thimbles in many-dimensional complex space is a non-trivial numerical task, we will explicitly consider only the small lattices with $N_s = 1, 2, 4$ and $N_t = 1, 2, 3, 4$. Corresponding square lattices with two and four sites and periodical boundary conditions are shown in the figure 4.1. The hopping amplitude κ can be any complex number, only hoppings to nearest-neighbours are taken into account. The single-particle Hamiltonian takes the form

$$h = \begin{pmatrix} 0 & -\kappa \\ -\bar{\kappa} & -0 \end{pmatrix} \tag{4.17}$$

when $N_s = 2$ and

$$h = \begin{pmatrix} 0 & -\kappa & -\kappa & 0 \\ -\bar{\kappa} & 0 & 0 & -\kappa \\ -\bar{\kappa} & 0 & 0 & -\kappa \\ 0 & -\bar{\kappa} & -\bar{\kappa} & 0 \end{pmatrix}. \tag{4.18}$$

when $N_s = 4$. For the one-site Hubbard model the Hamiltonian h can obviously be disregarded. One should also note that the case of $N_t = 1$ is exact for the one-site Hubbard model as there is no error associated with the discretization of Euclidean time. Indeed, there are no alternating exponents in the Trotter decomposition (4.4) if the tight-binding part is absent. Thus it is sufficient to have only one step in Euclidean time. It automatically guarantees that the path integral representation (4.11) or (4.14) exactly reproduces the initial partition function (4.1).

Despite the very limited system sizes under consideration, all approaches we discuss are still fully applicable for real computations on lattices with large N_s and N_t.

4.2.2 Lefschetz thimbles method

In order to illustrate the basic ideas of the Lefschetz thimbles method, we start from the most general form of integrals appearing in QMC with continuous auxiliary fields:

$$\mathcal{Z}\left(\beta,\mu,\dots\right)=\int_{\mathbb{R}^N} d^N x e^{-S(\beta,\mu,\dots,x)}. \tag{4.19}$$

If we consider continuation of this integral in domain of complex-valued variables $x \in \mathbb{C}^N$, then due to Cauchy theorem one can choose any appropriate contour in complex space for integration. A representation with particularly useful properties can be constructed with the help of Morse theory (or Picard-Lefschetz theory) and is known as Lefschetz thimble decomposition of the path integral [18, 19]:

$$\mathcal{Z}\left(\beta,\mu,\dots\right) = \sum_{\sigma} k_\sigma\left(\beta,\mu,\dots\right)\mathcal{Z}_\sigma\left(\beta,\mu,\dots\right), \tag{4.20}$$

$$\mathcal{Z}_\sigma\left(\beta,\mu,\dots\right) = \int_{\mathcal{I}_\sigma(\beta,\mu,\dots)} d^N x e^{-S(\beta,\mu,\dots,x)}, \tag{4.21}$$

where σ labels all complex saddle points $z_\sigma\left(\beta,\mu,\dots\right) \in \mathbb{C}$ of the action:

$$\left.\frac{\partial S}{\partial x}\right|_{x=z_\sigma(\beta,\mu,\dots)} = 0, \tag{4.22}$$

integer-valued coefficients $k_\sigma\left(\beta,\mu,\dots\right)$ are so-called intersection numbers and $\mathcal{I}_\sigma\left(\beta,\mu,\dots\right)$ are steepest descent (Lefschetz thimble) manifolds. Here we have emphasized dependence of all important quantities and objects on parameters for clarity and will omit this in what follows. This relation is valid if saddle points are non-degenerate and isolated (for generalization in the case of gauge theory see [18]). Degenerate saddle points can appear due to spontaneous breaking of some continuous symmetry, and in this case, the symmetry should be explicitly broken by some small term in Hamiltonian and all results should be extrapolated to the limit where the symmetry is restored.

In order to construct the Lefschetz thimble manifold $\mathcal{I}_\sigma$ corresponding to a given complex saddle point z_σ we use the gradient flow equation:

$$\frac{dx}{d\tau} = \overline{\frac{\partial S}{\partial x}}, \tag{4.23}$$

with the following boundary conditions:

$$x \in \mathcal{I}_\sigma : x(\tau) = x, x(\tau \to -\infty) \to z_\sigma. \tag{4.24}$$

This equation defines the evolution of the complex variable x with respect to the fictitious flow time τ, and all such solutions constitute the thimble manifold.

Analogously, we define another important type of manifold, the so-called anti-thimble $\mathcal{K}_\sigma$ which consist of all possible solution of the flow equations (4.23) which end up at a given saddle point z_σ:

$$x \in \mathcal{K}_\sigma : x(\tau) = x, x(\tau \to +\infty) \to z_\sigma. \tag{4.25}$$

With the help of anti-thimbles one can compute integer-valued coefficients k_σ in the expression (4.20) by counting the number of intersection of $\mathcal{K}_\sigma$ with original integration contour $\mathbb{R}^N$:

$$k_\sigma = \langle \mathcal{K}_\sigma, \mathbb{R}^N \rangle. \tag{4.26}$$

Both thimbles and anti-thimbles are N-dimensional real manifolds in $\mathbb{C}^N$. Two basic properties which make them useful are the following. First of all, the real part of the action $\operatorname{Re} S$ monotonically increases along the thimble and monotonically decreases along the anti-thimble if we start from the saddle point. Secondly, the imaginary part of the action $\operatorname{Im} S$ stays constant along both of them. It follows that neither thimbles nor anti-thimbles can intersect each other, neither of saddle points can be connected by some thimble in a general situation (with a very important exception which is discussed below) and all integrals on the r.h.s. of the expression (4.20) are convergent.

It is due to constant complex phases on thimbles this method became attractive for studying the sign problem in QMC simulations. There is nevertheless a residual sign problem due to non-trivial complex-valued volume element on the thimble which is however soft and can be overcome. In practice, thimbles can be constructed using their tangent spaces in the vicinity of saddle points. Namely, at each saddle point we can compute $2N \times 2N$ matrix of the second derivatives of $\operatorname{Re} S$ over real and imaginary part of complex variable x. This matrix has exactly N positive and N negative eigenvalues. The corresponding eigenvectors define the tangent space for the thimble and the anti-thimble respectively and provide us with initial conditions for the flow equations.

The main subtlety in this theory is a Stokes phenomenon which happens when at some values of parameters (so-called Stokes rays) there exist two or more distinct saddle points connected by some thimble. This can only happen when the imaginary part of actions at these saddle points coincide: $\operatorname{Im} S(z_\sigma) = \operatorname{Im} S(z_{\sigma'})$. Then thimble integrals $\mathcal{Z}_\sigma$ associated with these saddle points exhibit jumps which should be compensated by the jump in coefficients k_σ in order to ensure validity of Cauchy theorem. Jumps in intersection numbers appear due to change in the structure of anti-thimbles. Consequently, some coefficients k_σ might become zero or non-zero and the structure of the sum (4.20) can change dramatically, thus any reasonable QMC algorithm based on the thimble decomposition should correctly account for them. This makes direct application of the thimble decomposition very impractical, however the very existence of such decomposition motivates development of algorithms which will approximate thimbles in some automatic manner and minimize sign problem, like those mentioned in the introduction.

The general sign problem generated by the fluctuating phase in (4.19) is substituted by the sign problem generated by different phase factors appeared in the sum over thimbles (4.20):

$$\mathcal{Z} = \sum_{\sigma} k_{\sigma} e^{-i \operatorname{Im} S(z_{\sigma})} \int_{\mathcal{I}_{\sigma}} d^{N} x e^{-\operatorname{Re} S(x)}, \tag{4.27}$$

where we write down complex factors associated with different saddle points explicitly. We say that thimble is "relevant" if it has a nonzero intersection number k_{σ} and thus participates in this sum. The number of relevant thimbles, their weight, and the distribution of imaginary part of action at corresponding (relevant) saddle points define the remaining complexity of the sign problem. The smaller the number of relevant saddle points, the less severe the sign problem in (4.20). An ideal situation is of course when we have just one relevant thimble or if only one thimble is important in the sum (4.20) due to dominating absolute value of integral over it.

4.2.3 Hybrid Monte Carlo and problems with ergodicity

Hybrid Monte Carlo (HMC) algorithm is now the most widely used technique to update continuous fields during the Markov process in QMC [134]. Details of this method impose some limitations on the possible path integral representations, so we give the brief description of the method. In HMC we employ artificial dynamics to make the updates of continuous fields. The main steps in the algorithm can be described as follows:

- Artificial momentum $\theta_{x,t}$ is introduced for each continuous auxiliary field $\psi_{x,t}$.
- The classical Hamiltonian for the artificial evolution is written as $H = 1/2 \sum_{x,t} \theta_{x,t}^2 + S(\psi_{x,t})$, where the action $S(\psi_{x,t})$ includes both quadratic form and logarithms of fermionic determinants (see eq. (4.16)).
- The update of both auxiliary fields and momenta is performed through the solution of classical dynamics equations according to this Hamiltonian. The Metropolis accept-reject step is made in the end of trajectory.

Hamiltonian updates used in HMC impose important limitation on the ergodicity of the method. Namely, these updates can not penetrate through the manifolds formed by configurations with zero fermionic determinant, because the action $S(\psi_{x,t})$ goes to infinity at these configurations. If the dimensionality of these manifolds is equal to $N-1$ within the general N-dimensional integration manifold, then we have "domain walls" and the single HMC process can do only integration within the single region surrounded by domain walls. In order to penetrate though the domain walls we need some other, non-Hamiltonian updates. Below we will show that this situation indeed emerges in some particular cases for the path integrals for the Hubbard model.

If $\alpha = 0$ the complex exponents and the auxiliary fields $\phi(x,t)$ disappear from the integral (4.14) and fermionic determinants both for electrons and holes are purely real functions. They are identical at half-filling and start to differ at nonzero μ thus the fluctuating sign (but not complex phase) appears in the integrand in (4.14). Since all functions are real, all relevant saddle points and thimbles are also within the real subspace $\mathbb{R}^N$. It means that we are automatically within the representation of the partition function through the sum over thimbles (4.20) even without any shift to the complex plane: the real subspace is simply divided between thimbles attached to relevant real saddles. Thus we do not even need to search for some manifolds in complex space. Away from half-filling some of these saddles have positive sign and some of them have negative sign. Simple counting of degrees of freedom shows that the manifold of the zero points of determinant $\det(M)_{el.} \det(M)_{h.}$ has dimensionality $N-1$ in $\mathbb{R}^N$ in general case. It means that the regions belonging to different thimbles in $\mathbb{R}^N$ are separated by "domain walls" of configurations with zero probability and HMC can not explore the full phase space, even at half filling. This phenomenon was already observed in [109, 133], where the representation with only real exponents was used for QMC calculations. This is not an issue if we already know in advance the dominant saddle(s) and want to compute integrals over corresponding thimbles as it was done in [109], but ideally one should construct some numerical procedure which doesn't need *a priori* knowledge.

The same situation with "domain walls" emerges also in the opposite limit where $\alpha = 1$ and real exponents completely disappear from the integral (4.14). In this case, we can make the Hubbard-Stratonovich transformation coupling the auxiliary field with spin degrees of freedom and compare the final integral with the one derived in terms of electrons and holes (4.15). If there are only hoppings between sublattices (no mass term and no chemical potential is introduced), the following relation for the fermionic operator in (4.15) can be proved for $\alpha = 1$:

$$\det(M)_{el.}(\phi_{x,t}) = F(\phi_{x,t}) e^{i\sum_{x,t}\phi_{x,t}}. \tag{4.28}$$

The function $F(\phi_{x,t})$ is real and it is not equal to the sum of squares, it can change the sign. The overall product of determinants

$$\det(M)_{el.} \det(M)_{h.} = F(\phi_{x,t})^2 \tag{4.29}$$

is again equal to the square of some real function. It means that if the zero points of determinant exist (if they are not eliminated by, e.g. some explicit mass term in one-particle Hamiltonian), their manifold again has dimensionality $N-1$ in $\mathbb{R}^N$. This fact can be noticed already in the simplest case of the lattice with $N_s = 2$ and $N_t = 1$. The fermionic determinant for this lattice takes the form

$$\det(M)_{el.} \det(M)_{h.} = e^{-2\beta\kappa} \times \left((1 + e^{2\beta\kappa}) \cos(\frac{\phi_1 - \phi_2}{2}) + 2e^{2\beta\kappa} \cos(\frac{\phi_1 + \phi_2}{2}) \right)^2 \tag{4.30}$$

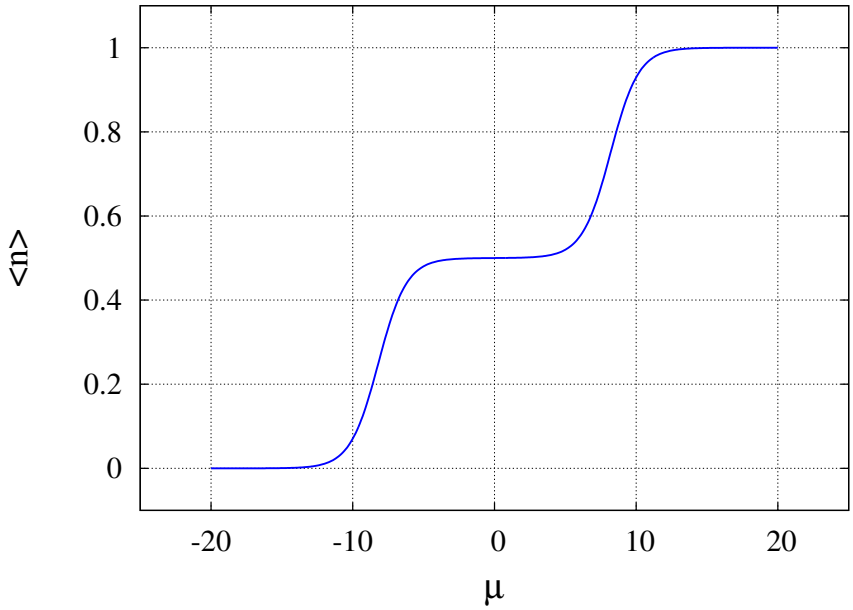

Figure 4.2: Average number of particles $\langle \hat{n} \rangle = \langle \hat{a}^\dagger \hat{a} \rangle$ for the one-site Hubbard model. $U\beta = 15.0$.

in the limit $\alpha = 1$.

We see that both limits of purely complex ($\alpha = 1$) and purely real ($\alpha = 0$) exponents are not entirely suitable for the HMC simulations due to the "domain walls" within the integration domain. Here we should stress again that insertion of explicit mass term in one-particle Hamiltonian as it was made in previous calculations on hexagonal lattice [121, 122, 135] completely eliminates the problems with ergodicity since configurations with zero fermionic determinant are absent [120]. The price is that the mass term can introduce bias towards some particular channel of spontaneous symmetry breaking. Thus, if we want to make calculations without this bias, some intermediate value of α should be used. First, we analyze both cases of $\alpha = 1$ and $\alpha = 0$ in order to give a comprehensive picture of the sign problem. Then we study intermediate values of α where the situation smoothly evolves between these too limits.

4.3 Lefschetz thimbles and Gaussian Hubbard-Stratonovich transformation

Now we are going to explore how the Lefschetz thimbles approach works for different variants of Gaussian HS transformation. In order to estimate the complexity of the sign problem, we estimate the number or relevant thimbles, calculate their phases and estimate their weight in the sum (4.20). We use built-in routine *FindRoot* from *Mathematica* in order to find saddle points and routine *NDSolve* in order to solve the flow equations (4.23). In this exploratory study we restrict ourselves to quite small lattice sizes because we use

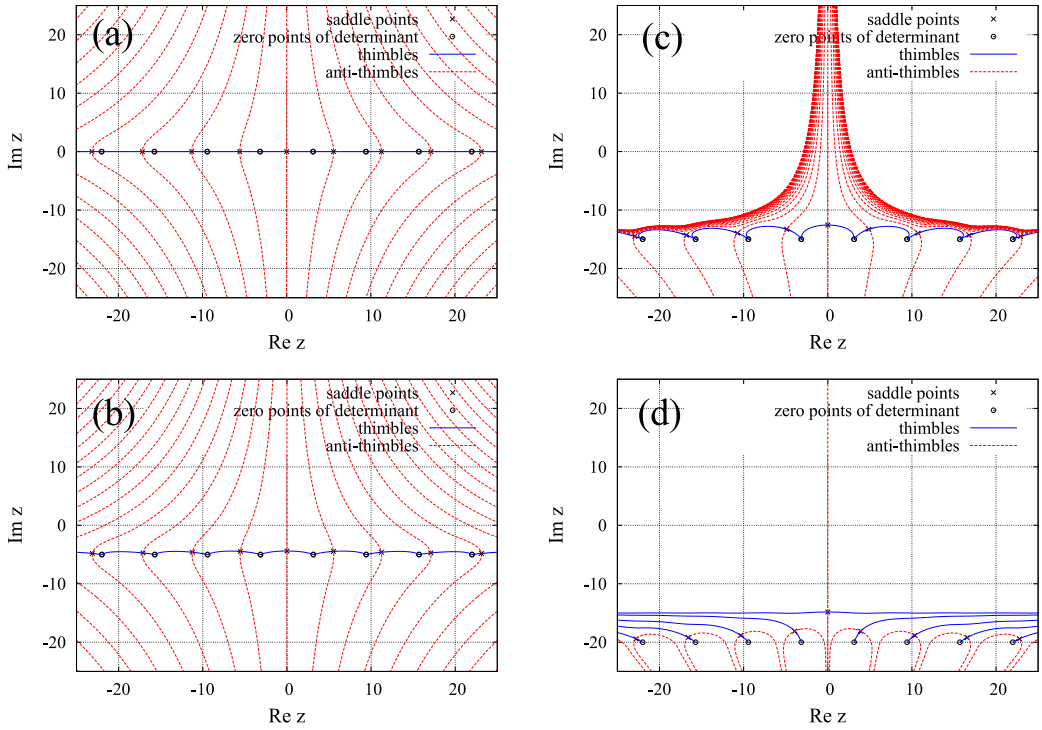

Figure 4.3: Thimbles and anti-thimbles for one-site Hubbard model in the Gaussian representation at various values of chemical potential.The action is written in (4.34), $U\beta = 15.0$. (a) Half filling ($\mu = 0$). The real axis is divided by "zeros" of fermionic determinant into infinite number of thimbles. Corresponding anti-thimbles end up at infinity $\mathrm{Im}\, z \to \pm\infty$. (b) $\beta\mu = 5.0$. The number of relevant thimbles is still infinite but all relevant saddles are shifted in the complex plane from the real axis. (c) $\beta\mu = 15.0$. There is still infinite number of relevant saddles, but the Stokes phenomenon is very close to appearance. (d) $\beta\mu = 20.0$. The Stokes phenomenon is occurred. Only one relevant thimble remained.

explicit expressions for fermionic determinants in computations. After finding the saddle points we estimate the absolute value of the integrals over thimbles in order to identify their real contribution to the overall sum (4.20). We base on the first approximation for the action in the vicinity of saddle points:

$$S \approx S|_{x_0} + \frac{1}{2}\frac{\partial S}{\partial x^i \partial x^j}\bigg|_{x_0} (x^i - x_0^i)(x^j - x_0^j). \tag{4.31}$$

Thus the integral over thimble can be estimated as the Gaussian one and the weight of thimble is defined by $\exp(-W)$, where

$$W = \mathrm{Re}S|_{x_0} + \frac{1}{2}\log\det\left(D\right)_2. \tag{4.32}$$

D_2 is the matrix of the second derivatives of the real part of the action calculated over coordinates within the thimble (denoted as t_i) in the vicinity of saddle point:

$$D_2 = \frac{\partial \mathrm{Re}S}{\partial t^i \partial t^j}\bigg|_{t=t(x_0)}. \tag{4.33}$$

For real saddles it coincides with the matrix of the second derivatives of the action within $\mathbb{R}^N$. For complex saddles we calculate the $2N \times 2N$ matrix $\mathcal{D}_2$ of the second derivatives of ReS over real and imaginary parts of complex variable x and compute the $\log\det(D)_2$ as the sum of logarithms of positive eigenvalues of this matrix.

4.3.1 Gaussian HS transformation with only complex exponents

Following [117], we start from the one-site Hubbard model because it allows to illustrate some basic concepts by plotting thimbles and anti-thimbles in simple 2D figures. According to definitions in Section (4.2), the action in the path integral representation for the partition function (4.14) of this model can be written as:

$$S(x) = \frac{x^2}{2\beta U} - \ln\left((1 + e^{ix-\beta\mu})(1 + e^{-ix+\beta\mu})\right). \tag{4.34}$$

We used $\alpha = 0$ thus only complex exponents are left in the action. The model is exactly solvable: at low temperatures ($\beta U \gg 1$) there is sharp transition in the number of particles $\langle\hat{n}\rangle = \langle\hat{a}^\dagger\hat{a}\rangle$ when the absolute value of chemical potential becomes comparable to the interaction strength U. The number of particles as a function of chemical potential is plotted in the figure 4.2.

Saddle points, thimbles and anti-thimbles for this model are shown in the figure 4.3 for four different situations. The first case (fig. 4.3a) corresponds to half-filling ($\mu = 0$); the second case (fig. 4.3b) corresponds to intermediate chemical potential ($\mu = U/3$) and the last two plots (fig. 4.3c and 4.3d) correspond to the case of large chemical potential ($\mu \geqslant U$) which is comparable to the interaction strength and causes the transition in the average number of particles $\langle\hat{n}\rangle$. These figures illustrate the key properties of thimbles and anti-thimbles which are important for further consideration. Both thimbles and anti-thimbles start from saddle points. Since the real part of the action monotonically increases along thimbles, they can end up either at infinity or at the points where the fermionic determinant is equal to zero, because Re S tends to infinity in both cases. Anti-thimbles should end up in the region where Re S monotonically decreases. In this model it corresponds to some direction at infinity. We will show further that there are also other possibilities.

At small and intermediate chemical potential ($\mu < U$) there is an infinite number of anti-thimbles crossing the real axis. Thus, there are an infinitely large amount of relevant saddle points which should be included into the sum (4.20). The relative importance of the different terms in the sum (4.20) was estimated for this model in [117] within the saddle points approximation, where the whole integral over the thimble is substituted by the value of the exponent at the corresponding saddle point $e^{-S(z_\sigma)}$. The zeroth saddle at $x = 0$ is of course dominant but one should take into account ≈ 5 thimbles

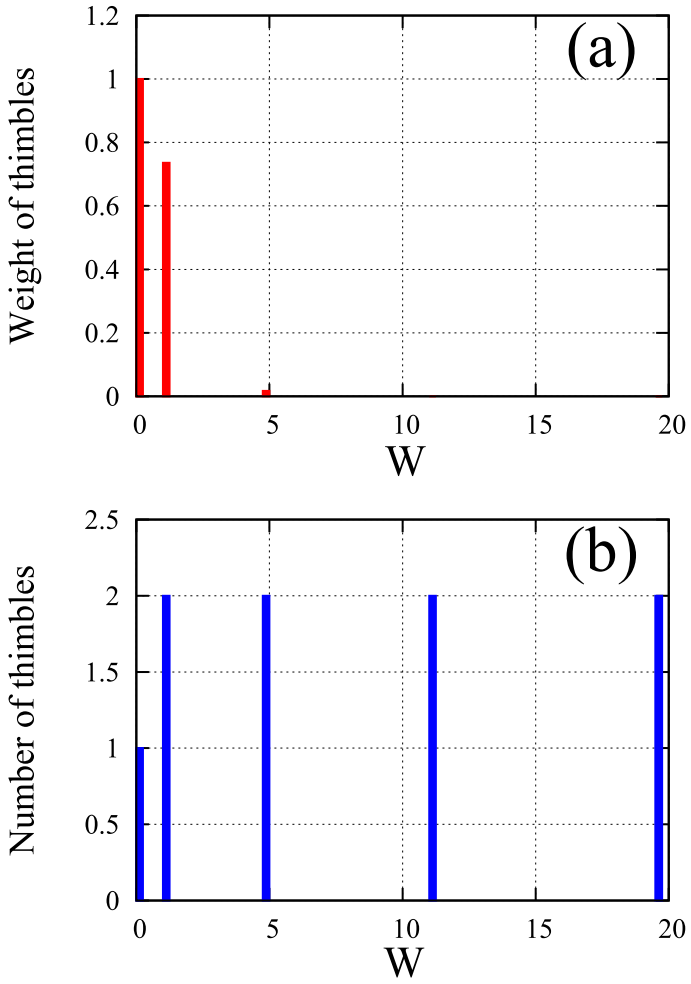

Figure 4.4: Weighted (a) and normal (b) histogram showing the relative importance of relevant saddles for the one-site Hubbard model in the Gaussian representation at half-filling ($\mu = 0$). The action is written in (4.34), $U\beta = 15.0$. Weight of thimbles is counted with respect to the vacuum one.

to reach reasonable precision at intermediate chemical potential around the transition point. This hierarchy is illustrated in the figure 4.4 using the approximations described in eq. (4.31-4.33). This is the typical plot which we will use for the estimation of the relative importance of thimbles in various situations. The lower plot is the histogram showing the number of thimbles which have their values of weight W_σ (see eq. (4.32)) within the given interval with respect to the thimble with the largest weight W_0. The upper plot is the "weighted" histogram. It means that the height of each bar increases by the relative weight $\exp\left(-(W_\sigma - W_0)\right)$ of the thimble with respect to the vacuum one if W_σ of the thimble belongs to the given interval. The weighted histogram (fig. 4.4a) clearly shows that the "vacuum" saddle at zero x still dominates. The weight of all further thimbles (there are two of them contributing to each bar, these thimbles are symmetrical with respect to $x = 0$) rapidly decreases with increased distance from the vacuum $x = 0$.

The main question is how this situation scales when the overall lattice size $N = N_s N_t$ increases. A full derivation of the exact scaling law for the number of relevant thimbles is

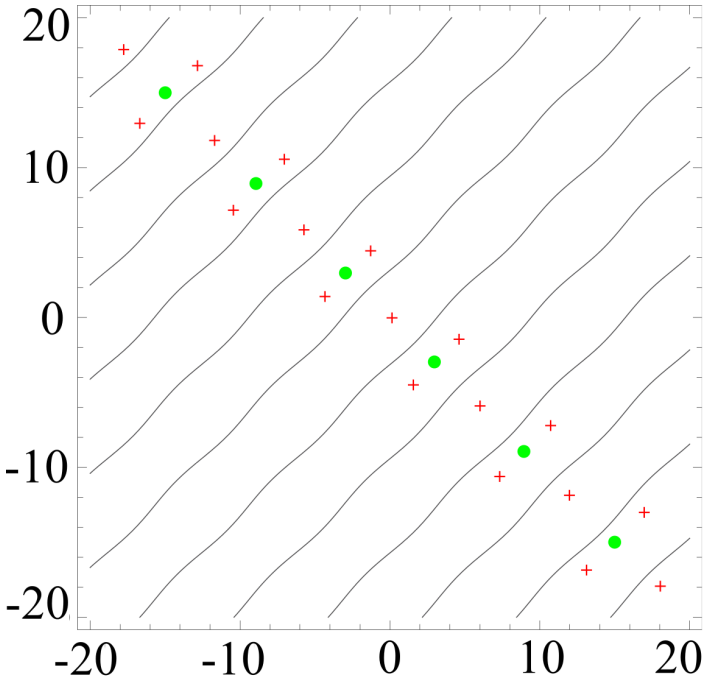

Figure 4.5: Position of the real saddles at half-filling for the two-site Hubbard model with one time slice in the Gaussian representation with only complex exponents. Relevant (positive) saddles are marked with red crosses and irrelevant (negative) saddles are marked by green circles. The lines represent the configurations of the fields ϕ_i where fermionic determinant is equal to zero. The action is written according to eq. (4.14), (4.15), (4.17) with parameters: $U\beta = 15.0$, $\kappa\beta = 3.0$, $\alpha = 1$.

probably unfeasible in the general case. Thus, our task is to find, empirically, whether the number of important saddles increases with increasing lattice size. We will study the region $\mu < U$, since the chemical potential is usually smaller than the typical scale of the on-site interaction in reality. For instance, in graphene, new physical phenomena emerge if the chemical potential crosses the van Hove singularity [136] which is of the order of the hopping (2.7 eV), while on-site interaction is of the order of 10 eV [137]. We will consider the two-site Hubbard model on the lattice with $N_t = 1, 2, 3$ and the four-site Hubbard model with $N_t = 1$. Action is constructed according to (4.14) and (4.15) with the single-particle Hamiltonian defined in (4.17) and (4.18) and $\alpha = 1$. The general form of the action in these cases can be written as

$$S(\phi) = \sum_i \frac{\phi_i^2}{2\delta U} - \ln\left(\det\left(M\right)_{el.}\left(\phi\right)\det\left(M\right)_{h.}\left(\phi\right)\right), \tag{4.35}$$

where $\delta = \beta/N_t$. At half-filling all relevant saddles are obviously located within the real subspace $\mathbb{R}^N$ and the same is true for all relevant thimbles. It means that the tangent subspace for the anti-thimbles is oriented perpendicular to $\mathbb{R}^N$ in the vicinity of these relevant saddles. It also means that once we introduce nonzero μ and the former real saddles shift from $\mathbb{R}^N$ into complex space, their intersection number still remains equal to 1 if the shift is not that large. Moreover, we can expect that additional complex saddles

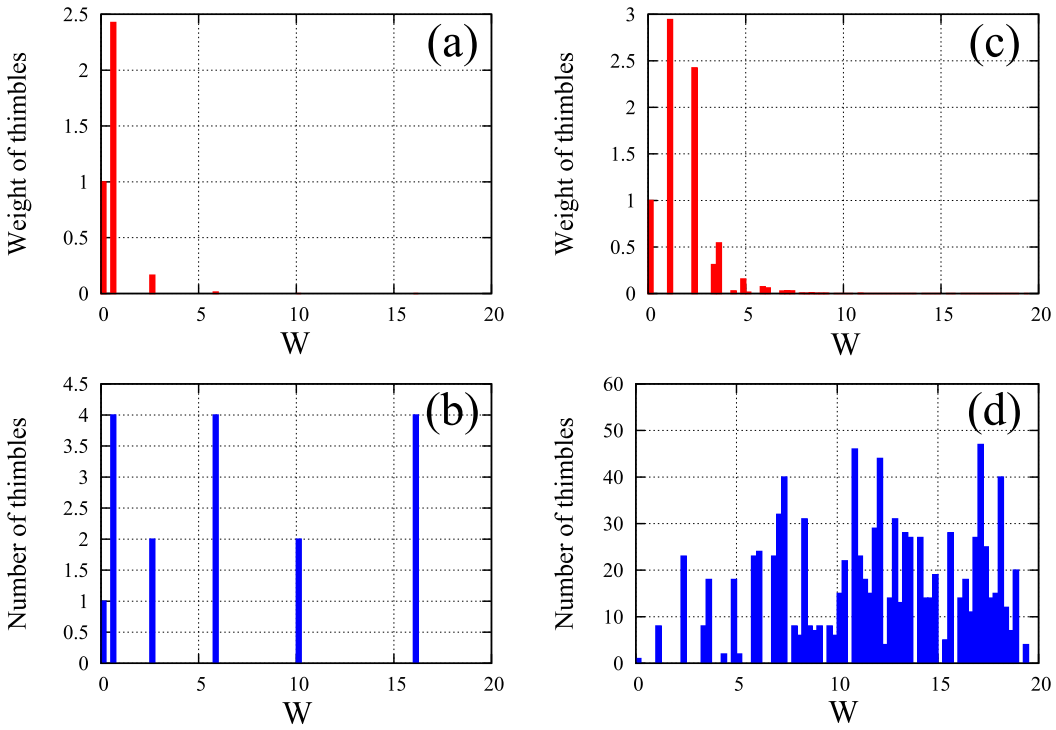

Figure 4.6: Weighted and normal histogram for relevant thimbles at half-filling for two-site lattice ((a) and (b)) and for four-site lattice ((c) and (d)). Gaussian representation with complex exponents is used, $N_t = 1$ in both cases. The action is written according to equations (4.14), (4.15), (4.17) with parameters: $U\beta = 15.0$, $\kappa\beta = 3.0$, $\alpha = 1$. Weight of thimbles is shown with respect to the vacuum one.

(which in principle might become relevant) do not play important role in the overall sum (4.20) for small chemical potential, especially if we do not pass trough a phase transition. Within all these approximations, we can estimate the complexity of the sign problem at relatively small chemical potential by looking at the distribution of real saddles at half filling and then tracing the shift of former real saddles to the complex plane at finite μ.

The figure 4.5 illustrates the position of real saddle points and configurations with zero fermionic determinant in the two-site Hubbard model with $N_t = 1$ and $\alpha = 1$ at half-filling for $U\beta = 15.0$ and $\kappa\beta = 3.0$. Now, two types of saddle points appear at half filling within the real subspace. The classification is made using the matrix of the second derivatives D_2 calculated entirely within the real subspace. "Positive" and "negative" saddles have positive- and negative-defined matrix D_2 respectively. Only positive saddles are relevant, because the thimbles corresponding to the saddle points with negative-defined matrix D_2 cross the real subspace only at a set of points with dimension less then N.

This feature can be easily understood in the model with the double-well potential $(\phi^2 - m^2)^2$. There are two stable minima at $\phi = \pm m$. These points correspond to relevant saddle points, while unstable equilibrium at $\phi = 0$ corresponds to an irrelevant saddle point. Nevertheless, it plays important role in the geometry of thimbles: this point

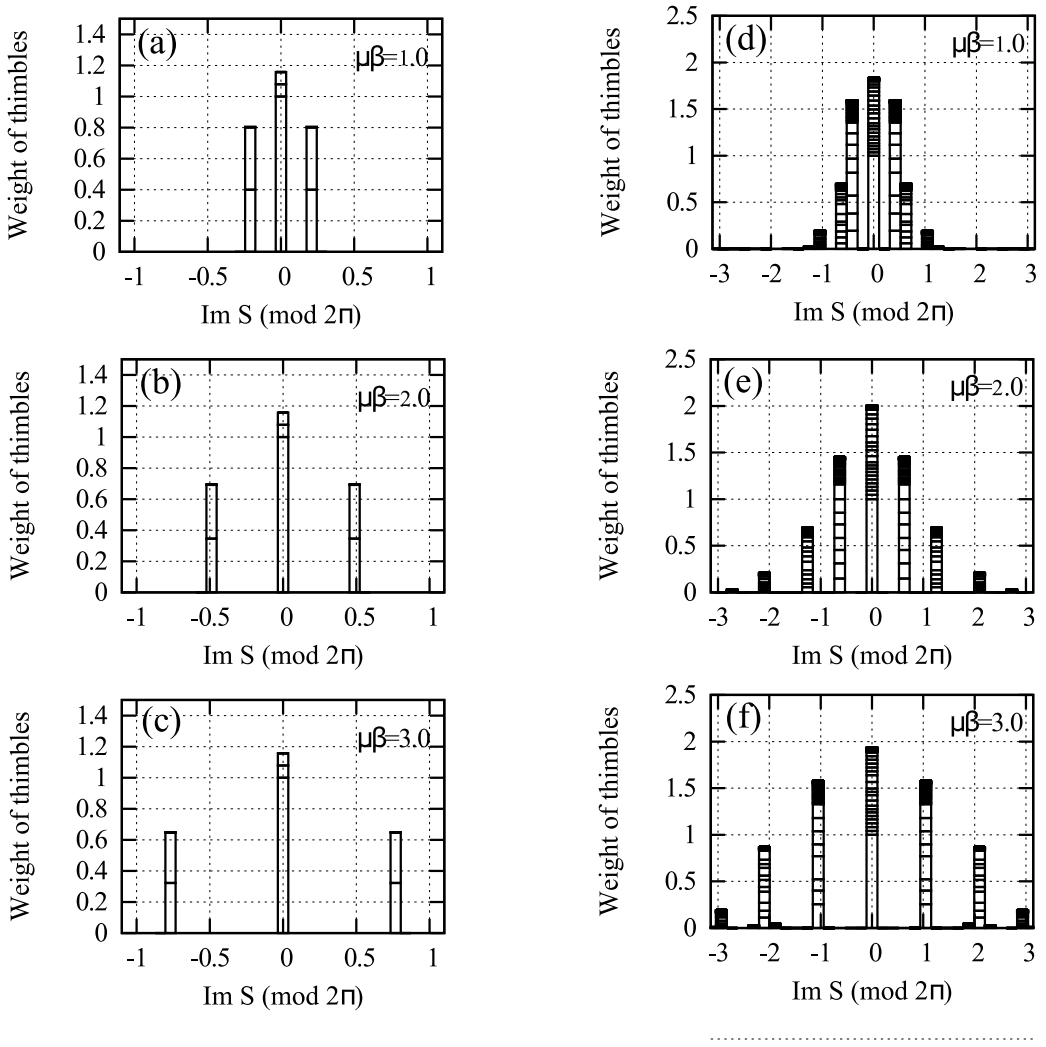

Figure 4.7: Stacked histograms showing the evolution of real saddles which were relevant at half-filling when we increase the chemical potential. In general, they acquire growing complex phases. Each bar shows the weights of several thimbles whose Im S lie within the given interval. Contributions of these thimbles are separated by horizontal lines within the bars. The weight of former "vacuum" saddle is taken as unity. The calculation is made for two-site lattice ((a), (b) and (c)) and four-site lattice ((d), (e) and (f)). $N_t = 1$ in both cases. The action is written according to equations (4.14), (4.15), (4.17),(4.18) with parameters: $U\beta = 15.0$, $\kappa\beta = 3.0$, $\alpha = 1$, $\mu\beta = 1.0,\ 2.0,\ 3.0$.

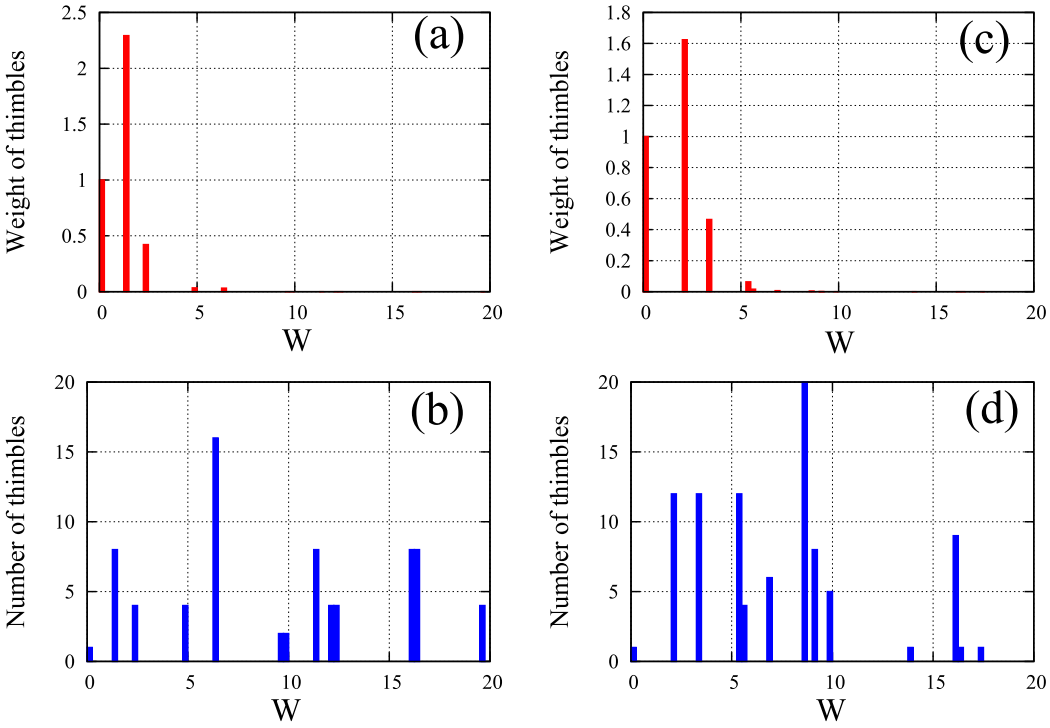

Figure 4.8: Weighted and normal histograms for relevant thimbles at half-filling for two-site lattice with two ((a) and (b)) and three ((c) and (d)) Euclidean time slices. Gaussian representation with only complex exponents is used, the action is written according to equations (4.14), (4.15), (4.17) with parameters: $U\beta = 15.0$, $\kappa\beta = 3.0$, $\alpha = 1$. Weight of thimbles is shown with respect to the vacuum one.

separates two thimbles which start from two stable minima, while its own thimble is perpendicular to the real axis. This property can be generalized to the N-dimensional case. If some saddle has its matrix $\mathcal{D}_2$ with $M \leq N$ negative eigenvalues, this saddle is irrelevant. But it still has $N - M$ positive eigenvalues. It means that the intersection of the thimble emanating from this saddle with real subspace $\mathbb{R}^N$ has dimension $N - M$. This set of points forms a domain wall between two thimbles within the real subspace if $M = 1$ or just the manifold of sunk points for relevant thimbles if $M > 1$.

To sum it all up, only "positive" real saddles are relevant when we are looking at a system at half filling. According to the figure 4.5, there is again an infinite set of relevant saddle points. The thimbles are separated by both the domain walls formed by configurations with zero fermionic determinant and by the lines originating from the "negative" (irrelevant) real saddles. Unlike the domain walls, these lines are penetrable for the HMC updates. In general, the appearance of the infinite number of relevant thimbles is the consequence of the periodicity of the fermionic determinant (4.15) as a function of auxiliary fields in $\mathbb{R}^N$.

The figure 4.6 shows the weight of thimbles at half filling for two-site and four-site lattice with $N_t = 1$. A comparison with the same plots for the one-site model 4.4 shows that the situation rapidly becomes worse. The "vacuum" saddle at $\phi_1 = \phi_2 = 0$ is no more

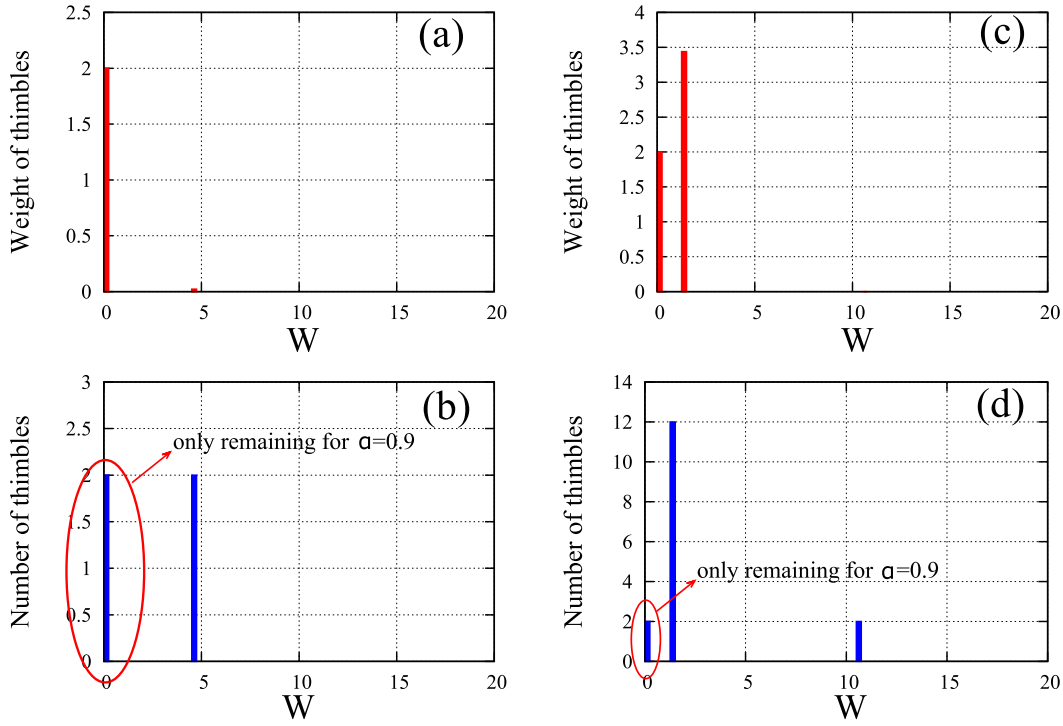

Figure 4.9: Weighted and normal histograms for relevant thimbles at half-filling for two-site ((a) and (b)) and four-site ((c) and (d)) lattice. Gaussian representation with only real exponents is used, $N_t = 1$ in all cases. The action is written according to equations (4.14), (4.15), (4.17) and (4.18) with parameters: $U\beta = 15.0$, $\kappa\beta = 3.0$, $\alpha = 0$. Weight of thimbles is shown with respect to the vacuum one. We also mark the thimbles, which remain relevant if the mixed representation is used with $\alpha = 0.9$.

dominant. Instead of it the spatially nonuniform saddles play the main role in the sum and their number increases non-linearly with increasing N_s. For example, the number of thimbles needed to be taken into account for four-site lattice already approaches 100.

Once we go away from half-filling, former real saddles move to the complex plane and acquire complex phases. This process is illustrated in the figure 4.7 for lattices with $N_S = 2, 4$ and $N_t = 1$. These stacked histograms show the distribution of the imaginary part of the action for former real saddles which presumable remain relevant for relatively small chemical potential. The delimiters inside each bar mark the share of one thimble within the bar. One can clearly see how the complexity of the sign problem increases with increased number of thimbles: the distribution of ImS becomes much broader and denser for the four-site model. It is directly connected with the appearance of new types of non-uniform saddles which are not equivalent to each other due to translational or rotational symmetry (equivalent saddles have the same ImS). Once the lattice size is increased these saddles fill the unit circle in complex plane more and more densely thus increasing the sign problem.

The cases of the two-site model with $N_t = 2$ and $N_t = 3$ are shown in the figure 4.8. The number of non-uniform saddles increases again, but in the continuous limit

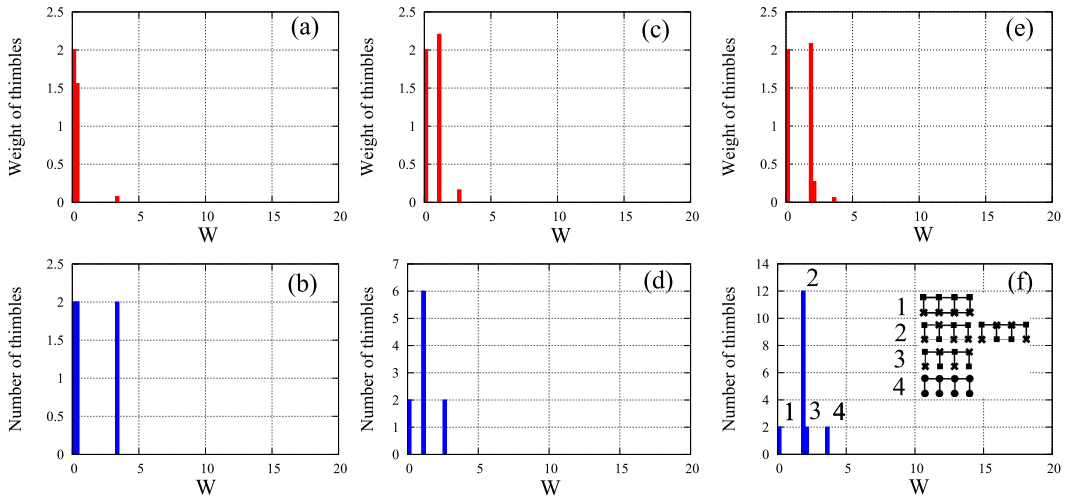

Figure 4.10: Weighted and normal histograms for relevant thimbles at half-filling for two-site lattice with two ((a) and (b)), three ((c) and (d)), and four ((e) and (f)) Euclidean time slices. Gaussian representation with only real exponents is used, the action is written according to equations (4.14), (4.15), (4.17) with parameters: $U\beta = 15.0$, $\kappa\beta = 3.0$, $\alpha = 0$. Weight of thimbles is shown with respect to the vacuum one. Inset in the figure (f) shows schematic pictures of relevant saddle points corresponding to each of the four bars in the histogram.

the situation might actually become much better. The reason is that almost all of these non-vacuum saddle points are lying already behind the "domain wall": the situation from the figure 4.5 is reproduced also for larger lattices. Thus these thimbles appear in the sum only due to the presence of the "domain walls". If N_t is increased, the coefficient before the squared fields in the action increases (see eq. (4.14)) thus the configurations with large values of the fields $\phi_{x,t}$ are suppressed. On the other hand, the overall scale for the distance between "domain walls" is fixed by the period 2π of the fermionic determinant and this period is independent on N_t. Thus the configurations behind the domain wall with $\phi_{x,t} > \pi$ are effectively suppressed and we a left with very limited number of thimbles which are really important. This phenomena can be already seen in the figures 4.8a and 4.8c), where the weight of the second bar (the lowest "non-vacuum" thimbles) decreases which increased N_t.

4.3.2 Gaussian HS transformation with only real exponents

Now we check the same lattices using HS transformation with only real exponents. Action is again constructed according to (4.14) and (4.15) but parameter α is equal to zero, thus only fields $\chi_{x,t}$ remain in the integral. The figure 4.9 shows the weight of relevant thimbles at half filling for two- and four-site lattices with $N_t = 1$. The situation is much better in comparison with the analogous distributions for the action with complex exponents (fig. 4.6). The fermionic determinant is no more periodical function of the fields in $\mathbb{R}^N$, thus there is always finite number of relevant thimbles.

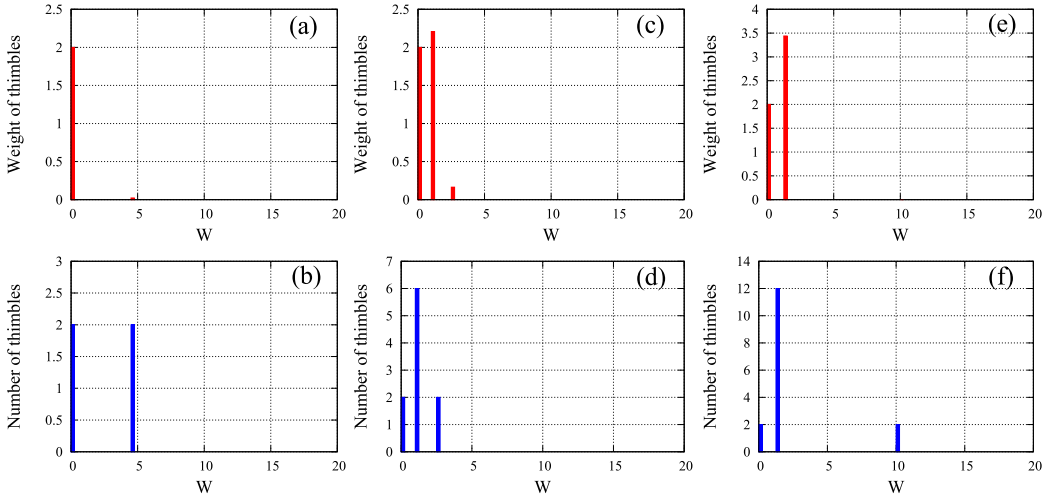

Figure 4.11: Weighted and normal histograms for relevant thimbles at finite chemical potential $\mu\beta = 3$ for two-site lattice with $N_t = 1$ (a, b) and $N_t = 2$ (c, d), and for four-site lattice with $N_t = 1$ (e, f) . Gaussian representation with purely real exponents is used, the action is written according to equations (4.14), (4.15), (4.17) and (4.18) with parameters: $U\beta = 15.0$, $\kappa\beta = 3.0$, $\alpha = 0$. Weight of thimbles is shown with respect to the vacuum one.

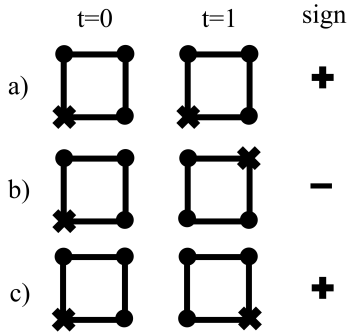

Figure 4.12: Examples of configurations on the lattice with $N_s = 4$, $N_t = 2$, with only real exponents in the action. The scheme shows three configurations, two of them have positive weight ((a) and (c)) and one has negative weight (b). Both time slices are shown in each case. Circles correspond to the Hubbard field $\chi \approx -U\delta$ and crosses correspond to $\chi \approx U\delta$, $\delta = \beta/2$.

However, the situation with the number of dominant thimbles is still rather complicated. The two thimbles with the lowest weight correspond to the saddle points where the Hubbard fields $\chi_{x,t}$ have opposite values at two sublattices but are uniform within each sublattice. The two saddles with the smallest weight (the last bar in the figures 4.9b and 4.9d) correspond to uniform field configurations. And finally, the large number of saddle points with highly non-uniform Hubbard field configurations appear with increased N_s and N_t (see the bar in the middle in the figures 4.9 and 4.10). These non-uniform saddles dominate in the sum over thimbles for all lattices studied in this work except of the smallest one with $N_s = 2$ and $N_t = 1$. More detailed analysis of the continuous limit is presented in the figure 4.10 for the lattice with $N_s = 2$ and $N_t = 2, 3, 4$. Different types of saddle points are described symbolically in the inset in the figure 4.9f: we always have two lowest saddles with Hubbard fields uniform within sublattices and two highest saddles with Hubbard fields uniform in entire lattice. In between of them we have a set of saddles where Hubbard fields fluctuate between sublattices. Their weight is very close to each other, only small splitting appears for $N_t = 4$. Thus their overall number can be estimated as $2^{N_t} - 2$, taking into account all possible reflections and translations. The competition arises between exponentially increased amount of these thimbles and their exponentially decreasing weight (this fact can be also noticed from the figure 4.9). It means that in continuous limit $N_t \to \infty$ these non-uniform saddles can still make significant contribution in the sum (4.20).

The case with non-zero chemical potential is shown in the figure 4.11. Unlike the previous study for complex exponents, where we could not directly find relevant complex saddles thus we just tracked the evolution of former real saddles, here we can find all relevant saddles exactly, because all of them are lying within $\mathbb{R}^N$ even for $\mu \neq 0$. The figure 4.11 shows the situation for $\mu\beta = 3$. It shows three different cases: 1) $N_s = 2$, $N_t = 1$; 2) $N_s = 2$, $N_t = 2$; 3) $N_s = 4$, $N_t = 1$. Thus we can trace both trends: increasing N_t and increasing N_s. Comparison with the figures 4.9 and 4.10 shows that there are only small changes in the distribution of relevant thimbles.

Importantly, all relevant saddles still have positive weight. This is not surprising taking into account that the absence of the sign problem for the two-site model with Hamiltonian (4.17) can be proven analytically even in the continuous limit $N_t \to \infty$. It means that the sign problem for the path integral representation with purely real exponents appears only if we increase N_t and N_s further. In order to give a short overview how the sign problem looks like in this case, we studied the lattice with $N_s = 4$ and $N_t = 2$. Indeed, the saddle points with negative sign appear in this case. There is, of course, very large amount of various non-uniform saddles on this lattice, so we just give some examples. The two saddle points with auxiliary fields being uniform across sublattices are again the lowest ones and they still have positive weight. However, the non-uniform saddles with smaller weight can change the sign. Typically, those saddle points which

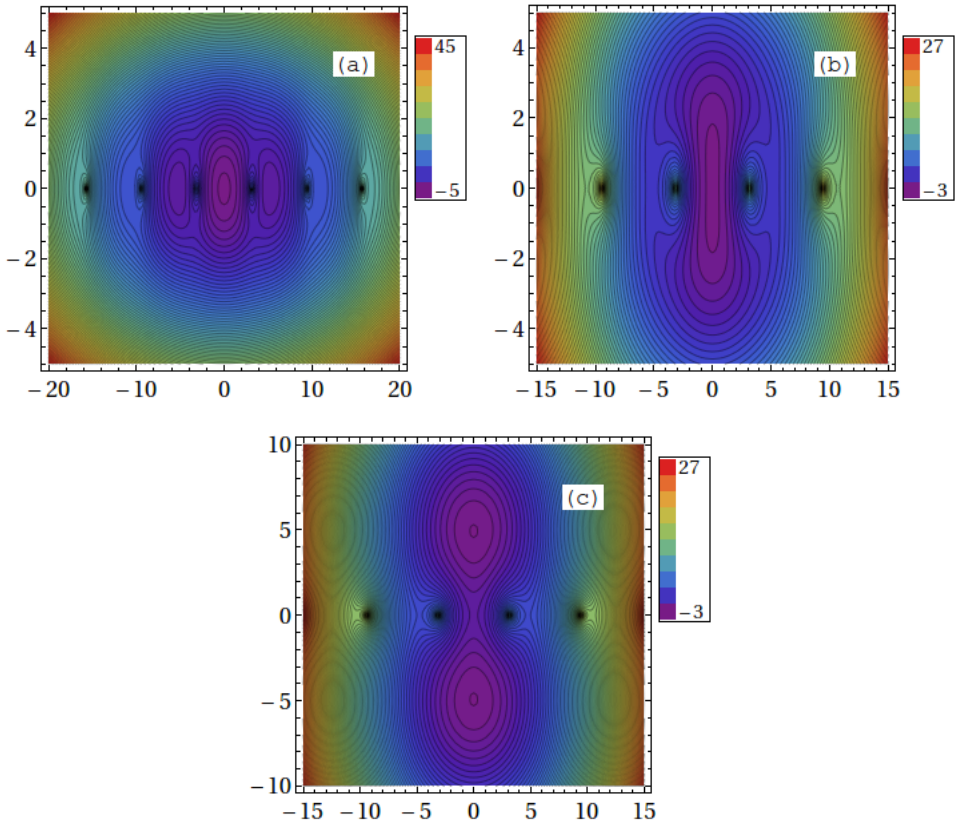

Figure 4.13: The action for the one-site Hubbard model in the Gaussian representation: (a) $\alpha = 0.95$, (b) $\alpha = 0.8$, (c) $\alpha = 0.5$. $U\beta = 10.0$, the action is written according to (4.14), (4.16). Horizontal axis corresponds to the field ϕ and vertical axis corresponds to the field χ. Relevant saddle points looks like local minima on the current plots which show only the behaviour of action within $\mathbb{R}^N$. All "negative" directions for those saddle points are pointing out in complex space.

are non-uniform only in space but uniform in the Euclidean time direction have positive weight. On the other hand, the saddle points, which are non-uniform both in space and time, can have both positive and negative weight and the cancellation appears between them. Example configurations for the saddle points with positive and negative weight are shown in the figure 4.12. The observation that the field configurations, which are highly non-uniform in Euclidean time, are responsible for the sign problem is in line with early observations made for BSS-QMC [138].

In general, the sign problem in the limit $\alpha = 0$ is much milder in comparison with the $\alpha = 1$ case. This is true at least for small lattice studied so far. The reason is the finite number of relevant thimbles for $\alpha = 0$ and much smaller fluctuations of the phase factors for these thimbles.

4.3.3 Gaussian HS transformation in mixed regime

Now we explore the "mixed" regime where $\alpha \in (0, 1)$ and both real and complex exponents appear in the action (4.16). At the moment we know that the sign problem is milder in the $\alpha = 0$ case, but we will explicitly demonstrate below that the number of relevant thimbles can be reduced even further by tuning the parameter α. Additional argument in favor of the mixed regime is the appearance of "domain walls" in both limits. Thus neither $\alpha = 1$ nor $\alpha = 0$ is entirely suitable for the simulations even at half filling.

We start from the simplest example of the one-site Hubbard model. Figure 4.13 shows the action (including logarithms of fermionic determinants) constructed according to eq. (4.14),(4.15),(4.16) for one-site model. It is plotted as a function of two fields ϕ and χ for different values of α. In the limit when α approaches 1 we have infinite number of relevant saddle points located along the ϕ-axis and separated by the barriers around the points where the determinant is equal to zero. The vacuum thimble is dominant but the others still have significant weight. Once α decreases, the non-vacuum saddles emerged due to the periodicity of the fermionic determinant as a function of ϕ start to disappear. If $\alpha < 0.86$ we arrive at the intermediate regime where only vacuum saddle point is relevant. The two saddles along the χ axis appear only if $\alpha < 0.84$. If α decreases further, these saddle points become more and more disconnected. Thus we have the situation when the length of the HMC trajectory should become longer and longer in order to ensure the possibility to visit both saddle points which are equally important in the probability distribution. This situation is again very disadvantageous for QMC calculations.

Summarizing, in the interval $\alpha \in [0.84, 0.86]$ we have only one relevant thimble at half filling for the one-site Hubbard model. Even more generally, the vicinity of the vacuum configuration $\phi = \chi = 0$ is strongly dominant if α is around this interval because the saddles along the ϕ-axis are lifted or even disappeared and the two saddles along χ-axis (if appeared) are still very close to the vacuum. Important point is that the "sweet spot" regime exists also for larger lattices. For example, at the lattice with $N_s = 2$, $N_t = 1$ all saddles connected with ϕ-periodicity of the fermionic determinant disappear at $\alpha < 0.92$. On the other hand, the sub-dominant thimbles corresponding to the second bar in the histogram for the case with real exponents (see fig. 4.9a and 4.9b) appear only if $\alpha < 0.63$. In between of these two values of α we have the regime with only two relevant saddle points at half filling. These saddles are marked in the figure 4.9b. The situation repeats also at the lattice with $N_s = 4$, $N_t = 1$. Due do increased system size, we didn't scan the whole interval $\alpha \in [0, 1]$, but at least at $\alpha = 0.9$ there are again only two relevant saddles (the first bar in the figure 4.9d) which correspond to auxiliary fields χ being uniform across sublattices, with different signs at different sublattices. Auxiliary fields ϕ are zero at these saddles. In the next section we present also some numerical observations that the regime with reduced number of relevant thimbles exists also in more

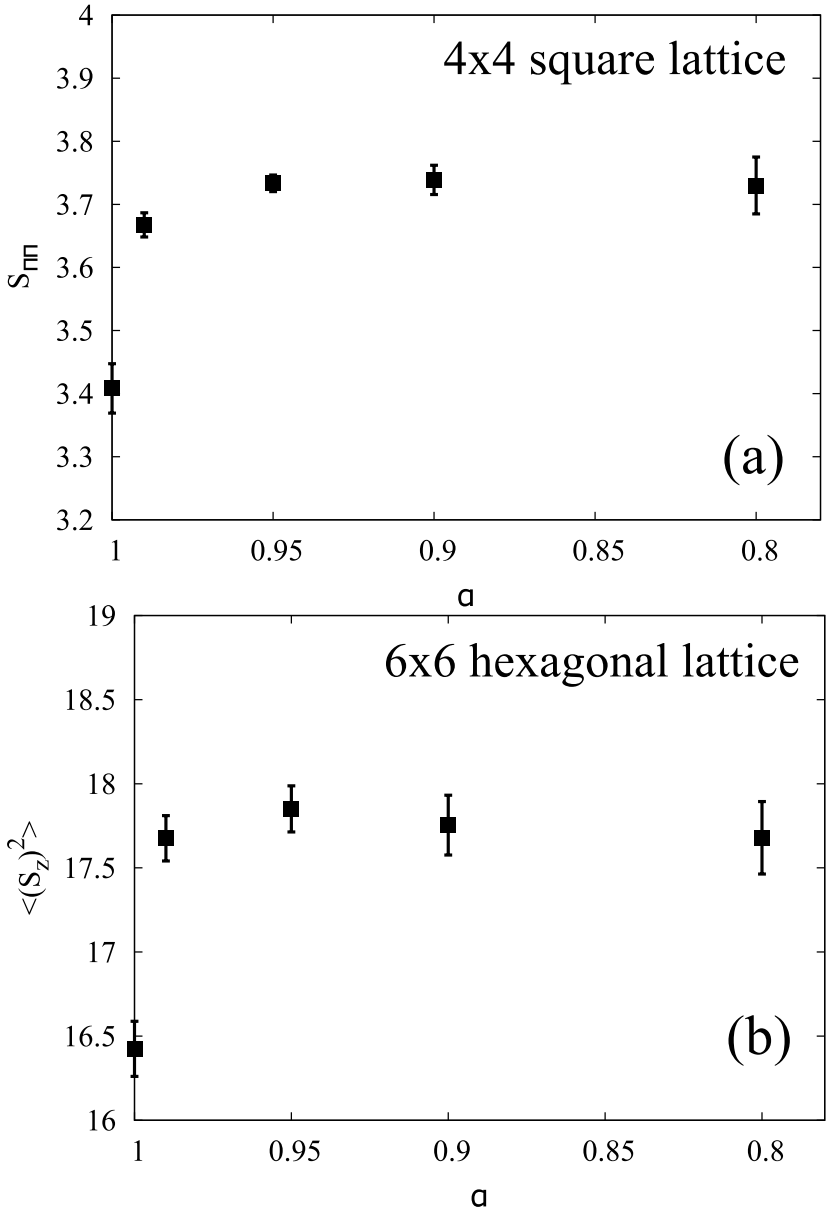

Figure 4.14: (a) The dependence of the spin structure factor $S_{\pi\pi}$ on α for the 4×4 square lattice. The following parameters were used for the simulation: $U = 4\kappa$, $N_t = 320$, $\beta\kappa = 40$. (b) The dependence of the squared spin at one sublattice on α for the 6×6 hexagonal lattice. Parameters of the simulation: $U = 3.8\kappa$, $N_t = 128$, $\beta\kappa = 20$.

realistic situations with large N_t.

4.4 Results from test HMC simulations

In order to expand the results from the previous section to more practical cases, we performed some simulations using HMC at different values of α. Two settings were used: 1) square 4×4 lattice with $N_t = 320$ time slices in Euclidean time, on-site interaction $U = 4\kappa$, and inverse temperature $\beta\kappa = 40$; 2) 6×6 lattice with $N_t = 128$ time slices, on-site interaction $U = 3.8\kappa$, and inverse temperature $\beta\kappa = 20$. In the case of the square

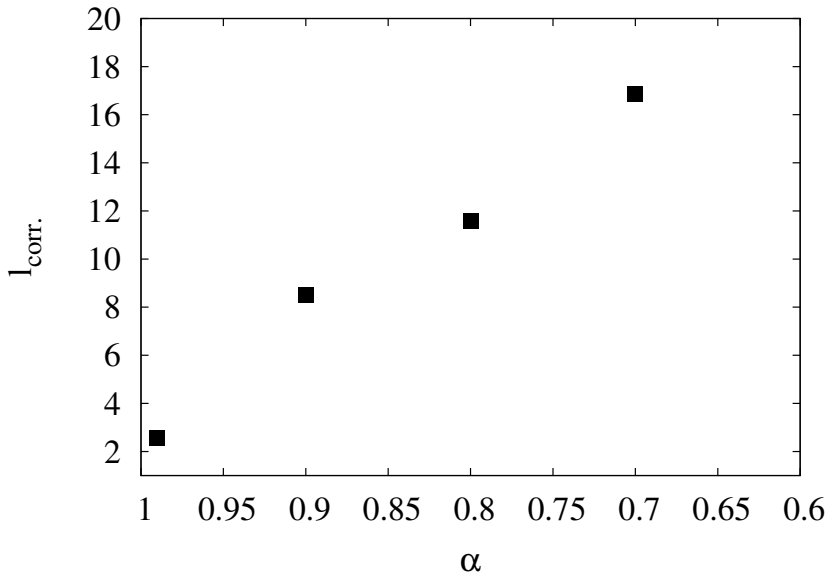

Figure 4.15: Correlation length characterizing the autocorrelation between configurations in the HMC process. The runs for different α are equivalent in a sense that the trajectory length in Hamiltonian updates is fixed. One can see that the autocorrelation grows signalling about the problems with ergodicity for smaller values of α. Results are shown for 6×6 hexagonal lattice, with the following parameters: $U = 3.8\kappa$, $N_t = 128$, $\beta\kappa = 20$.

lattice we calculate the spin structure factor

$$S_{\pi,\pi} = \frac{4}{N}\sum_{i,j} e^{i\mathbf{Q}(\mathbf{R}_i-\mathbf{R}_j)}\langle \hat{S}_z^i \hat{S}_z^j\rangle, \tag{4.36}$$

where $\mathbf{Q} = (\pi,\pi)$, $\mathbf{R}_i$ is the coordinate of the i-th site of the lattice. The squared spin per sublattice is calculated for the hexagonal lattice:

$$\langle (S_z)^2\rangle = \langle \left(\sum_{i\in 1st.sublat.} \hat{S}_z^i\right)^2 \rangle. \tag{4.37}$$

Results are presented in the figure 4.14. The effect of the elimination of "domain walls" existing in the limit $\alpha = 1$ is clearly seen, since the calculations made at $\alpha = 0$ show noticeably different results. However, the overall role of the thimbles behind the "domain walls" is rather small and doesn't exceed 10 %. The comparison with the figure 4.6 indeed supports the previous claim that the weight of all additional saddles appearing due to the periodicity of the fermionic determinant as a function of fields ϕ decreases in continuous limit. Even quite small value of $\alpha \sim 0.05$ is already enough to eliminate the problems with ergodicity.

Figure 4.15 shows the dependence of the autocorrelation between configurations of auxiliary fields on the parameter α. Since all parameters of HMC process including the trajectory length are fixed, increased correlation length means that configurations tend to stuck within some regions of the phase space when α decreases. It directly

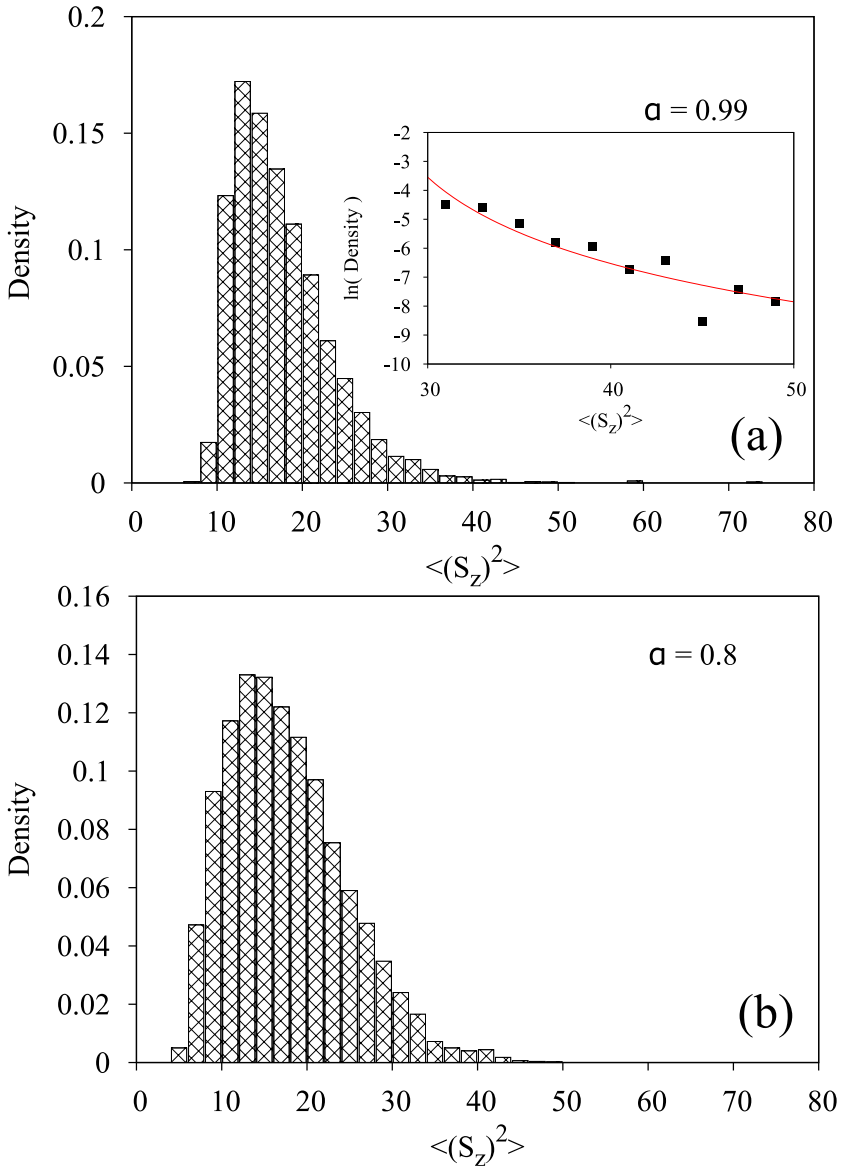

Figure 4.16: Histograms showing the distribution of the observable (squared spin on sublattice) in different Monte Carlo field configurations. Results are presented for 6×6 hexagonal lattice, with the following parameters: $U = 3.8\kappa$, $N_t = 128$, $\beta\kappa = 20$, $\alpha = 0.99$ and 0.8. The inset in the figure (a) shows the logarithm of the distribution fitted with the function $\ln A/(x - B)^{2.5}$.

corresponds to the phenomena we observed in the previous section for one-site and few-site models (see e g. figure 4.13c), where the relevant saddle points tend to form more and more separated peaks in the probability distribution with decreasing α. Combining this observation with the results for observables (figure 4.14) we can conclude that the "sweet spot" regime exists also in these more realistic calculations at approximately the same values of $\alpha \approx 0.9$. In this regime we already get rid of the "domain walls" but the probability distribution for the fields ϕ and χ is not yet separated into distinct peaks.

Unfortunately, the existence of the field configurations with zero fermionic determinant still introduces important obstacles in QMC algorithms for continuous auxiliary

fields even if the problems with ergodicity are absent. Namely, the distributions of observables become heavy tailed with indefinite second moment. Thus the standard statistical post-processing based on the central limit theorem may not be applicable. Let us consider the complementary cumulative distribution function for the spin structure factors Σ. Among other terms, they always include squared Euclidean fermionic propagator g^2. This is the most important term in the vicinity of the configurations where the fermionic determinant is zero, since the propagator diverges there as $1/\Delta$. Δ is the distance to the zero point of the determinant in the space of auxiliary fields ϕ and χ. Due the divergence of observables near the zero points of the determinant, exactly these field configurations define the complementary cumulative distribution function $\bar{F}_\Sigma(S)$ at large values of observable. If $\alpha = 1$ (only ϕ fields appear in the integrals) the asymptotic behaviour of the function $\bar{F}$ can be described by the integral:

$$\bar{F}_\Sigma(S)|_{S\to\infty} = \mathcal{P}(\Sigma > S) = \int_{V:\Sigma>S} d^N\phi P(\phi), \tag{4.38}$$

where $P(\phi)$ is the probability distribution for the ϕ fields. If S is sufficiently large, the volume V is just some thin layer in the vicinity of the "domain wall", where $P(\phi) = 0$. Now we change the variables so that $x_2...x_N$ correspond to the shift parallel to the "domain wall" while the coordinate x_1 is perpendicular to it. The "domain wall" itself corresponds to $x_1 = 0$. Thus

$$\bar{F}_\Sigma(S)|_{S\to\infty} = \int_{V:\Sigma>S} d^N x \frac{\mathcal{D}(\phi)}{\mathcal{D}(x)} x_1^2 f(x_2...x_N), \tag{4.39}$$

and we used eq. (4.29) in order to estimate the probability distribution $P(x)$ in the vicinity of "domain walls" as $P(x) \approx x_1^2 f(x_2...x_N)$. Since the observable diverges as we approach the "domain wall":

$$\Sigma \approx \frac{C(x_2, ...x_N)}{x_1^2}, \tag{4.40}$$

the integral over x_1 in (4.39) has the limits

$$x_1 \in [-C_1(x_2, ...x_N)/\sqrt{S}, C_2(x_2, ...x_N)/\sqrt{S}], \tag{4.41}$$

where $C_1, C_2 > 0$. If the Jacobian doesn't have any divergences in the limit $x_1 \to 0$, the integral over x_1 in (4.39) can be computed separately. Thus the asymptotic behaviour of the function $\bar{F}$ is described by the expression:

$$\bar{F}_\Sigma(S)|_{S\to\infty} \approx \frac{\mathcal{C}}{S^{3/2}}, \tag{4.42}$$

$$\mathcal{C} = \frac{1}{3}\int dx_2...dx_N \left.\frac{\mathcal{D}(\phi)}{\mathcal{D}(x)}\right|_{x_1=0} \times \tag{4.43}$$

$$\times \left(C_1(x_2, ...x_N)^3 + C_2(x_2, ...x_N)^3\right).$$

Conversion to the probability distribution gives

$$P_\Sigma(S)|_{S\to\infty} \sim \frac{1}{S^{5/2}}. \tag{4.44}$$

The same derivation can be repeated in the opposite limit of purely real exponents ($\alpha = 0$). Away of these two limits the derivation has to be modified since the dimensionality of the manifolds with zero determinant is reduced to $N - 2$, where N is the total number of auxiliary fields ϕ and χ. We should now separate two coordinates x_1 and x_2 which corresponds to the shift perpendicular to the "line" with zero fermionic determinant, while all other coordinates $x_3, ..x_N$ again correspond to the shift parallel to this "line". After it x_1 and x_2 are changed to polar coordinates (ρ, φ) and the resulting asymptotic behaviour for the complementary cumulative distribution function is described by the expression

$$\bar{F}_\Sigma(S)|_{S\to\infty} \approx \int d\varphi dx_3 ... dx_N \int_0^{C(\varphi,x_3,..x_N)/\sqrt{S}} \rho^3 d\rho \left.\frac{\mathcal{D}(\phi)}{\mathcal{D}(x)}\right|_{\rho=0} f(\varphi, x_3 ... x_N). \tag{4.45}$$

Additional power of ρ appears from the transfer to polar coordinates. In principle, this power appears from the Jacobian if the transfer to polar coordinate is included in the general change of variables. The probability distribution for the spin structure factors has now the asymptote

$$P_\Sigma(S)|_{S\to\infty} \sim \frac{1}{S^3}. \tag{4.46}$$

Similar derivations can be repeated for lower dimensions of the manifolds with zero fermionic determinant with larger powers of ρ appearing from the Jacobian. Generally, the lower the dimensionality of the manifolds with zero fermionic determinant leads to the larger absolute value of the power in the tail of the distribution.

In order to demonstrate this effect explicitly, we plotted the distributions of the observable (squared spin on sublattice) obtained from the calculations on hexagonal lattice. Results are shown in the figure 4.16. The heavy tailed distribution is clearly seen both for $\alpha = 0.99$ and $\alpha = 0.8$. The inset in the figure 4.16a shows that the tail of the distribution can not be described by the Gaussian function. The quality of data is not good enough to define the power law from the fitting, but the logarithm of the distribution definitely can not be fitted with $-(x - x_0)^2/2\sigma$ with any reasonable dispersion σ.

One can see that in both cases (4.44) and (4.46) the second moment for the observable is not defined. It means that the standard estimation of error based on the calculations of dispersion is not applicable. Correct procedure must include data binning with numerical estimation for the confidence interval on the basis of the final distribution for the averages.

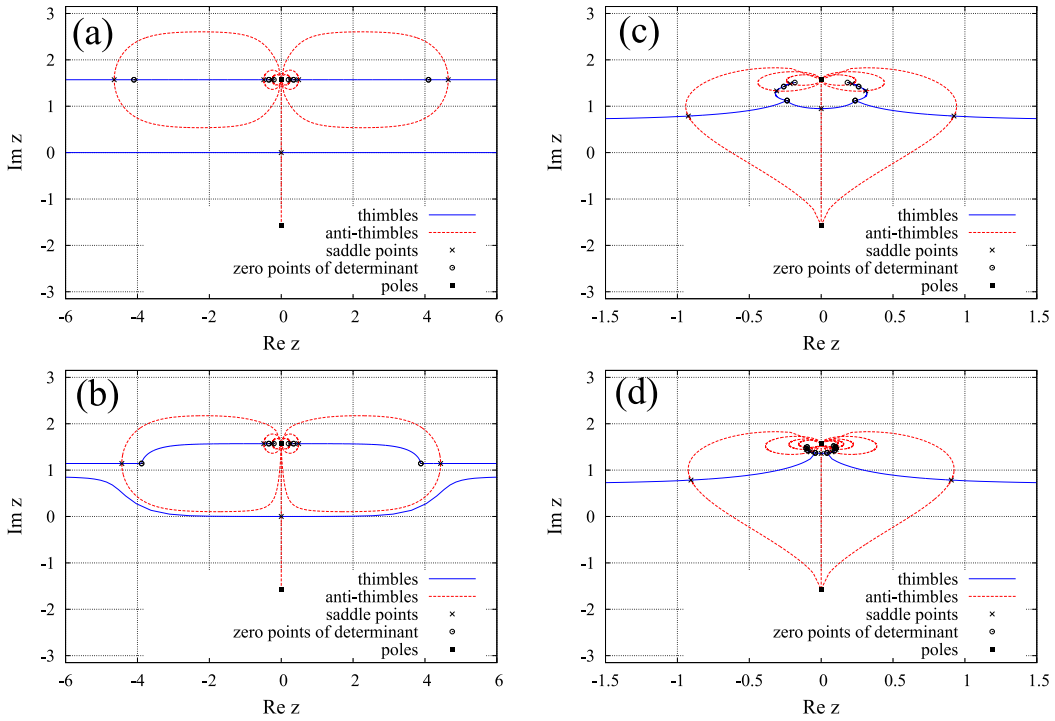

Figure 4.17: Thimbles and anti-thimbles for the one-site Hubbard model in the non-Gaussian representation at various values of chemical potential. The action is written in (4.54). $U\beta = 15.0$. (a) Half filling ($\mu = 0$). Only one thimble covers the whole real axis. (b) Small chemical potential ($\beta\mu = 0.002$). The Stokes phenomenon hasn't yet occurred and we have still only one relevant saddle: the former "vacuum" one but shifted to complex plane. (c) Intermediate values of chemical potential ($\beta\mu = 5.0$). The Stokes phenomenon has already occurred and we have three relevant saddles. However, the statistical weight of former "vacuum" saddle still prevails. (d) Large chemical potential ($\beta\mu = 15.0$). There are still three relevant thimbles, but the statistical weight of former "vacuum" saddle is negligible in comparison with two symmetrical complex saddles. In all cases anti-thimbles corresponding to irrelevant saddles have both their ends in the same pole $\mathrm{Im}\, z = \pi/2$, $\mathrm{Re}\, z = 0$. We show only several saddles close to the point $\mathrm{Im}\, z = \pi/2$, $\mathrm{Re}\, z = 0$, in fact there is infinite number of saddles approaching the pole.

4.5 Non-Gaussian representation for the interaction term

4.5.1 One-site Hubbard model

In this section we derive the non-Gaussian integral representation of the exponents with four-fermionic terms. We choose the integral representation because it preserves the Cauchy's Integral theorem and the possibility to reduce the sign problem by shifting the integration contour to the complex plane. The main motivation is to demonstrate an alternative way to get rid of the infinite number of relevant thimbles appearing in the Gaussian HS transformation with only complex exponents.

We start from the integral representation with overall structure similar to BSS-QMC

(4.5) with the auxiliary fields bounded to some finite region. The interaction term in (4.10) can be written as the series:

$$e^{-\frac{\delta U}{2}(\hat{n}_{el.}-\hat{n}_{h.})^2} = \\ = 1+\sum_{j=1}^{\infty}\frac{(-\delta U/2)^j}{j!}(\hat{n}_{el.}-\hat{n}_{h.})^2 \tag{4.47}$$

On the other hand

$$\frac{1}{2}\int_{-1}^{1} e^{i\gamma x(\hat{n}_{el.}-\hat{n}_{h.})}dx = \\ = 1+(\hat{n}_{el.}-\hat{n}_{h.})^2\int_0^1\left(\sum_{m=0}^{\infty}\frac{(-1)^m(\gamma x)^{2m}}{(2m)!}\right)dx. \tag{4.48}$$

Thus the following integral transformation is possible:

$$e^{-\frac{\delta U}{2}(\hat{n}_{el.}-\hat{n}_{h.})^2} = \frac{1}{2}\int_{-1}^{1} e^{i\gamma x(\hat{n}_{el.}-\hat{n}_{h.})}dx, \tag{4.49}$$

where constant γ is defined as

$$e^{-\frac{\delta U}{2}} = \frac{\sin\gamma}{\gamma}. \tag{4.50}$$

In some cases this equation has several physically equivalent solutions. We always get the smallest possible value of γ. Using this formula, we arrive to the path integral representation of the partition function very similar to (4.11) and (4.12):

$$\mathcal{Z}_n = \int_{-1}^{1}\mathcal{D}\psi_{x,t}\det\left(P\right)_{el.}\left(\psi_{x,t}\right)\det\left(P\right)_{h.}\left(\psi_{x,t}\right) \tag{4.51}$$

with fermionic operators for electron and holes defined as:

$$P_{el.}(\psi_{x,t}) = I+\prod_{t=1}^{N_t}\left(e^{-\delta(h+\mu)}\mathrm{diag}\left(e^{i\gamma\psi_{x,t}}\right)\right), \\ P_{h.}(\psi_{x,t}) = I+\prod_{t=1}^{N_t}\left(e^{-\delta(h-\mu)}\mathrm{diag}\left(e^{-i\gamma\psi_{x,t}}\right)\right). \tag{4.52}$$

As in the previous cases $\left(\mathrm{diag}\left(e^{i\gamma\psi_{x,t}}\right)\right)$ is a $N_s\times N_s$ diagonal matrix, which contains the exponents of auxiliary fields belonging to one time slice.

In principle, one can work directly with this representation for the partition function changing the fields $\psi_{x,t}$ locally or organizing the Hamiltonian updates in the bounded region. However, the organization of dynamics for the field bounded within the interval $\psi_{x,t}\in[-1;\,1]$ needs some modifications of the HMC algorithm. The special "reflection" steps should be made at the border. This can be avoided if we change the variables stretching the integration domain back to infinity:

$$\psi_{x,t} = \tanh z_{x,t}, \quad z_{x,t}\in(-\infty,\,+\infty). \tag{4.53}$$

Effectively we introduce "soft walls" on the borders of initial integration domain $[-1;\ 1]$. It also allows us to treat the integration contours in a similar manner as in the case of Gaussian HS transformation. For example, we do not need to attach the shifted contours to the points ± 1 at real axis in order to preserve the value of the integral. Here is the final form of the partition function:

$$\mathcal{Z}_n = \int_{-\infty}^{+\infty} \mathcal{D}z_{x,t} e^{-S_n(z_{x,t})},$$
$$S_n(z_{x,t}) = 2\sum_{x,t} \ln\cosh z_{x,t} -$$
$$- \ln\left(\det\left(P\right)_{el.}\left(\tanh z_{x,t}\right)\det\left(P\right)_{h.}\left(\tanh z_{x,t}\right)\right) \tag{4.54}$$

The introduction of the hyperbolic functions does not make the calculation much more expensive then the Gaussian approach (4.35), because we need to compute the complex exponents in fermionic determinants (4.15) and (4.52) in any case. Thus, additional calculation of the exponent e^z needed for the evaluation of hyperbolic functions doesn't introduce significant additional difficulty in the algorithm. However, we should mention that this change of variables might be not the most efficient choice. Probably, some other variants should be tested.

This representation suffers from the same ergodicity problem (see eq. (4.28)) which appears if we use Gaussian HS transformation with only complex exponents: domain walls formed by configurations with zero fermionic determinant. It can be solved using the same trick with combination of real and complex exponents. The same derivation for real exponents gives us

$$e^{-\frac{\delta U}{2}(\hat{n}_{el.}-\hat{n}_{h.})^2} = \frac{1}{2}\int_{-1}^{1} e^{\lambda x(\hat{n}_{el.}-\hat{n}_{h.})} dx, \tag{4.55}$$

where constant λ is defined as

$$e^{\frac{\delta U}{2}} = \frac{\sinh\lambda}{\lambda}. \tag{4.56}$$

So we can combine it with (4.49) and get rid of the "domain walls".

Now we study the one-site Hubbard model using the new path integral representation with only complex exponents and compare our results with [117]. According to (4.54), the action should be written as

$$S_n^{(1)}(z) = 2\ln\cosh z -$$
$$- \ln\left((1+e^{i\gamma\tanh z-\beta\mu})(1+e^{-i\gamma\tanh z+\beta\mu})\right). \tag{4.57}$$

Complex saddle points as well as corresponding thimbles and anti-thimbles are shown in the figure 4.17 for the same interaction strength $U\beta = 15.0$ and four different values of the chemical potential. Since the action is periodic along the imaginary axis with period 2π (and this property is preserved in the case of full many-site Hubbard model), we can

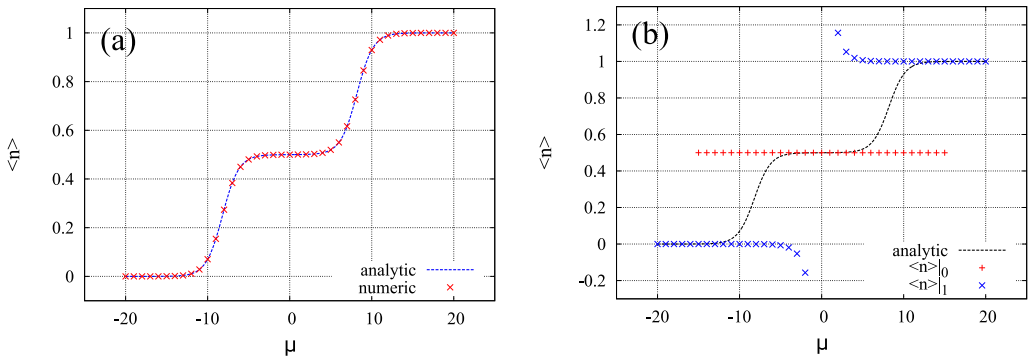

Figure 4.18: (a) Average number of particles $\langle \hat{n} \rangle$ computed with the non-Gaussian integral representation for the one-site Hubbard model (4.58). (b) Contribution of different thimbles to the average number of particles $\langle \hat{n} \rangle|_0$ and $\langle \hat{n} \rangle|_1$ computed with the non-Gaussian integral representation for the one-site Hubbard model (4.59). Analytic result is also shown for comparison, $U\beta = 15.0$.

look only at the strip $\mathrm{Im}\, z \in [-\pi, \pi]$. Unlike the Gaussian case (fig. 4.3a), we have only one relevant thimble at half filling which coincides with the whole real axis. An important property of the representation (4.54) is that the action has now an additional singular points, namely, the poles at $\mathrm{Im}\, z = \pm\pi/2$, $\mathrm{Re}\ z = 0$. All anti-thimbles now should end up at one or both of these points. Obviously, anti-thimbles corresponding to relevant saddle points start at one pole and end up at another one with an opposite sign of $\mathrm{Im}\, z$.

This behaviour is indeed clearly seen in the figure 4.17. Initially, at small chemical potential, we still have the situation where only the "vacuum" saddle point at $z = 0$ is relevant. However, at larger values of μ the Stokes phenomenon happens where anti-thimbles of two initially irrelevant saddle points collide with the former "vacuum" saddle point. Subsequently, three anti-thimbles pass from one pole to another crossing the real axis. After the Stokes phenomenon the situation with only three relevant saddles persists even at very large values of chemical potential $\mu > U$. This is already quite different situation from the Gaussian case with complex exponents, where the series over thimbles (4.20) is infinite. In this sense we are already closer to the Gaussian HS transformation with only real exponents.

The role of saddle points in the new representation is clarified in the figure 4.18. This figure illustrates the contribution to the average number of particles $\langle \hat{n} \rangle$ from different thimbles. The full observable is equal to

$$\langle \hat{n} \rangle = \frac{\sum_{\sigma=0,\pm1} \int_{\mathcal{I}_\sigma} dz e^{-S_n^{(1)}} \left(1 + e^{i\gamma \tanh z - \mu\beta}\right)^{-1}}{\sum_{\sigma=0,\pm1} \int_{\mathcal{I}_\sigma} dz e^{-S_n^{(1)}}}, \tag{4.58}$$

where $\sigma = 0, \pm 1$ denotes all three relevant thimbles. The full sum is shown in the figure 4.18a and indeed, the values obtained via integral over thimbles coincides completely with the analytic answer. The role of different thimbles is revealed if we plot the observable

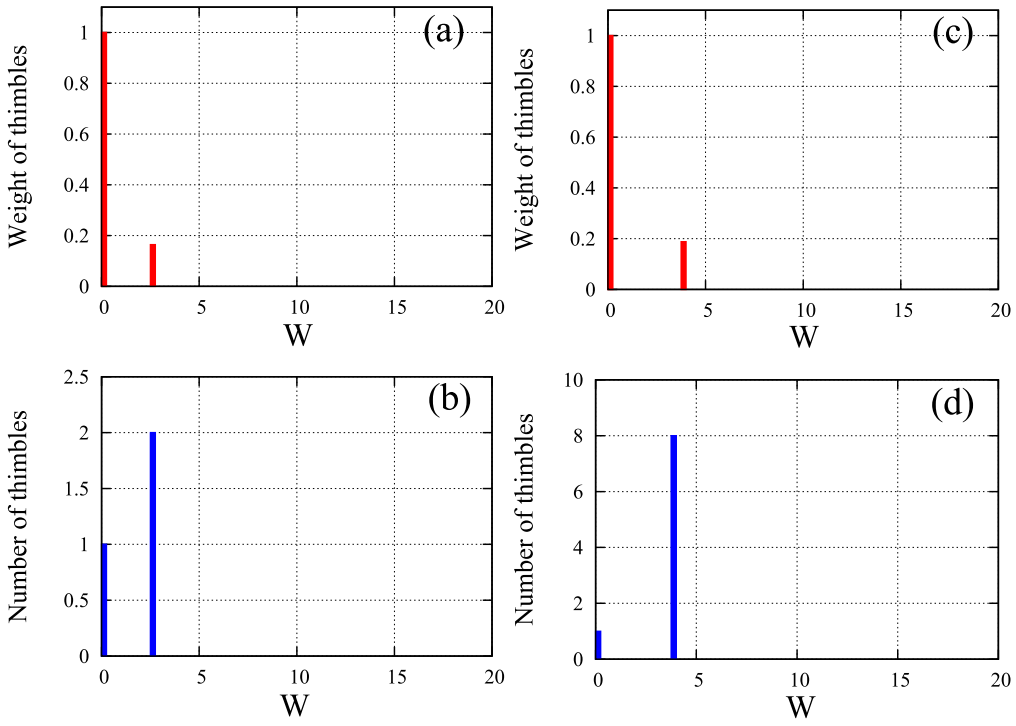

Figure 4.19: Weighted and normal histograms for relevant thimbles at half-filling for two-site ((a) and (b)), four-site ((c) and (d)) lattice. Non-Gaussian representation is used, $N_t = 1$ in all cases. The action is written according to equations (4.54), (4.52), (4.17) with parameters: $U\beta = 15.0$, $\kappa\beta = 3.0$. Weight of thimbles is shown with respect to the vacuum one.

calculated only at given thimbles:

$$\langle \hat{n} \rangle|_0 = \frac{\int_{\mathcal{I}_0} dz e^{-S_n^{(1)}} \left(1 + e^{i\gamma \tanh z - \mu\beta}\right)^{-1}}{\int_{\mathcal{I}_0} dz e^{-S_n^{(1)}}},$$
$$\langle \hat{n} \rangle|_1 = \frac{\sum_{\sigma \pm 1} \int_{\mathcal{I}_\sigma} dz e^{-S_n^{(1)}} \left(1 + e^{i\gamma \tanh z - \mu\beta}\right)^{-1}}{\sum_{\sigma \pm 1} \int_{\mathcal{I}_\sigma} dz e^{-S_n^{(1)}}}. \tag{4.59}$$

$\langle \hat{n} \rangle|_0$ represents the contribution from "vacuum" thimble and $\langle \hat{n} \rangle|_1$ corresponds to the contribution from two others (they are complex conjugate to each other, thus making equal contribution to the real observable). Figure 4.18b demonstrates these quantities. One can see that the "vacuum" thimble gives a good approximation to $\langle \hat{n} \rangle$ for small chemical potential while two others work well for $\mu \geq U$ after the transition. We should stress that $\langle \hat{n} \rangle \neq \langle \hat{n} \rangle|_0 + \langle \hat{n} \rangle|_1$ because of different normalization in the denominators of eq. (4.58) and (4.59).

We see that in this model the phase transition reflects itself in the transfer of statistical weight from one saddle point (former "vacuum") to a couple of others which are complex conjugate to each other. Thus, everywhere except the transition region, $\mu \approx U$, there is one (or two complex conjugated) thimbles which provide the dominant contribution to observable. This property when just one thimble (or the group of equivalent thimbles)

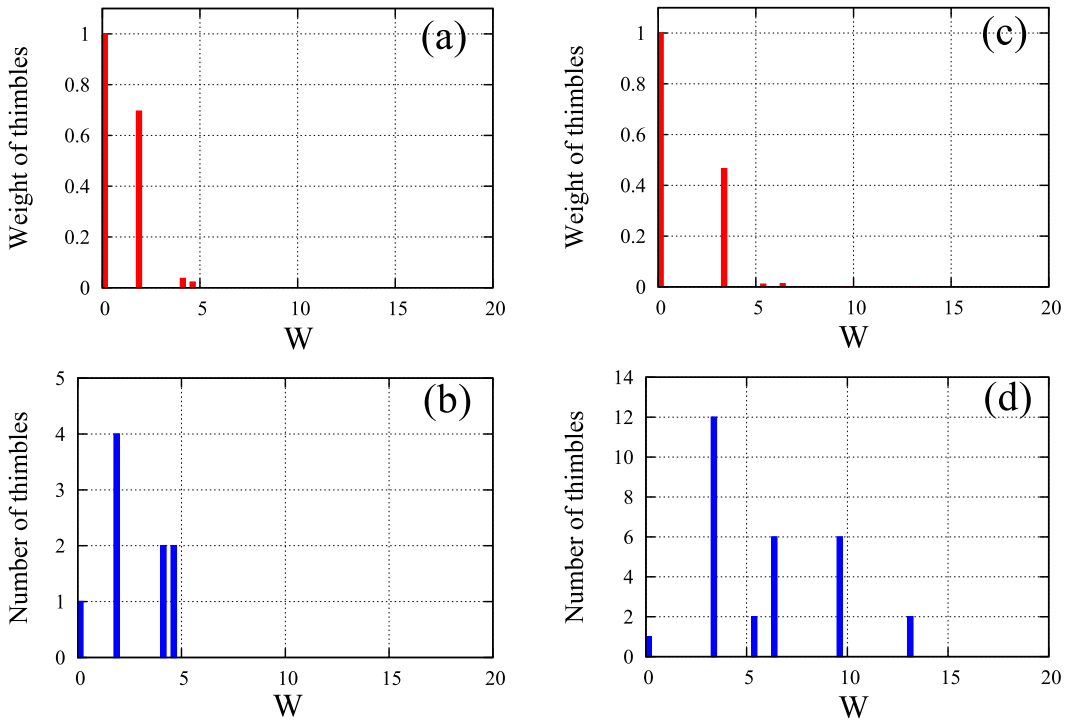

Figure 4.20: Weighted and normal histograms for relevant thimbles at half-filling for two-site lattice with two ((a) and (b)) and three ((c) and (d)) Euclidean time slices. Non-Gaussian representation is used, the action is written according to equations (4.54), (4.52), (4.17) with parameters: $U\beta = 15.0$, $\kappa\beta = 3.0$. Weight of thimbles is shown with respect to the vacuum saddle.

gives a good approximation for particular phase is very useful in real calculations, because it reduces the problems with ergodicity in QMC. However, we don't know, how this situation will change in the thermodynamic limit, this should be a subject of further study.

Interestingly, we can now introduce the topological invariant to distinguish relevant and irrelevant saddle points. This possibility relies on the fact that anti-thimbles for irrelevant saddle points have both their ends at one pole, while anti-thimbles for relevant saddles should connect both poles. The invariant for the σ-th saddle point can be written as

$$\mathcal{T}_\sigma = \frac{1}{i\pi} \int_{\mathcal{K}_\sigma} dz, \tag{4.60}$$

where the integral is taken over corresponding anti-thimble. The invariant is equal to 1 for relevant saddle point and 0 for irrelevant. The possibility to generalize this formula to larger dimensions also exists but should be a subject of further study. In principle, the existence of such invariant can help in the detection of relevant saddle points, because we do not need to search for the intersection point, which might be very non-trivial task in many dimensions.

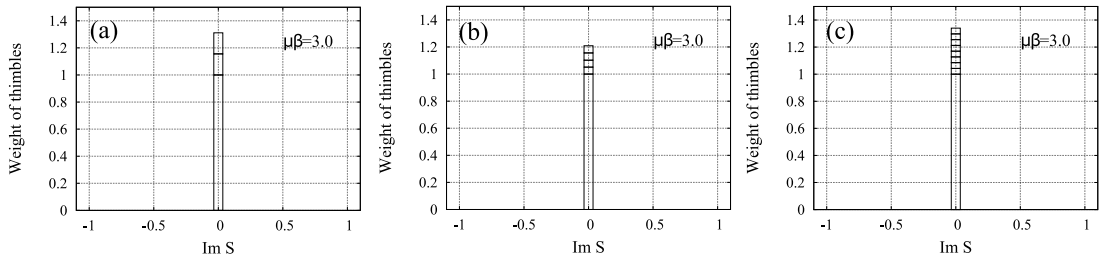

Figure 4.21: Stacked histograms showing the evolution of real thimbles which were relevant at half-filling. Calculations are made for non-Gaussian representation. Since ImS remains zero for all thimbles, they form only one bar in the histograms. Contributions of these thimbles are separated by horizontal lines within the bar. The weight of former "vacuum" thimble is taken as unity. The calculation is made for two-site lattice with $N_t = 1$ (a) and $N_t = 2$ (b); and for four-site lattice with $N_t = 1$ (c). The action is written according to equations (4.54), (4.52), (4.17) with parameters: $U\beta = 15.0$, $\kappa\beta = 3.0$, $\kappa\mu = 3.0$.

4.5.2 Few-site Hubbard model

Next we study the behaviour of the non-Gaussian integral representation of the interaction term in case of the Hubbard model with few lattice sites. We take the action (4.54). In order to make direct comparison, the same parameters ($U\beta = 15.0$ and $\kappa\beta = 3$) are used as was done for the Gaussian representation. The same approach is also used for the estimation of the complexity of the sign problem: we start from half filling and identify all relevant real saddle points; after it we trace their shift in the complex plane with increasing chemical potential and look at the evolution of their phases.

The results for the two- and four-site lattices with $N_t = 1$ at half filling are shown in the figure 4.19 in the usual manner (normal and "weighted" histogram for relevant real saddles). The most important feature of the new path integral representation is still preserved: instead of an infinite number of relevant saddles we have only finite number of them within the real subspace. Importantly, the "weighted" histogram shows that the vacuum saddle still dominates in the sum (4.20). The number of sub-dominant thimbles grows with N_s, but their role in the sum (4.20) remains stable, as one can see from the figures 4.19b and 4.19d. Thus we have similar competition between exponentially increasing number of relevant thimbles and their exponentially decreasing weight as we observed in the case of the real Gaussian HS transformation. The only difference is that the weight of sub-dominant thimbles is substantially decreased and the "vacuum" thimble always dominates.

The scaling with N_t is shown in the figure 4.20 for two-site lattice with $N_t = 2$ and $N_t = 3$. Comparison of fig. 4.20a and 4.20c shows that that the overall weight of sub-dominant thimbles decreases, despite that their number increases with N_t.

However, these sub-dominant thimbles are not a large issue from the point of view of the sign problem. The results for the former real saddles in the case of increased chemical

potential (see fig. 4.21) are shown for the following lattices: 1) $N_s = 2$, $N_t = 1$; 2) $N_s = 2$, $N_t = 2$; 3) $N_t = 4$, $N_t = 1$. In all cases we see only saddle points with $\mathrm{Im}S = 0$. Thus the sign problem is significantly milder in comparison with the case of the Gaussian HS transformation with complex exponents and situation reminds more the Gaussian case with only real exponents.

4.6 Conclusions

The Lefschetz thimble analysis of the sign problem was made for the few-site Hubbard model combining the analytic study of the lattices with few Euclidean time slices and the results from HMC simulations on the lattices with large N_t, approaching the continuous limit. In this study, we found all relevant saddles in the real subspace $\mathbb{R}^N$ at half filling and looked at their relative importance using the Gaussian approximation to the integrals over thimbles. After it we track the evolution of these real saddles (including the shift in the complex domain) with increasing chemical potential and look at the phases which they acquire. In principle, some additional relevant saddles can appear or former real saddles can become irrelevant. However, since the action is a continuous function of the chemical potential, additional saddles can not suddenly become dominant. Thus, such an incomplete study still gives a reasonable estimate of the complexity of the sign problem at small values of chemical potential.

Two variants of the Gaussian HS transformation were studied. They differ by the presence of real or complex exponents with Hubbard fields in the fermionic determinant. Hubbard fields are coupled to particle number operators for electrons and holes. In both cases the complexity of the sign problem (the number of significant thimbles and the fluctuations of their sign) increases with the spatial size of lattice. On the contrary, the continuous limit $N_t \to \infty$ makes the sign problem milder by lifting the non-uniform saddle points and decreasing their contribution in the overall sum over relevant thimbles. The variant with only real exponents in fermionic determinant exhibits much milder sign problem due to finite number of relevant thimbles and much smaller fluctuations of their phases.

The minimal number of relevant thimbles is observed when both real and complex exponents are mixed in the action (thus two auxiliary fields per lattice site should be introduced). This regime needs some tuning of the parameter α which defines the relative importance of real and complex exponents in the decomposition of the interaction term. Generally, we should work in the regime closer to the case with only complex exponents ($\alpha \approx 0.9$). In this case the number of relevant thimbles is equal to two for all few-site lattices studied in this work. Data from HMC test runs also support the claim that this is the most advantageous regime for possible application of Generalized thimble algorithm for the Hubbard model.

We present also another example of the representation where the number of relevant thimbles is substantially reduced. An alternative integral representation for the interaction term is derived using the analogy with BSS-QMC. Analysis made on lattices with $N_s = 1, 2, 4$ and $N_t = 1, 2, 3$ shows that the number of relevant thimbles is always finite and the "vacuum" saddle point located at zero auxiliary fields is always dominant (at least for moderate values of the chemical potential $\mu \approx \kappa$). Moreover, the calculation with finite chemical potential shows that all former real saddles move into complex domain but still preserve zero ImS. It means that at small values of chemical potential the complexity of the sign problem for the non-Gaussian representation is comparable to the case of Gaussian HS transformation with purely real exponents. Additionally, in non-Gaussian representation we can write the topological invariant for the detection of relevant saddle points, at least in the simplest case of one-site Hubbard model.

We also describe some difficulties arising in QMC with continuous auxiliary fields due to the presence of the field configurations with zero fermionic determinant. First of all, the dimension of the manifolds formed by these field configurations is equal to $N - 1$ in $\mathbb{R}^N$ if we work both in the limit with only complex or only real exponents. It means that in both limits we have the "domain walls" which divide the integration domain into disconnected regions. These "domain walls" are impenetrable for Hamiltonian updates of HMC algorithm thus it suffers from the ergodicity problems in both of these limits. This is an additional argument why the mixed regime with both types of exponents present in the action should be used. In the mixed regime the dimensionality of the manifolds with zero fermionic determinant is equal to $N - 2$. The appearance of these configurations leads also to the heavy tailed distribution for physical observables. Since the second moment is not defined for these distributions, the statistical post-processing of the Monte Carlo data should be made carefully enough to give correct estimation of errors.

Chapter 5

Overlap fermions in real-time lattice simulations of anomalous transport

5.1 Introduction

Transport phenomena related to quantum anomalies of chiral fermions might have profound impact on the properties of dense chiral medium, which can be realized in Dirac or Weyl semimetals, in neutrino/leptonic matter in astrophysical contexts and in quark-gluon plasma. It is by now commonly accepted that such phenomena as the Chiral Magnetic Effect and the Chiral Magnetic Wave cannot exist in equilibrium [56]. For this reason first-principle numerical studies of anomalous transport require real-time simulation techniques, especially if the relevant dynamics is strongly nonlinear, as in the case of chiral plasma instability [57, 139] or chiral shock waves [140].

Currently the state-of-the-art method for real-time simulations is the classical-statistical approximation, in which the gauge fields are treated as classical, but the dynamics of fermions is fully quantum. So far most real-time simulations of anomalous transport phenomena have been performed with Wilson-Dirac fermions, for which the chiral symmetry is explicitly broken by the Wilson term. At the same time, Wilson term is responsible for axial anomaly of Wilson fermions (see e.g. [141] for a recent real-time study). It is therefore important to understand, how lattice artifacts of Wilson fermions can affect anomalous transport, and how these artifacts can be reduced. One practical solution considered recently in [142] is the improvement of the Wilson-Dirac operator which removes lattice artifacts up to some fixed order $\mathcal{O}\left(a^n\right)$ in lattice spacing a.

In this Chapter we advocate the use of overlap Hamiltonian, first proposed in [143], for real-time classical-statistical simulations of chiral medium. We demonstrate that even on small lattices the real-time dynamics of overlap fermions reproduces the results

known for continuum Dirac fermions with very good precision. In contrast, for Wilson-Dirac fermions the effects of explicit chiral symmetry breaking is significant even on large lattices, especially for quickly changing electromagnetic fields. As a test case, we consider the generation of axial charge density in parallel electric and magnetic fields. If gauge fields are considered dynamical, this process corresponds to the formation of Chiral Magnetic Wave mixed with plasmon.

This Chapter is organized as follows. In the Section 5.2 we present basics of quantum axial anomaly and of anomalous transport phenomena. In the Section 5.3 we give basic information about chiral fermions on the lattice. Finally, in the remaining Sections we study overlap fermions in the real-time CSFT simulations in scenarios related to anomalous transport of chiral fermions.

5.2 Anomalous transport of chiral fermions

5.2.1 Chiral symmetry and Axial anomaly

Notions of chiral symmetry and axial anomaly are in the heart of the anomalous transport phenomena. In order to introduce these concepts we start with a theory of N_f flavors of free massless Dirac fermions described by the standard action:

$$S_f = \sum_{i=1}^{N_f} \int \mathrm{d}^4x\, \bar{\psi}_i i \not{D} \psi_i, \qquad \not{D} = \gamma^\mu D_\mu, \qquad D_\mu = \partial_\mu + iA_\mu, \tag{5.1}$$

where D_μ is a covariant derivative, ψ and $\bar{\psi} = \psi^\dagger \gamma^0$ are spinor fields, γ^μ are standard anti-commuting Dirac matrices, A_μ is vector-potential and the coupling constant g is absorbed into definition of A_μ. This action is invariant under $SU_V(N_f) \times SU_A(N_f) \times U_V(1) \times U_A(1)$ symmetry transformations describing rotations of N_f fermion flavors, where subscripts V and A stand for vector and axial transformations.

Vector transformations can be written in the following form:

$$SU_V(N_f): \qquad \psi \to e^{i\theta t^a}\psi, \qquad \bar{\psi} \to \bar{\psi} e^{-i\theta t^a}, \tag{5.2}$$

$$U_V(1): \qquad \psi \to e^{i\theta \mathbb{1}}, \qquad \bar{\psi} \to \bar{\psi} e^{-i\theta \mathbb{1}}, \tag{5.3}$$

where t^a are $N_f^2 - 1$ generators of $SU(N_f)$ group acting on the flavor indices and $\mathbb{1}$ is corresponding identity operator. In a classical field theory according to Noether's theorem these symmetries are associated with classically conserved vector currents:

$$j^{\mu,a} = \bar{\psi}\gamma^\mu t^a \psi, \tag{5.4}$$

$$j^\mu = \bar{\psi}\gamma^\mu \psi, \tag{5.5}$$

where we omit the identity operator $\mathbb{1}$ for brevity. The symmetry is called "vector" since corresponding currents transform as vectors under Lorentz transformations.

Axial transformations read as:

$$SU_A(N_f): \qquad \psi \to e^{i\theta\gamma_5 t^a}\psi, \qquad \bar{\psi} \to \bar{\psi}e^{i\theta\gamma_5 t^a}, \tag{5.6}$$

$$U_A(1): \qquad \psi \to e^{i\theta\gamma_5 \mathbb{1}}, \qquad \bar{\psi} \to \bar{\psi}e^{i\theta\gamma_5 \mathbb{1}}, \tag{5.7}$$

where $\gamma_5 = i\gamma_0\gamma_1\gamma_2\gamma_3$ is a chiral operator which distinguishes right- and left-handed Weyl components of Dirac field:

$$\psi_\pm = P_\pm\psi, \qquad P_\pm = \frac{1 \pm \gamma_5}{2}, \qquad \gamma_5\psi_\pm = \pm\psi_\pm, \tag{5.8}$$

where $P_\pm$ are chiral projectors. Corresponding classically conserved axial currents can be written as:

$$j_5^{\mu,a} = \bar{\psi}\gamma_5\gamma^\mu t^a\psi, \tag{5.9}$$

$$j_5^{\mu} = \bar{\psi}\gamma_5\gamma^\mu\psi. \tag{5.10}$$

In terms of chiral projections (5.8) the action (5.1) is decomposed into a set of independent Weyl fermions corresponding to different chiral components of Dirac field:

$$S_f = S_+ + S_-, \qquad S_\pm = \sum_{i=1}^{N_f} \int \mathrm{d}^4x\, \bar{\psi}_{i,\pm} i\not{D}\psi_{i,\pm}. \tag{5.11}$$

Fermionic currents $j_\pm^\mu$ of right- and left-handed particles can be expressed as linear combinations of conserved vector (5.5) and axial (5.10) currents:

$$j_\pm^\mu = \bar{\psi}_\pm\gamma^\mu\psi_\pm = \left(j^\mu \pm j_5^\mu\right)/2, \tag{5.12}$$

therefore in a classical theory each Weyl component of Dirac field evolves separately maintaining conservation of the currents $j_\pm^\mu$.

The fate of these symmetries is non-trivial in quantum field theory. In the presence of strong interactions the group $SU_V\left(N_f\right) \times SU_A\left(N_f\right)$ can be spontaneously broken due to emergence of the chiral condensate $\langle\, \bar{\psi}\psi \,\rangle$ which acts as effective mass term mixing chiralities. This effect is important for understanding anomalous transport in strongly interacting theories, however detailed discussion goes beyond the scope of the this work.

Furthermore, classical $U_A\left(1\right)$ symmetry is explicitly broken in quantum field theory because of famous Adler-Bell-Jackiw (ABJ) axial anomaly:

$$\partial_\mu j_5^\mu = -\frac{N_f}{16\pi^2} F_{\mu\nu}\tilde{F}^{\mu\nu}, \tag{5.13}$$

where $F_{\mu\nu} = \partial_\mu A_\nu - \partial_\nu A_\mu$ is the stress-tensor of a (non-Abelian) background gauge field and $\tilde{F}^{\mu\nu} = \frac{1}{2}\epsilon^{\mu\nu\alpha\beta}F_{\alpha\beta}$ is a dual stress-tensor.

The axial anomaly (5.13) appears already at the first order of perturbation theory which is given by the triangle diagram. Moreover, it was shown that this result is exact

and higher-order terms do not introduce any corrections. This surprising result can be understood as inability to regularize the theory at the UV scale while maintaining chiral symmetry and vector charge conservation simultaneously.

Let us sketch derivation of the anomaly following Fujikawa's approach. To this end we note that axial transformations (5.7) of the action (5.1) generate non-trivial Jacobian associated with fermionic integration measure of the path integral:

$$\mathcal{D}\psi\mathcal{D}\bar{\psi} \to \mathcal{D}\psi\mathcal{D}\bar{\psi}\det\left[i\theta\gamma_5\right] = \mathcal{D}\psi\mathcal{D}\bar{\psi}e^{-S_\theta}, \quad \text{where} \quad S_\theta = i\mathrm{Tr}\,\left[\theta\gamma_5\right]. \tag{5.14}$$

The trace operator in the expression for S_θ implies summation over all suitably chosen fermion states, therefore it is affected to UV divergences. Moreover, because of the structure of γ_5 operator it consists of a difference of two divergent pieces, thus it requires careful regularization in order to obtain well-defined results. It turns out that any reasonable regularization scheme which preserves gauge invariance inevitably breaks axial symmetry at UV scale and the trace operator leads to non-vanishing contribution to the action responsible for the anomaly:

$$S_\theta = i\frac{N_f}{16\pi^2}\int \mathrm{d}^4x\,\theta F_{\mu\nu}\tilde{F}^{\mu\nu}. \tag{5.15}$$

Let us note that from this perspective it is clear that additional mass term $m\bar{\psi}\psi$ in the action will not eliminate the anomaly but will rather lead to a new term $2m\langle\,\bar{\psi}i\gamma_5\psi\,\rangle$ on the r.h.s of the equation (5.13) accounting for explicit symmetry breaking.

For detailed derivation using this and other approaches we refer to the literature. In what follows we will consider important aspects of the axial anomaly relevant for anomalous transport.

Let us consider distinct chiral components of Dirac fermions separately according to equation (5.11). Then anomaly equation (5.13) can also be viewed as non-conservation of a charge of Weyl fermions in a background of gauge fields:

$$\partial_\mu j^\mu_\pm = \mp\frac{N_f}{4\pi^2}\mathbf{E}\cdot\mathbf{B}. \tag{5.16}$$

This effect is especially transparent if we consider a system of Dirac fermions in strong magnetic field $\mathbf{B}$ (much stronger than other relevant energy scales of the problem). In this situation energy spectrum is described by Landau levels:

$$\begin{aligned}\epsilon_n &= \pm\sqrt{k^2+2Bn},\\ \epsilon_0 &= \pm k.\end{aligned} \tag{5.17}$$

It is important that while higher Landau level $n>0$ are doubly degenerate with respect to spin, the lowest Landau levels (LLL) are not and they are chiral. Since contributions of levels $n>0$ are suppressed by a gap $\sqrt{2Bn}$, the low energy physics is dominated by LLLs.

Due to chiral nature particles on LLLs can be effectively described as $1+1$-dimensional fermions moving parallel to magnetic field. In the background of electric field $\mathbf{E}$ (parallel to magnetic field) evolution of such states is given by equation $\dot{\mathbf{k}} = -\mathbf{E}$ which describes electrons disappearing from the right-moving level and appearing on the left-moving level. Therefore electric charge is not conserved on individual LLLs and we observe so-called $1D$ axial anomaly $\dot{q}_{\pm} = \mp E/(2\pi)$, where $q_{\pm}$ is a density of the charge. Taking into account the number of flavors N_f and the degeneracy of each Landau level which is proportional to magnetic flux $B/(2\pi)$ one obtains correct expression for $3D$ axial anomaly (5.16) in a particular case when electromagnetic fields are spatially uniform (this implies $\nabla \cdot \mathbf{j} = 0$).

We note that axial anomaly is an example of all-scale phenomenon. Indeed, emergence of chiral Landau levels is a feature of IR physics . On the other hand, in order to derive expression (5.13) a careful regularization at the UV scale was necessary. These facts are important for understanding axial anomaly in lattice quantum field theory and in solids such as Weyl semimetals, where underlying lattice structure can be considered as a natural gauge-invariant regularization which at the same time breaks chiral symmetry at higher energies. We will consider these issues in more details in the Section dedicated to chiral fermions in lattice systems.

Finally, this discussion would not be complete without mentioning importance of axial anomaly for non-Abelian gauge theories, including QCD and electroweak sector of the Standard model. We note that r.h.s. of the equation (5.13) is a total derivative of the Chern-Simons current:

$$K^{\mu} = 2\epsilon^{\mu\nu\alpha\beta}\mathrm{tr}\left(A_{\nu}F_{\alpha\beta} + \frac{2}{3}iA_{\nu}A_{\alpha}A_{\beta}\right), \tag{5.18}$$

so that the change of the fermionic axial charge $Q_5 = \int \mathrm{d}^3x\, j_5^0(x)$ over time $\Delta Q_5 = Q_5(t=+\infty) - Q_5(t=-\infty)$ is related to topological Chern-Simons number Q_{CS} of gauge fields:

$$\Delta Q_5 = 2Q_{CS}, \tag{5.19}$$

$$Q_{CS} = \frac{N_f}{32\pi^2}\int \mathrm{d}^4x\, \partial_{\mu}K^{\mu}, \tag{5.20}$$

where we assume vacuum boundary conditions. In this form of so-called index theorem the axial anomaly relates non-trivial topological vacuum structure of non-Abelian gauge theories (e.g. of QCD) to fermionic observables.

5.2.2 Chiral Magnetic Effect and anomalous transport

The emergence of anomalous transport is tightly connected to a notion of chirally imbalanced media. A medium is called chirally imbalanced if it consists of different number

of left- and right-handed particles. In different systems chiral imbalance can be created using different mechanisms. For example, this can be achieved with the help of chirality pumping process: in the background of parallel electric and magnetic fields the number of left- and right-handed fermions is not conserved due to axial anomaly (5.16). In QCD it can be created according to index theorem (5.19) by sphalerons which describe real-time transitions between different topological sectors of gluon field. Another mechanism which might be relevant to astrophysics is that in weak interactions only left-handed components of fermions participate, therefore produced neutrinos can carry away some amount of chirality from the system.

In order to describe such systems one can parameterize chiral imbalance by so-called chiral chemical potential μ_A which couples to axial charge:

$$S_5 = \sum_{i=1}^{N_f} \int d^4x \, \mu_A \bar{\psi}_i \gamma_5 \gamma^0 \psi_i. \tag{5.21}$$

With the help of axial transformations (5.7) in a local form it is possible to eliminate term S_5 in the expense of the theta-term S_θ (5.15) if $\theta \equiv \theta\,(x^\mu) = \mu_A\, x^0$. Since in this case parameter θ is space-time dependent, it can be interpreted as axion field and one can expect emergence of new interesting transport phenomena.

Indeed, calculation shows that chirally imbalanced media support novel anomaly-related transport called Chiral Magnetic Effect: in a response to applied external magnetic field $\mathbf{B}$ a macroscopic electric current $\mathbf{j}$ is generated:

$$\mathbf{j} = \sigma_{CME}\, \mathbf{B}, \tag{5.22}$$

where σ_{CME} is so-called chiral magnetic conductivity:

$$\sigma_{CME} = \frac{N_f\, \mu_A}{2\pi^2}. \tag{5.23}$$

From this perspective it is clear that CME is directly related to the presence of axial anomaly and that σ_{CME} is fixed by a coefficient in the anomaly equation (5.13).

An intuitive picture behind CME is the following. Assume that a medium consisting of different number of left- and right-handed chiral fermions is subjected to external magnetic field. If the field is strong enough, particles will tend to (counter-)align their spins with magnetic field. Because the spin of chiral fermions is (anti-) parallel to the direction of momentum, right-handed particles of positive charge will move along the magnetic field and right-handed particles of negative charge will move against magnetic field. In total, there will be a non-vanishing electric current of right-handed fermions. Accordingly, left-handed fermions will also produce a current in the opposite direction. In a chiraly imbalanced medium these two currents will not compensate each other and therefore a net electric current directed along magnetic field will be generated.

Chiral Magnetic Effect is probably one of the best known in the family of anomalous transport phenomena. Let us mention a tightly connected to CME Chiral Separation Effect (CSE) which amounts to generation of axial current in the background of external magnetic field in a medium at a finite density:

$$\mathbf{j}_5 = \sigma_{CSE}\,\mathbf{B}, \qquad \sigma_{CSE} = \frac{N_f\,\mu}{2\pi^2}, \tag{5.24}$$

where μ is a chemical potential. In rotating chiral fluids there is also a similar to CME effect called Chiral Vortical Effect:

$$\mathbf{j} = \sigma_{CVE}\,\boldsymbol{\omega}, \qquad \sigma_{CVE} = \frac{N_f\,\mu\,\mu_A}{\pi^2}, \tag{5.25}$$

where $\boldsymbol{\omega} = \frac{1}{2}\nabla \times \mathbf{u}$ is a vorticity and $\mathbf{u}$ is a fluid element velocity.

Chiral Magnetic Effect is very appealing since 1) in contrast to axial currents, electric currents are routinely measured in experiments and 2) parity of quantities in the expression (5.22) under time ($\mathcal{T}$) reflections suggest dissipation-free nature of this effect. Indeed, because electric current and magnetic field are $\mathcal{T}$-odd quantities, chiral magnetic conductivity σ_{CME} should be $\mathcal{T}$-even. This is in contrast to ordinary dissipating Ohmic transport $\mathbf{j} = \sigma\,\mathbf{E}$ where conductivity σ is $\mathcal{T}$-odd. According to the second law of thermodynamics dissipative processes increase entropy of the system and because of that two possible direction of time are no longer equal. This suggests that dissipative transport should be described by $\mathcal{T}$-odd transport coefficients as in the case of Ohm's law, whereas $\mathcal{T}$-even coefficients might indicate absence of dissipation.

However, this argument implies that CME current in the naive form (5.22) can exist as a persistent current in a background state in contradiction to requirements of gauge invariance: applying arbitrary weak electric field $\mathbf{E}$ to such system one can perform work and obtain energy from the ground state which is impossible.

This contradiction is resolved if we allow magnetic field to vary in space and time. Then chiral magnetic conductivity become a function of wave vector $\mathbf{k}$ and frequency ω of applied field. Analysis reveals that in the limit of static and slowly varying in space magnetic field conductivity $\sigma_{CME}\left(\omega, \mathbf{k}\right)$ become sensitive to IR definition of the system and in particular in finite-sized crystallines it vanishes in agreement to requirements of gauge invariance. At the same time, the opposite limit of spatially uniform and slowly varying in time field corresponds to non-stationary process, therefore these arguments do not apply and CME in the naive form (5.22) is allowed.

Complications mentioned above and necessity to create chiral imbalance makes direct observation of CME difficult. However, anomalous transport phenomena lead to a number of important consequences for chiral media which can be potentially detected in experiments.

First of all, interplay of CME and CSE leads to novel gapless excitations in chiral media called Chiral Magnetic Waves (CMW). We note that local fluctuations of vector

and axial charges $\delta q_{V/A}$ can be related to fluctuations of corresponding local chemical potentials $\delta\mu_{V/A}$ via constitutive equations: $\delta q_{V/A} = \chi_{V/A}\,\delta\mu_{V/A}$, where susceptibilities $\chi_{V/A}$ take into account details of a particular medium. Consequently, in the background of external magnetic field fluctuations of vector and axial currents can be induced according to CME (5.22) and CSE (5.24). Using (non-)conservation laws for these currents $\partial_\mu j^\mu_{V/A} = 0$ and constitutive equations one can obtain a system of coupled equations which describes collective massless excitations propagating in the direction of magnetic field: Chiral Magnetic Waves. We will give an explicit example of this phenomenon in the Section 5.4 in the case when external magnetic field is very strong (so-called quantum limit).

Another interesting effect is so-called Chiral Plasma Instability. Let us consider a chirally imbalanced matter interacting with dynamical electromagnetic field. To this end one can write down classical Maxwell equation in the basis of plane waves $\exp\left[i\left(\mathbf{k}\cdot\mathbf{x} - \omega t\right)\right]$ and coupled to CME current:

$$i\omega\mathbf{B} = -\mathbf{k}\times\mathbf{E} \qquad i\omega\mathbf{E} = \mathbf{k}\times\mathbf{B} - \sigma_{CME}\left(\omega,\mathbf{k}\right)\,\mathbf{B}. \tag{5.26}$$

If we simplify analysis and take CME in the naive form (5.22) then this system of equations describes excitations with dispersion relation $\omega = \pm\sqrt{k\left(k \pm \sigma_{CME}\right)}$. In the kinematic region $0 < k < \sigma_{CME}$ there is a growing exponentially in time solution signaling an instability. When this instability develops the chiral charge of fermions is expected to decay in the expense of helicity of unstable electromagnetic modes according to anomaly equation (5.13). A more rigorous consideration employing chiral kinetic theory and lattice real-time simulations support these expectations.

5.3 Lattice fermions and problem of doublers

5.3.1 Naive lattice fermions

In contrast to gauge fields, construction of chiral lattice fermions is a subtle issue. In order to see why, let us consider naively discretized Dirac Hamiltonian:

$$\hat{H}_f = a^3\sum_{\mathbf{xy}}\hat{\psi}^\dagger_{\mathbf{x}}\tilde{h}_{\mathbf{xy}}\hat{\psi}_{\mathbf{y}}, \qquad \tilde{h}_{\mathbf{xy}} = \sum_{i=1}^{3} -i\alpha_i\nabla_{i,\mathbf{xy}} + M\gamma_0\delta_{\mathbf{xy}}, \tag{5.27}$$

where $\tilde{h}_{\mathbf{xy}}$ is a single-particle Hamiltonian, $\alpha_i = \gamma_0\gamma_i$ are Dirac alpha matrices, M is the mass and $\nabla_{i,\mathbf{xy}}$ is a lattice covariant derivative (**??**).

Let us consider free fermions $U_{\mathbf{x},i} \equiv 1$ and diagonalize this Hamiltonian with the help of Fourier transform:

$$\hat{\psi}_{\mathbf{x}} = \frac{1}{\sqrt{V}}\hat{\psi}_{\mathbf{k}}e^{i\mathbf{k}\cdot\mathbf{x}}, \qquad h_{\mathbf{k}} = \sum_i \alpha_i \sin k_i + M\gamma_0, \tag{5.28}$$

where lattice momentum $\mathbf{k}$ is defined in the Brillouin zone:

$$k_i = \frac{2\pi}{aL_i} q_i, \qquad 0 \leq q_i < L_i, \qquad q_i \in \mathbb{Z}. \tag{5.29}$$

Then spectrum of excitations is easily found:

$$\varepsilon_{s,\sigma}(\mathbf{k}) = \frac{s}{a}\sqrt{\sum_i \sin^2(ak_i) + M^2}, \tag{5.30}$$

where $s = \pm 1$ labels particles and holes and $\sigma = \pm 1$ is chirality.

Now problem is clear: although in the limit of small momentum $|\mathbf{k}| \ll 1/a$ expression (5.30) correctly describes Dirac fermions $\varepsilon^2 = k^2 + M^2$, it also gives rise to $2^d - 1$ (where $d = 3$ is a spatial dimension) spurious flavors of fermions absent in the continuum theory when $k_i = \pm\pi/a$. These additional, unphysical degrees of freedom are called *fermion doublers*.

Moreover, despite the fact that Hamiltonian (5.27) with vanishing mass $M = 0$ manifestly obeys chiral symmetry $\left[\hat{H}_f, \hat{Q}_5\right] = 0$, where $\hat{Q}_5 = a^3 \sum_{\mathbf{x}} \hat{\psi}^\dagger_{\mathbf{x}} \gamma_5 \hat{\psi}_{\mathbf{x}}$ is operator of axial charge, the axial anomaly vanishes due to presence of doublers which generate equal contributions with opposite signs.

Neither presence of doublers nor absence of axial anomaly are desired features. This problem is a manifestation of a general theorem due to Nielsen and Ninomia: a lattice system with fermions can never have the following properties simultaneously:

1. Locality
2. Axial symmetry
3. Correct continuum limit, including axial anomaly (5.13) and absence of fermion doublers.

Therefore, there are two possible ways to achieve correct continuum limit: one can either break axial symmetry or employ non-local Hamiltonian.

5.3.2 Wilson-Dirac fermions

In order to remove doublers Wilson proposed to add so-called Wilson term to the naive Hamiltonian (5.27) which will make them infinitely heavy in the continuum limit:

$$h_W = \frac{r}{2}\gamma_0 \Delta_{\mathbf{xy}}, \tag{5.31}$$

where r is real-valued Wilson parameter and $\Delta_{\mathbf{xy}}$ is a lattice Laplacian:

$$\Delta_{\mathbf{xy}} = \frac{1}{a^2}\sum_{i=1}^{3}\left(2\,\delta_{\mathbf{xy}} - U_{\mathbf{x},i}\,\delta_{\mathbf{x}+\mathbf{i},\mathbf{y}} - U^\dagger_{\mathbf{x}-\mathbf{i},i}\,\delta_{\mathbf{x}-\mathbf{k},\mathbf{y}}\right). \tag{5.32}$$

Resulting Wilson-Dirac Hamiltonian reads as:

$$\hat{H}^{wd} = a^3 \sum_{\mathbf{xy}} \hat{\psi}^\dagger_{\mathbf{x}} h^{wd}_{\mathbf{xy}} \hat{\psi}_{\mathbf{y}}, \qquad h^{wd}_{\mathbf{xy}} = \sum_{i=1}^{3} -i\alpha_i \nabla_{i,\mathbf{xy}} + \frac{ar}{2}\gamma_0 \Delta_{\mathbf{xy}} + M\gamma_0 \delta_{\mathbf{xy}}. \quad (5.33)$$

Using Fourier transform one can find corresponding dispersion relation:

$$\varepsilon_{s,\sigma}(\mathbf{k}) = \frac{s}{a}\sqrt{\sum_i \sin^2(ak_i) + \Delta^2}, \qquad \Delta^2 = \frac{2r}{a}\sum_i \sin^2(ak_i/2) + M^2. \quad (5.34)$$

Thanks to the Wilson term, all doublers acquired momentum-dependent mass Δ which is infinitely large in the continuum limit, therefore they effectively decouple from the theory.

The price to pay is that Wilson-Dirac fermions explicitly break axial symmetry even in the massless case. Nevertheless, it is possible to show that since doublers are gone the axial anomaly is restored in the continuum limit precisely due to Wilson term:

$$\partial_t \hat{Q}_5 = \hat{\psi}^\dagger i\gamma_5 h_w \hat{\psi} \to -\frac{N_f}{2\pi^2}\mathbf{E}\cdot\mathbf{B}, \qquad \hat{Q}_5 = \hat{\psi}^\dagger \gamma_5 \hat{\psi}, \quad (5.35)$$

where we assume spatially uniform external fields for simplicity. In general case, $\hat{\psi}^\dagger i\gamma_5 h_w \hat{\psi} \to -\frac{N_f}{16\pi^2} F_{\mu\nu}\tilde{F}^{\mu\nu}$ and with suitable choice of lattice axial current j^μ_5 anomaly equation (5.13) is also recovered.

It is interesting to note that realization of axial anomaly is "reversed" for Wilson-Dirac fermions compared to continuum theory: on the finite lattice the number of fermion states is finite and fermion integration measure of the path integral is explicitly chiral invariant ($\mathrm{Tr}\,[\gamma_5] = 0$), whereas classical action breaks chiral symmetry in a particular way which is responsible for the anomaly.

5.3.3 Overlap fermions

Construction of Wilson-Dirac fermions is rather straightforward approach to the problem of lattice fermions which renders realization of chiral symmetry and axial anomaly obscured. Another perspective is to define lattice version of chiral symmetry in a way which will transparently preserve important features such as anomaly and absence of additive renormalization of the mass.

To this end, lattice fermions described by the Euclidean action $S = \int \mathrm{d}^4x\, \bar{\psi} D \psi$, where D is a four-dimensional Dirac operator, should satisfy fundamental Ginsparg-Wilson relation:

$$\{D, \gamma_5\} = aD\gamma_5 D. \quad (5.36)$$

In the continuum limit this equation reduces to $\{D, \gamma_5\} = 0$ which is equivalent to the requirement of chiral symmetry.

Using relation (5.36) one can define lattice axial transformations:

$$\psi \to e^{i\theta\gamma_5\left(1-\frac{a}{2}D\right)}, \qquad \bar{\psi} \to \bar{\psi}e^{i\theta\gamma_5\left(1-\frac{a}{2}D\right)}, \tag{5.37}$$

which leave the action $\bar{\psi}D\psi$ invariant and reduce to conventional axial symmetry (5.7) in the continuum limit. Right- and left-handed projections of fermions are constructed as follows:

$$\psi_\pm = \tilde{P}_\pm\psi, \qquad \bar{\psi}_\pm = \bar{\psi}P_\pm, \tag{5.38}$$

where modified projectors $\tilde{P}_\pm$ are:

$$\tilde{P}_\pm = \frac{1 \pm \tilde{\gamma}_5}{2}, \qquad \tilde{\gamma}_5 = \gamma_5\left(1 - aD\right). \tag{5.39}$$

Note that projectors $\tilde{P}_\pm$ satisfy requirement $\tilde{P}_\pm^2 = \tilde{P}_\pm$ due to Ginsparg-Wilson relation (5.36).

Within this approach, realization of axial symmetry on the lattice is in one-to-one correspondence to continuum theory. Indeed, on the language of chiral projections (5.38) lattice fermion action is decomposed into independent pieces describing chiral fermions independently. On the other hand, fermion measure of the lattice path integral explicitly generates theta-term analogous to (5.15):

$$\prod_{\mathbf{x}} \mathrm{d}\psi_{\mathbf{x}} \prod_{\mathbf{x}} \mathrm{d}\bar{\psi}_{\mathbf{x}} \to \prod_{\mathbf{x}} \mathrm{d}\psi_{\mathbf{x}} \prod_{\mathbf{x}} \mathrm{d}\bar{\psi}_{\mathbf{x}}\, e^{-S_\theta}, \quad \text{where} \quad S_\theta = ia\mathrm{Tr}\,\left[\theta\gamma_5 D\right]. \tag{5.40}$$

Eigenmodes of Dirac operator with non-zero eigenvalue do not contribute to S_θ, however since zero modes $D\psi_0 = 0$ have well-defined chirality $\gamma_5\psi_0 = \pm\psi_0$ due to Ginsparg-Wilson relation (5.36), their contribution to the theta-term directly lead to the lattice version of index theorem (5.19):

$$a\mathrm{Tr}\left[\gamma_5 D\right] = N_- - N_+, \tag{5.41}$$

where $N_\pm$ are numbers of right- and left-handed zero modes and $a\mathrm{Tr}\left[\gamma_5 D\right] \to Q_{CS}$ in the continuum limit.

A particular way to realize chiral fermions which satisfy the above requirements is to consider so-called *domain wall fermions*: in a five-dimensional space divided into domains where fermion mass has different sign in the direction of fifth dimension, chiral fermion modes emerge on the four-dimensional domain boundaries. These modes obey Ginsparg-Wilson relation and can be explicitly constructed in four dimensions with the help of Neuberger's *overlap fermions*.

In this work we are interested in Hamiltonian formulation rather than in the path integral representation. Overlap fermions and their properties within this approach have

been first considered in [143] and recently attracted attention in the context of real-time lattice simulations of anomalous transport phenomena. Let us write down overlap Hamiltonian:

$$\hat{H}^{ov} = \hat{\psi}^{\dagger} h^{ov} \hat{\psi}, \qquad h^{ov} = \gamma_0 D^{ov}, \qquad D^{ov} = 1 + \gamma_0 \frac{K}{\sqrt{K^{\dagger} K}}, \tag{5.42}$$

where indices are omitted for brevity and we put lattice spacing a to 1, D^{ov} is a spatial Dirac operator, $K = h^{wd} - \rho\gamma_0$ is overlap kernel, h^{wd} is Wilson-Dirac hamiltonian (5.33) and free parameter $\rho \in (0, 2]$ is domain wall height in the underlying five-dimensional theory of domain wall fermions.

In Hamiltonian approach Ginsparg-Wilson relation (5.36) and axial transformations (5.37) are written in terms of spatial Dirac operator D^{ov}. Operator of chiral charge can be defined as:

$$\hat{Q}_5 = \hat{\psi}^{\dagger} q_5 \hat{\psi}, \qquad q_5 = \gamma_5 \left(1 - \frac{1}{2} D^{ov}\right), \tag{5.43}$$

and it is straightforward to see that it commutes with overlap Hamiltonian: $\left[\hat{H}^{ov}, \hat{Q}_5\right] = 0$.

The use of overlap fermions in practical computations is only limited by their high numerical cost due to non-local structure of the Hamiltonian. However, their appealing chiral properties can easily overweight possible practical issues if the notion of exact chiral symmetry is crucial for the problem at hand.

5.4 Chirality pumping, Chiral Magnetic Wave and plasmon

In order to test performance of different lattice operators of chiral fermions we need some clear dynamical phenomenon related to the axial anomaly. Let us consider a neutral plasma of massless charged particles in the background of external magnetic field $\mathbf{B} = \mathbf{e}_3 B$ and a time-dependent electric field $\mathbf{E} = \mathbf{e}_3 E(t, x_3)$ parallel to $\mathbf{B}$ (here $\mathbf{e}_3$ is the unit basis vector along the x_3 coordinate axis). The axial charge and current q_A and $\mathbf{j}_A$ obey the real-time anomaly equation

$$\partial_t q_A(t, x_3) + \partial_3 j_{A3}(t, x_3) = \kappa \mathbf{E} \cdot \mathbf{B} = \kappa B E(t, x_3), \tag{5.44}$$

where $\kappa = 1/(2\pi^2)$ is the anomaly coefficient (we assume unit electric charge). If electromagnetic field is dynamical, the longitudinal electric field $E(t, x_3)$ satisfies the Maxwell equations

$$\partial_3 E(t, x_3) = q(t, x_3), \quad \partial_t E(t, x_3) = -j_3(t, x_3), \tag{5.45}$$

where $q\,(t, x_3)$ and $j_3\,(t, x_3)$ are the electric charge and current densities. In sufficiently strong magnetic fields $(3+1)$-dimensional Dirac fermions can be effectively described as $(1+1)$-dimensional Dirac fermions on the lowest Landau level. Higher Landau levels remain decoupled as long as all the relevant scales are significantly smaller than the energy of the next Landau level $E_1 = v_F\sqrt{2B}$, where v_F is the Fermi velocity. As a consequence of such dimensional reduction, longitudinal components of axial and electric currents are related to the electric and axial charge densities as

$$j_3(t, x_3) = v_F\, q_A(t, x_3), \quad j_{A\,3}(t, x_3) = v_F\, q(t, x_3). \tag{5.46}$$

Combining these equations with the Maxwell equations (5.45) and the anomaly equation (5.44), we arrive at the wave equation:

$$\partial_t^2 E(t, x_3) - v_F^2 \partial_3^2 E(t, x_3) + v_F\, \kappa B E(t, x_3) = 0, \tag{5.47}$$

which describes the Chiral Magnetic Wave (CMW) [144] of axial/vector charge density propagating along the magnetic field. If electromagnetic fields are dynamical, the mixing of CMW with plasmon leads to the dispersion relation with a finite gap ω_A:

$$\omega\,(k_3) = \pm\sqrt{v_F^2 k_3^2 + \omega_A^2}, \quad \omega_A = \sqrt{v_F \kappa B}. \tag{5.48}$$

Particularly instructive is the spatially homogeneous solution with $E\,(t=0) = E_0$ and $q_A\,(t=0) = q\,(t=0) = j_3\,(t=0) = j_{A\,3}\,(t=0) = 0$:

$$\begin{aligned} &E(t) = E_0 \cos(\omega_A t), \\ &q_A(t) = v_F^{-1} j_3(t) = \omega_A / v_F\, E_0 \sin(\omega_A t) = E_0 \sqrt{\kappa B} \sin\left(\sqrt{\kappa B} t\right). \end{aligned} \tag{5.49}$$

At $\omega_A t \ll 1$ this solution is close to the behavior of the axial charge density $q_A\,(t) = \kappa E_0 B\, t$ in the absence of backreaction of fermionic current on electromagnetic field. However, at later times the effect of backreaction turns the unbounded growth of axial charge density into periodic oscillations of amplitude $\omega_A E_0 = \sqrt{\kappa B} E_0$. It is interesting that the scaling of the axial charge density q_A with B changes from $q_A \sim B$ to $q_A \sim \sqrt{B}$. Simplicity of the solution (5.49) and apparent connection to anomaly makes it ideal candidate for testing real-time anomaly in lattice classical-statistical simulations with dynamical gauge fields.

5.5 Lattice chiral fermions within the classical-statistical field theory approximation

As described in detail in a number of papers [139, 142, 145, 146], classical-statistical approximation for gauge theories with fermions amounts to solving the quantum Heisenberg

equations for fermionic fields $\hat{\psi}_x$ in the background of the classical gauge vector potential $\mathbf{A}_x$, which in turn satisfies the Maxwell (or Yang-Mills) equations with the fermionic current term $\mathbf{j}_x$:

$$\partial_t \hat{\psi}_x = h\left[\mathbf{A}\right]_{xy} \hat{\psi}_y, \quad \mathbf{j}_x = \langle\, \hat{\psi}_y^\dagger \frac{\partial h\left[\mathbf{A}\right]_{yz}}{\partial \mathbf{A}_x} \hat{\psi}_z \,\rangle, \tag{5.50}$$

$$\partial_t \mathbf{A}_x = \mathbf{E}_x, \quad \partial_t \mathbf{E}_x = -\nabla \times \left(\nabla \times \mathbf{A}\right)_x - \mathbf{j}_x - \mathbf{j}_x^{ext}, \tag{5.51}$$

where $h_{xy}\left[\mathbf{A}\right]$ is the single-particle fermionic Hamiltonian and $\mathbf{j}_x^{ext}$ is the external current which creates the external electromagnetic fields $\mathbf{A}_x^{ext}$, $\mathbf{E}_x^{ext}$. The fermionic current $\mathbf{j}_x$ in the equation for $\mathbf{E}_x$ leads to the back-reaction of fermions on the electromagnetic fields, to which we refer as "backreaction" for the sake of brevity, i.e. "no backreaction" means that $\mathbf{j}_x$ was omitted from (5.51).

In the present study $h_{xy}\left[\mathbf{A}\right]$ is either the well-known Wilson-Dirac Hamiltonian (5.33) with zero mass or the overlap Hamiltonian (5.42), defined as

$$h^{ov} = \gamma_0 + \text{sign}\,\left(K\right), \quad K = h^{wd} - \rho\gamma_0, \tag{5.52}$$

where $0 < \rho < 2$, $\text{sign}\,\left(K\right)$ is the matrix sign function of the Hermitian kernel K and we have suppressed all matrix indexes and arguments for simplicity. In both cases $v_F = 1$. The matrix sign function $\text{sign}\,\left(K\right)$ can be defined, for example, in terms of the eigenstates $|\phi_n\rangle$ and eigenvalues λ_n of K as:

$$\text{sign}\,\left(K\right) = \sum_n \text{sign}\,\left(\lambda_n\right) |\phi_n\rangle\langle\phi_n| \,. \tag{5.53}$$

In order to calculate the derivative of the single-particle Hamiltonian over the gauge field $\frac{\partial h}{\partial \mathbf{A}_x}$, which enters the fermionic current, we use the expression analogous to the first-order perturbative correction in quantum mechanics:

$$\frac{\partial}{\partial \mathbf{A}_x} |\phi_n\rangle = \sum_{m \neq n} \frac{|\phi_m\rangle\langle\phi_m| \frac{\partial}{\partial \mathbf{A}_x} K |\phi_n\rangle}{\lambda_n - \lambda_m}. \tag{5.54}$$

Since the kernel K is expressed in terms of a local, sparse operator h^{wd}, the derivative $\frac{\partial}{\partial \mathbf{A}_x} K$ can be explicitly calculated. The expression for $\frac{\partial}{\partial \mathbf{A}_x} K$ involves also the contribution proportional to $\frac{\partial}{\partial \mathbf{A}_x} \text{sign}\,\left(\lambda_n\right)$ which only becomes nonzero when one of the eigenvalues λ_n crosses zero. However, in practice we never observed such crossings, and hence we neglected this term. We finally obtain

$$\frac{\partial h^{ov}}{\partial \mathbf{A}_x} = \sum_{n \neq m} \left(\frac{\text{sign}\,\left(\lambda_n\right) - \text{sign}\,\left(\lambda_m\right)}{\lambda_n - \lambda_m} \right) |\phi_n\rangle\langle\phi_n| \frac{\partial h^{wd}}{\partial \mathbf{A}_x} |\phi_m\rangle\langle\phi_m| \,. \tag{5.55}$$

In this exploratory study on small lattices, we have obtained the eigenstates $|\phi_n\rangle$ and the eigenvalues λ_n numerically using `LAPACK`, and calculated the current using the explicit expression (5.55). This brute force approach results in a V^4 scaling of the CPU

time, where V is the lattice volume, which has to be contrasted with the V^2 scaling for simulations with Wilson-Dirac Hamiltonian. Approximately half of CPU time is spent on the calculation of eigensystem of K using `LAPACK`, and another half is taken by the matrix-vector multiplications and summation over n and m in (5.55). In order to get rid of the V^4 scaling which becomes prohibitively expensive at large lattices, one could use e.g. the minmax polynomial approximation for the sign function, as is common in Monte-Carlo simulations with overlap fermions. Work in this direction is in progress.

5.6 Comparison of numerical results from Wilson-Dirac and overlap fermions

In this Section we compare the analytic solutions obtained in Section 5.4 with the results of classical-statistical simulations with Wilson-Dirac and overlap fermionic Hamiltonians h^{wd} and h^{ov} defined in the previous Section 5.5. We work on lattices of size $L \times L \times L$ with $L = 200$ for Wilson-Dirac fermions and $L = 25$ for overlap fermions with periodic boundary conditions for gauge fields and fermions, and introduce a constant magnetic field with flux $\Phi = L$ through the x_1x_2 plane, which corresponds to magnetic field strength $B = \frac{2\pi\Phi}{L^2}$. The reason for introducing magnetic flux which is a multiple of lattice size is that in this case the magnetic translation group [147] is equivalent to the group of lattice translations, and transnational invariance in the x_1x_2 plane is not broken by the magnetic field. Thus we can consistently assume that electromagnetic fields are homogeneous. The fermions are assumed to be initially in the equilibrium state at zero temperature and density. Also, one can use this symmetry in order diagonalize lattice Hamiltonian in the x_2 direction in the basis of plane waves $e^{ix_2p_2}$ and then to perform integration over p_2 analytically, so that the problem can be significantly simplified. This allowed us to speed up numerical calculations and go for lattice as large as $L = 200$ in the case of Wilson-Dirac fermions.

For Wilson-Dirac fermions, there is no unique definition of axial charge density, and we use the simplest one: $q_A^{wd} = \langle\, \hat{\psi}^\dagger \gamma_5 \hat{\psi}\, \rangle$. For overlap fermions, the conserved axial charge can be defined as [143]:

$$q_A^{ov} = \langle\, \hat{\psi}^\dagger \gamma_5 \left(1 - \gamma_0 h^{ov}/2\right) \hat{\psi}\, \rangle. \tag{5.56}$$

First, we consider the case of homogeneous and constant external electric field:

$$E^{ext}\,(t = 0) = E_0 \tag{5.57}$$

and disregard the effects of backreaction. On Fig. 5.1 we compare the time dependence of the axial charge density for Wilson-Dirac (red line) and overlap (blue line) fermions with the expected linear growth of the axial charge density $q_A = \kappa E_0 B\, t$ (dashed gray line).

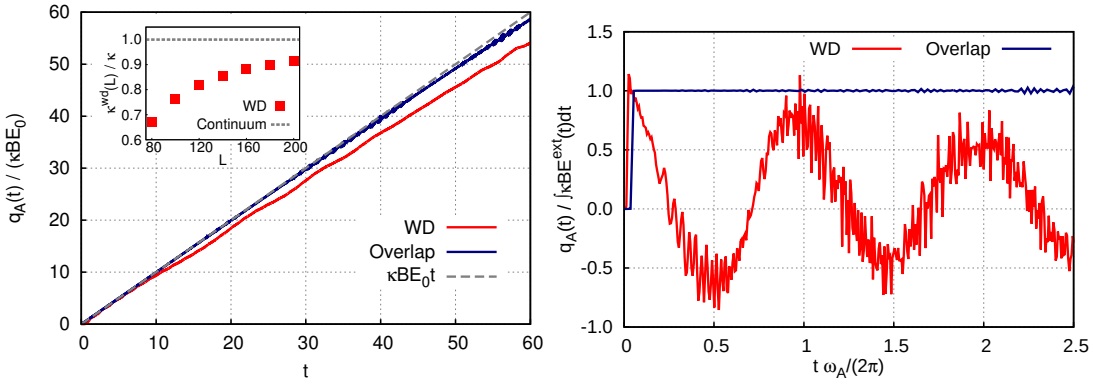

Figure 5.1: Time dependence of axial charge density in parallel external magnetic and electric field $E^{ext}(t) = E_0$ (on the left) and $E^{ext}(t) = E_0 \exp\left(-\frac{(t-t_0)^2}{2\tau^2}\right)$ with $t_0 = 2.5$ and $\tau\omega_A = 2 \cdot 10^{-2}$ (on the right) for Wilson-Dirac (red line) and overlap (blue line) fermions without backreaction, compared with the continuum anomaly result $q_A = \int^t \kappa B E^{ext}(t')dt'$. The inset on the left plot shows the lattice size dependence of the effective anomaly coefficient $\kappa^{wd}(L)$ for Wilson-Dirac fermions.

We see that while overlap fermions are simulated on the significantly smaller lattice, they still reproduce the continuum anomaly with a much better precision than Wilson-Dirac fermions. The inset of Fig. 5.1 shows the lattice size dependence of the effective anomaly coefficient $\kappa^{wd}(L)$ which relates $E_0 B t$ and $q_A(t)$ for Wilson-Dirac fermions. One can see that the approach to the continuum result is rather slow, so that even on the lattices as large as $200 \times 200 \times 200$ with magnetic field $B = \frac{2\pi}{L} = 0.0314$ lattice artifacts result in $\sim 10\%$ corrections to the anomaly.

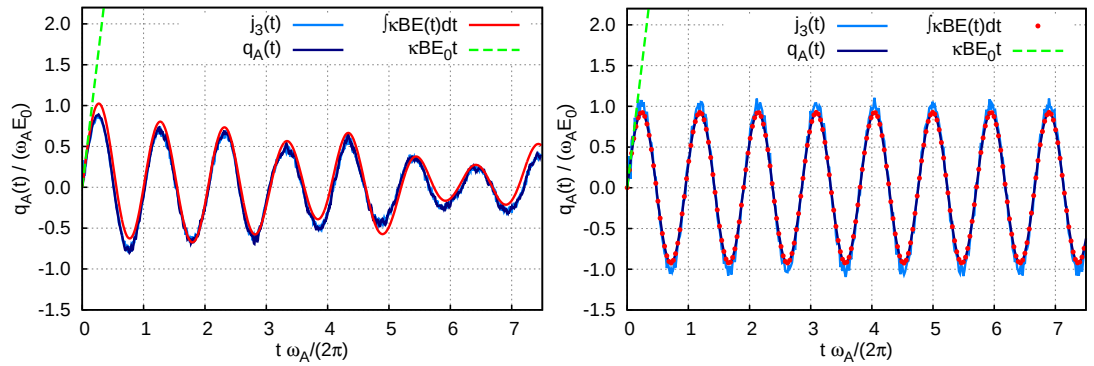

Figure 5.2: A comparison of axial charge density $q_A(t)$ (light blue line) and current density $j_3(t)$ (dark blue line) with the time-integrated gauge anomaly $\kappa \int_0^t d\tau \mathbf{E} \cdot \mathbf{B}$ (red line) in the presence of backreaction. On the left: for Wilson-Dirac fermions, on the right: for overlap fermions.

Next, we consider the effect of back-reaction of fermions on the gauge fields in the case when the external field E_0 is still constant in time. On Fig. 5.2 we compare the time dependence of the expectation values of the axial charge density and electric current for Wilson-Dirac (on the left) and overlap (on the right) fermions with the integral $\kappa \int_0^t d\tau \mathbf{E} \cdot \mathbf{B}$.

For both types of fermions we see the expected oscillations with the frequency ω_A. For Wilson-Dirac fermions these oscillations seem to slowly decay, showing interesting similarity with the results of holographic calculations of [148]. However, oscillations do not decay completely and start growing after some moment of time, suggesting that this could be an artifact of Wilson term.

For overlap fermions the fermionic and the gauge parts of the anomaly equation coincide with a very good precision (of order of 10^{-8}), but for Wilson fermions there is a visible difference. On the other hand, for Wilson-Dirac fermions the axial charge density and the electric current coincide with much better accuracy than for overlap fermions. This could be probably attributed to a much smaller lattice size for overlap fermions, and hence larger corrections due to distortions of higher Landau levels.

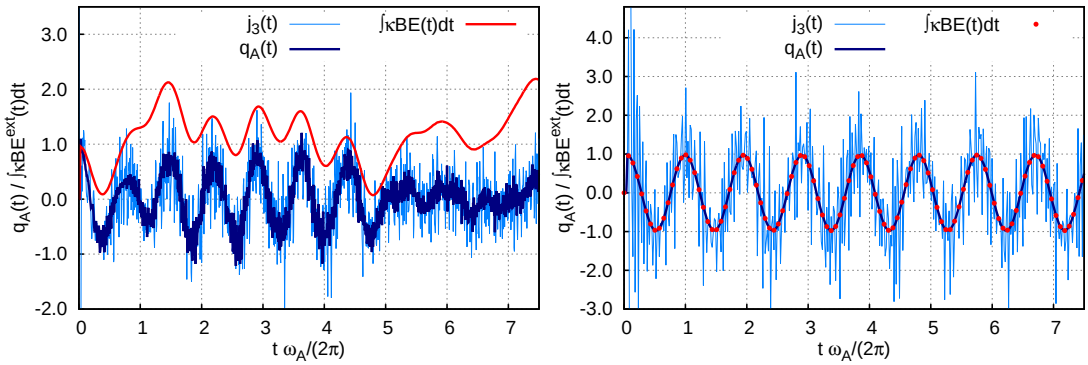

Figure 5.3: Time dependence of the axial charge density $q_A(t)$, electric current density $j_3(t)$ and the time-integrate gauge anomaly $\kappa \int dt BE(t)$ after a short pulse of external electric field for Wilson-Dirac (on the left) and overlap (on the right) fermions in the presence of backreaction.

Finally, we study the case of a short Gaussian-shaped pulse of external electric field:

$$E^{ext}(t) = E_0 \exp\left(-\frac{(t-t_0)^2}{2\tau^2}\right), \tag{5.58}$$

with $t_0 = 2.5$ and $\tau\omega_A = 2 \cdot 10^{-2} \ll 1$, where the role of higher Landau levels should be significant. If backreaction is disregarded, after the external electric field is switched off the axial charge of overlap fermions stays at a perfectly constant value consistent with the anomaly equation, as illustrated on the right plot on Fig. 5.1. Remembering the relation between the axial charge density and the electric current along the magnetic field, we can regard this situation as a real-time manifestation of the Chiral Magnetic Effect. Namely, with a short pulse of electric field parallel to magnetic field we have created nonzero axial charge in the system, and it results in non-dissipative electric current flowing along the magnetic field even when electric field becomes zero. However, this situation will be most likely unstable for sufficiently large volumes due to the chiral plasma instability phenomenon [57, 139] once we allow for fully 3D electromagnetic fields. In this case any small perturbation would result in quickly growing transverse helical electromagnetic fields and subsequent decrease of axial charge density and electric current.

In contrast, for the case of Wilson-Dirac fermions without backreaction the axial charge is not conserved at all after the same short pulse, as illustrated on the right plot of Fig. 5.1. Instead we observe nearly periodic, slightly decaying oscillations of axial charge density, with some irregular short-range fluctuations on top. These oscillations originate in explicit chiral symmetry breaking due to the Wilson term, which becomes significant for higher energy levels which are excited by the short pulse of electric field. The slow decay of $q_A(t)$ is similar to the one observed for constant external electric field with backreaction (left plot on Fig. 5.2), which again suggests that it might be an artifact of Wilson-Dirac fermions.

On Fig. 5.3 we illustrate the effect of backreaction on the time dependence of the chiral charge, electric current and the time-integrated gauge anomaly $\kappa \int dt BE(t)$ for Wilson-Dirac (on the left) and overlap (on the right) fermions subject to the same short pulse of external electric field. For overlap fermions we still observe regular oscillations with frequency ω_A. The fermionic and the gauge contributions to the anomaly equation agree very well, but electric current $j_3(t)$ exhibits significant short-range oscillations. The origin of this oscillations is again the dynamics associated with higher Landau levels. With Wilson-Dirac fermions, however, the gauge and the fermionic contributions to the anomaly disagree significantly already at early times, and are completely de-correlated at late times $t\omega_A/(2\pi) \gtrsim 6$. The electric current and the axial charge still agree quite well up to quite large short-scale fluctuations. By performing the Fourier transform of numerical data for $q_A(t)$ we have found that for Wilson-Dirac fermions we have a mixture of two oscillations with frequencies approximately equal to $0.6\omega_A$ and $1.5\omega_A$.

5.7 Conclusions

In this exploratory study we compared performance of overlap (for the first time) and Wilson-Dirac fermions in real-time classical-statistical field theory (CSFT) simulations. To this end, we considered both types of lattice fermions subjected to external magnetic field which was assumed larger than other relevant energy scales of the problem. We studied the behaviour of the axial charge and electric current in the direction of magnetic field. In the first scenario we considered so-called chirality pumping process when external electric field is applied parallel to magnetic field. In this scenario, only external electromagnetic fields were considered. We observed that in the case of overlap fermions the axial anomaly is reproduced with very high precision. In particular, in the absence of electric field the axial charge is conserved, as follows from anomaly equation. On the other hand, in the case of Wilson-Dirac fermions the anomaly equations is reproduced with worse precision even on larger lattices due to explicit breaking of chiral symmetry, so that axial charge is not conserved in the absence of electric field.

In the second scenario, we allowed electromagnetic fields to respond to induced

electric current in the system according to Maxwell equations (as follows from CSFT approximation). In this scenario, we observed generation of Chiral Magnetic Wave (CMW) propagating in the direction of magnetic field in the response to short pulse of external electric field. In the case when electric field was turned on sufficiently smoothly, for both types of fermions we observed oscillations corresponding to CMW on the frequency ω_A. Overlap fermions exhibited clear regular oscillations with a small distortion due to contribution of higher Landau levels. The anomaly equation is satisfied with very high precision. Wilson-Dirac fermions, however, showed interesting pattern of oscillation similarity to the results of holographic calculations from [148]. Even on large lattices, anomaly equation is satisfied with worse precision compared to overlap fermions. However, if initial pulse of electric field was very short, we observed complete break down of anomaly equation in the case Wilson-Dirac fermions due to lattice artifacts, whereas for overlap fermions it is still satisfied precisely.

Summarizing, we observed qualitatively better performance of overlap fermions in real-time CSFT simulations of chiral fermions even on smaller lattices compared to Wilson-Dirac fermions. It would be interesting to use exact chiral lattice fermions realized by overlap fermions in more realistic situations, for instance in simulations of Chiral Plasma Instability which was previously studied with the help of Wilson-Dirac fermions [139]. Another interesting case would be Chiral Magnetic Effect and Chiral Magnetic Wave in non-Abelian gauge theory. However, such problems require more involved numerical techniques since it is no longer possible to straightforwardly diagonalize dense matrix of overlap Hamiltonian due to its much bigger size. This is a subject of ongoing research project, results of which will be reported elsewhere.

Chapter 6

Conclusions

To summarize, the following results constitute the present Thesis:

1. In the Chapter 2 we found rich structure of complex saddle points of two-dimensional lattice gauge theory represented by Gross-Witten-Wadia unitary matrix model. We revealed novel interpretation of non-perturbative effects in the strong coupling phase in terms of manifestly complex saddle point. We checked that action and properties of these saddle points precisely matches predictions of the resurgence theory based on the analysis of asymptotic $1/N$ expansion [8]. In the weak coupling phase we found that multi-instanton configurations required by the resurgence theory are also manifestly complex, where eigenvalue tunnelling happens into the complex plane. However, one-instanton configuration is real.

   We confirmed that third-order phase transition in this model is driven by the instanton condensation [149]. We also discovered that properties of the spectrum of Gaussian fluctuations about saddle points significantly change across the phase transition. In particular, in the strong coupling phase an interesting zero mode emerges at $N = \infty$ and other low-lying modes become doubly degenerate. However, the upper edge of the spectrum remains non-degenerate. It is interesting to note, that the structure of complex saddle points seems to be reflected in the spectrum of Gaussian fluctuations about the vacuum: in the strong coupling regime, the fraction of degenerate low-lying modes approximately corresponds to the fraction of complex saddle points described by three-cut solutions, whereas all other saddle points are described by two-cut solutions. As system goes into weakly coupled regime, zero mode and degeneracy are lifted. At the same time, three-cut saddle points completely disappear. This intriguing observation, to our humble opinion, deserves some investigation.

   It would be very interesting to find some interpretation of our complex saddle points directly in the continuum two-dimensional gauge theory, where the phase transition happens with respect to the manifold area A [66, 67]. Our hope is to

find transparent and clear description of physics of this model in both phases in terms of some generalized class of non-perturbative objects, just like in the case of complex saddle points in two dimensional lattice gauge theory. This could be an important step towards explicit construction of uniform resurgent approximations in continuum and lattice theories [60, 150]. We leave this question for a future investigation.

2. In the Chapter 3 we studied adiabatic continuity conjecture and phase structure of the two-dimensional Principal Chiral Model (PCM) with respect to the size L of compact spatial direction. We considered two types of boundary conditions on that direction: periodic and with $\mathbb{Z}^N$-preserving twist [15, 31, 81]. In the absence of well-defined local order parameters such as e.g. Polyakov loop, we considered universal physical observables which can characterize phase transitions regardless of the symmetries of the system: mean energy, specific heat and static correlation length. We found that for both types of boundary conditions these quantities behave in a way which is compatible with a rather weak crossover or $N = \infty$ phase transition: mean energy and specific heat exhibit monotonic growth/decrease with L once it is sufficiently small, and the static correlation length is enhanced near some "critical" length.

   We found important differences between two types of boundary conditions. For periodic boundary conditions the peak in the correlation length becomes somewhat higher and narrower as the rank N is increased. It also becomes slightly higher for larger lattice volumes. This behavior might suggest that PCM with periodic boundary conditions might indeed feature a finite-temperature phase transition at $N = \infty$. In contrast, for twisted boundary conditions the shape of the peak in the static correlation length is independent of N, once the data is considered as a function of the combined length parameter $\rho = NL$. This behaviour is not typical for the scenario of $N = \infty$ phase transition, but can be still compatible with a weak crossover. If true, the crossover scenario would be a challenge for the adiabatic continuity conjecture, since the phases separated by the crossover typically cannot be analytically related to each other (recall classical example of the Berezinskii–Kosterlitz–Thouless transition).

   With the help of Gradient Flow, we also studied the structure of dominant non-perturbative saddle points of the path integral of the PCM, for both types of boundary conditions. We found numerical evidence for unitons, the unstable saddle points of the continuum PCM. In particular, we observed quantized action which scales linearly with N as expected for uniton. Non-perturbative saddle points become effectively stable in the case of twisted boundary conditions, thus exhibiting the phenomenon of emergent topology [15]. We also find that for twisted

boundary conditions the geometric properties of non-perturbative saddles change precisely at the position of the aforementioned crossover, which is yet another argument that this crossover might be non-trivial.

Summarizing, PCM appeared a difficult theory for lattice study, primarily due to absence of any clear order parameter. However, our observations suggest that physics of adiabatic continuity and $\mathbb{Z}^N$-preserving twist in matrix QCD-like theories is more complicated than we could have expected. We plan to extend the present work and investigate continuum limit, as well as structure of observed saddle points. In particular, we plan to study spectrum of Gaussian fluctuations about such saddles since it should be possible, in principle, to clearly identify effectively stable fractons as constituents of unstable unitons in the compactified regime. We are also highly intrigued by recent applications of adiabatic continuity to Yang-Mills theory and QCD [32, 33].

3. In the Chapter 4 we preformed the Lefschetz thimble analysis of the sign problem in the two-dimensional Hubbard model. We combined analytic analysis on small lattices consisting of few sites with Monte-Carlo simulations on bigger lattices. We considered two possible representations of the interaction term based on the Gaussian Hubbard-Stratonovich (HS) transformation. These two possibilities can be unified if one consider two auxiliary boson fields instead of one, where their mixture can be parameterized by $\alpha \in [0, 1]$. We have found that in this representation the complexity of the sign problem increases with the spatial size of lattice. On the contrary, the continuous limit $N_t \to \infty$, where N_t is the size of Euclidean time direction, makes the sign problem milder by lifting the non-uniform saddle points and decreasing their contribution in the overall sum over thimbles. For $\alpha = 0$ fermionic determinant exhibits much milder sign problem compared to $\alpha = 1$ case due to finite number of relevant thimbles and much smaller fluctuations of their phases. However, the minimal number of relevant thimbles is observed for some intermediate value $\alpha \approx 0.9$. In this case, there are two relevant thimbles for all studied few-site lattices. Monte-Carlo simulations indicate that this regime is also advantageous for larger lattices. We also find that "domain walls" on the real integration plane formed by zeros of fermionic determinant at $\alpha = 0$ and $\alpha = 1$ are absent at $\alpha \approx 0.9$, so that ergodicity problem become milder for Monte-Carlo simulations on the thimbles.

   We have also studied a novel representation with substantially reduced number of relevant thimbles. Calculations at finite chemical potential show that saddle points from real domain move into complex domain while preserving the action real. It implies that at small values of chemical potential the complexity of the sign problem in this case is comparable to $\alpha = 0$ Gaussian Hubbard-Stratonovich

transformation. Additionally, in new representation one can define topological invariant which can distinguish relevant saddle points from the irrelevant ones, at least in the simplest case of one-site Hubbard model. We would like to extend our work towards larger lattices and physically interesting regimes in the near future.

4. In the Chapter 5 we performed exploratory study of overlap fermions, which realize exact lattice version of chiral symmetry, and Wilson-Dirac fermions in real-time classical-statistical field theory (CSFT) simulations. We considered both types of fermions subjected to external magnetic field which was assumed larger than other relevant energy scales of the problem. We studied realization of axial anomaly and real-time anomalous transport phenomena. In the first scenario, we considered so-called chirality pumping process when external electric field is applied parallel to magnetic field, so that axial charge grows due to anomaly. In the second scenario, we studied Chiral Magnetic Wave (mixed with plasmon) excited by short pulse of external electric field parallel to magnetic field.

   In both cases, we observed qualitatively better performance of overlap fermions in real-time CSFT simulations compared to Wilson-Dirac fermions. In particular, we found that equation for axial anomaly is satisfied with very high precision for overlap fermions at all considered conditions, whereas for Wilson-Dirac it might completely break down at certain circumstances due to lattice artifacts. Thus, it would be interesting to use exact chiral lattice fermions realized by overlap fermions in more realistic situations, for instance in simulations of Chiral Plasma Instability which was previously studied with the help of Wilson-Dirac fermions [139]. Another interesting case would be non-Abelian gauge theory in strong magnetic field where instanton/sphaleron transitions between topological sectors can induce local fluctuations of axial charges and therefore cause Chiral Magnetic Effect and Chiral Magnetic Wave [142, 151]. However, such problems require more involved numerical techniques compared to rather straightforward approach of the present work. This is a subject of ongoing research project, results of which will be reported elsewhere.

Part I

Appendix

Appendix A

Details of numerical study of two-dimensional lattice gauge theory

A.1 Halley method

Halley method [152] is a numerical iterative procedure for finding roots of a system of holomorphic equations:

$$F_i[z] = 0, \qquad i = 1 \dots n, \tag{A.1}$$

where z is n-dimensional complex-valued vector. This method is the next-order improvement of well-known Newton iterations. At the initial step $k = 0$ one chooses some initial guess $z^{(0)}$ for the root. At the following steps $k = 1, \dots$ the guess is refined according to the formula:

$$z_i^{(k+1)} = z_i^{(k)} - 2\left(2J_{ij}\left[z^{(k)}\right] - H_{ijl}\left[z^{(k)}\right] J^{-1}_{lm}\left[z^{(k)}\right] F_m\left[z^{(k)}\right]\right)^{-1} F_j\left[z^{(k)}\right], \tag{A.2}$$

where we have defined:

$$J_{ij}[z_l] = \frac{\partial F_i[z_l]}{\partial z_j}, \quad H_{ijk}[z_l] = \frac{\partial^2 F_i[z_l]}{\partial z_j \partial z_k}. \tag{A.3}$$

Under certain conditions [152] Halley iterations $z^{(k)}$ converge to some root of the system (A.1). In practice, each iteration can be implemented as follows:

1. Solve $J_{ij}\left[z^{(k)}\right] u_j = F_i\left[z^{(k)}\right]$ for u_i,
2. Solve $\left(J_{ij}\left[z^{(k)}\right] - \frac{1}{2} H_{ijk}\left[z^{(k)}\right] u_k\right) v_j = H_{ijk}\left[z^{(k)}\right] u_j u_k$ for v_i,
3. Finally, $z_i^{(k+1)} = z_i^{(k)} - u_i - v_i/2$.

We note that it is not necessary to store the whole tensor H_{ijk} in computer memory since only its contractions with the vectors u and v are needed. Algorithm stops when the stopping criteria is met:

$$||z^{(k+1)} - z^{(k)}|| < \epsilon, \tag{A.4}$$

where ϵ is a given precision. In addition to this, one can test whether equation (A.1) is satisfied within given precision.

Halley method is advantageous compared to Newton method since it offers better convergence and it is stable in the vicinity of points where Jacobi matrix $J_{ij}[z]$ becomes non-invertible. In practical computations, the latter circumstance helps to find good approximations to roots which cannot be found by Newton algorithm, however at the price of considerable slow down.

Bibliography

[1] D. J. Gross and F. Wilczek. "Ultraviolet Behavior of Non-Abelian Gauge Theories". *Phys. Rev. Lett.* 30.26 (1973), 1343–1346.

[2] H. D. Politzer. "Reliable Perturbative Results for Strong Interactions?" *Phys. Rev. Lett.* 30.26 (1973), 1346–1349.

[3] G. Veneziano. *Nuovo Cimento* 57A (1968), 190.

[4] Z. Koba and H. B. Nielsen. "Reaction amplitude for n-mesons a generalization of the Veneziano-Bardakci-Ruegg-Virasoro model". *Nucl. Phys. B* 10 (1969), 633–655.

[5] Edward Shuryak. "Physics of strongly coupled quark–gluon plasma". *Prog. Part. Nucl. Phys.* 62 (2009), 48–101.

[6] Edward Shuryak. "Physics of strongly coupled quark–gluon plasma". *Rev. Mod. Phys.* 89 (2017), 035001.

[7] M. Mariño, R. Schiappa, and M. Weiss. "Nonperturbative effects and the large-order behavior of matrix models and topological strings". *Comm.Num.Theor.Phys.* 2 (2008), 349–419. arXiv: 0711.1954.

[8] M. Mariño. "Nonperturbative effects and nonperturbative definitions in matrix models and topological strings". *JHEP* 0812 (2008), 114. arXiv: 0805.3033.

[9] S. Pasquetti and R. Schiappa. "Borel and Stokes Nonperturbative Phenomena in Topological String Theory and $c = 1$ Matrix Models". *Annales Henri Poincare* 11 (2010), 351–431. arXiv: 0907.4082.

[10] S. Garoufalidis et al. "Asymptotics of the instantons of Painleve I". *Int.Math.Res.Not.* 2012 (2012), 561–606. arXiv: 1002.3634.

[11] I. Aniceto, R. Schiappa, and M. Vonk. "The Resurgence of Instantons in String Theory". *Comm.Num.Theor.Phys.* 6 (2012), 339–496. arXiv: 1106.5922.

[12] R. Couso-Santamaría, R. Schiappa, and R. Vaz. "Finite N from Resurgent Large N". *Ann.Phys.* 356 (2015), 1–28. arXiv: 1501.01007.

[13] P. C. Argyres and M. Unsal. "The semi-classical expansion and resurgence in gauge theories: new perturbative, instanton, bion, and renormalon effects". *JHEP* 08 (2012), 063. arXiv: 1206.1890.

[14] G. V. Dunne and M. Unsal. "Resurgence and Trans-series in Quantum Field Theory: The CP(N-1) Model". *JHEP* 1211 (2012), 170. arXiv: 1210.2423.

[15] A. Cherman et al. "Resurgence in QFT: Unitons, Fractons and Renormalons in the Principal Chiral Model". *Phys. Rev. Lett.* 112 (2014), 021601. arXiv: 1308.0127.

[16] G. V. Dunne and M. Unsal. "Resurgence and Dynamics of O(N) and Grassmannian Sigma Models". *JHEP* 1509 (2015), 199. arXiv: 1505.07803.

[17] I. Aniceto, J. G. Russo, and R. Schiappa. "Resurgent Analysis of Localizable Observables in Supersymmetric Gauge Theories". *JHEP* 1503 (2015), 172. arXiv: 1410.5834.

[18] E. Witten. "Analytic continuation of Chern-Simons theory". *Stud.Adv.Math.* 50 (2011), 347–446. arXiv: 1001.2933.

[19] E. Witten. "A New Look At The Path Integral Of Quantum Mechanics" (2010). arXiv: arXiv:1009.6032.

[20] G. t'Hooft. *The Whys of subnuclear physics, Proc. Int. School*. Plenum, New York, 1977.

[21] G. Parisi. "Singularities of the Borel transform in renormalizable theories". *Phys. Lett. B* 76 (1 1978), 65.

[22] G. Parisi. "On infrared divergences". *Nucl. Phys. B* 150 (C 1979), 163.

[23] F. David. "On the ambiguity of composite operators, IR renormalons and the status of the operator product expansion". *Nucl. Phys. B* 234 (1 1984), 237.

[24] F. David. "The operator product expansion and renormalons: A comment". *Nucl. Phys. B* 263 (3-4 1986), 637.

[25] A.H. Mueller. "On the structure of infrared renormalons in physical processes at high energies". *Nucl. Phys. B* 250 (1-4 1985), 327.

[26] M. Beneke and Vladimir M. Braun. "Heavy quark effective theory beyond perturbation theory: Renormalons, the pole mass and the residual mass term". *Nucl.Phys. B* 426 (1994), 301–343. arXiv: hep-ph/9402364.

[27] M. Beneke and Vladimir M. Braun. "Naive nonAbelianization and resummation of fermion bubble chains". *Phys.Lett. B* 348 (1995), 513–520. arXiv: hep-ph/9411229.

[28] Patricia Ball, M. Beneke, and Vladimir M. Braun. "Naive nonAbelianization and resummation of fermion bubble chains". *Nucl.Phys. B* 452 (1995), 563–625. arXiv: hep-ph/9502300.

[29] M. Beneke. "Renormalons". *Physics Reports* 317.1 (1999), 1–142.

[30] G. V. Dunne and M. Unsal. "Continuity and Resurgence: towards a continuum definition of the CP(N-1) model". *Phys. Rev. D* 87 (2013), 025015. arXiv: 1210.3646.

[31] Aleksey Cherman, Daniele Dorigoni, and Mithat Unsal. "Decoding perturbation theory using resurgence: Stokes phenomena, new saddle points and Lefschetz thimbles". *JHEP* 1510 (2015), 094. DOI: 10.1007/JHEP10(2015)056. arXiv: 1403.1277.

[32] Kyle Aitken, Aleksey Cherman ad Erich Poppitz, and Laurence G. Yaffe. "QCD on a small circle". *Phys. Rev. D* 96 (2017), 096022. arXiv: 1707.08971.

[33] Kyle Aitken, Aleksey Cherman, and Mithat Ünsal. "Vacuum structure of Yang-Mills theory as a function of θ". *JHEP* 09 (2018), 030. arXiv: 1804.06848.

[34] Philippe de Forcrand. "Simulating QCD at finite density". *Pos Lat.* 010 (2009). arXiv: 1005.0539.

[35] C. Gattringer and K. Langfeld. "Approaches to the sign problem in lattice field theory". *Int.J.Mod.Phys.A* 31 (2016), 1643007. arXiv: 1603.09517.

[36] J. Hubbard. "Electron Correlations in Narrow Energy Bands". *Proc. R. Soc. A* 276.1365 (1963), 238–257. DOI: 10.1098/rspa.1963.0204.

[37] J. Hubbard. "Electron Correlations in Narrow Energy Bands. III. An Improved Solution". *Proc. R. Soc. A* 281.1386 (1964), 401–419. DOI: 10.1098/rspa.1964.0190.

[38] Patrick A. Lee, Naoto Nagaosa, and Xiao-Gang Wen. "Doping a mott insulator: Physics of high-temperature superconductivity". *Rev. Mod. Phys.* 78 (Jan. 2006), 17–85.

[39] N. P. Armitage, P. Fournier, and R. L. Greene. "Progress and perspectives on electron-doped cuprates". *Rev. Mod. Phys.* 82 (Sept. 2010), 2421–2487.

[40] D. Bgeriswyl et al. *The Hubbard Model*. Nato Science Series B. Springer, 1995.

[41] S. L. Adler. "Axial-Vector Vertex in Spinor Electrodynamics". *Phys. Rev.* 177 (1969), 2426–2438.

[42] J.S. Bell and R. Jackiw. "A PCAC puzzle: $\pi^0 \to \gamma\gamma$ in the σ-model". *Il Nuovo Cimento A* 60 (1969), 47–61.

[43] Stephen L. Adler and William A. Bardeen. “Absence of Higher-Order Corrections in the Anomalous Axial-Vector Divergence Equation”. *Phys. Rev.* 182 (1969), 1517.

[44] D. Kharzeev and A. Zhitnitsky. “Charge separation induced by P-odd bubbles in QCD matter”. *Nucl.Phys.A* 797 (2007), 67–79. arXiv: 0706.1026.

[45] K. Fukushima, D. E. Kharzeev, and H. J. Warringa. “The Chiral Magnetic Effect”. *Phys. Rev. D* 78 (2008), 074033. arXiv: 0808.3382.

[46] L. Adamczyk (STAR Collaboration). “Beam-energy dependence of charge separation along the magnetic field in Au+Au collisions at RHIC”. *Phys. Rev. Lett.* 113 (2014), 052302. arXiv: 1404.1433.

[47] G. Basar, D. E. Kharzeev, and H. U. Yee. “Triangle anomaly in Weyl semi-metals”. *Phys. Rev. B* 89 (2014), 035142. arXiv: 1305.6338.

[48] H. J. Kim et al. “Dirac vs. Weyl in topological insulators: Adler-Bell-Jackiw anomaly in transport phenomena”. *Phys. Rev. Lett.* 111 (2013), 246603. arXiv: 1307.6990.

[49] Q. Li et al. “Chiral magnetic effect in ZrTe5”. *Nature Phys.* 12 (2016), 550–554. arXiv: 1412.6543.

[50] A. Vilenkin. “Equilibrium parity-violating current in a magnetic field”. *Phys. Rev. D* 22 (1980), 3080–3084.

[51] D. T. Son and A. R. Zhitnitsky. “Quantum Anomalies in Dense Matter”. *Phys. Rev. D* 70 (2004), 074018. arXiv: hep-ph/0405216.

[52] M. A. Metlitski and A. R. Zhitnitsky. “Anomalous Axion Interactions and Topological Currents in Dense Matter”. *Phys. Rev. D* 72 (2005), 045011. arXiv: hep-ph/0505072.

[53] H. Tashiro, T. Vachaspati, and A. Vilenkin. “Chiral Effects and Cosmic Magnetic Fields”. *Phys. Rev. D* 86 (2012), 105033. arXiv: 1206.5549.

[54] G. Sigl and N. Leite. “Chiral Magnetic Effect in Protoneutron Stars and Magnetic Field Spectral Evolution”. *J.Cosmol.Astropart.Phys.* 01 (2016), 025. arXiv: 1507.04983.

[55] V. Skokov, A. Illarionov, and V. Toneev. “Estimate of the magnetic field strength in heavy-ion collisions”. *Int. J. Mod. Phys. A* 24 (2009), 5925. arXiv: 0907.1396.

[56] N. Yamamoto. *Generalized Bloch Theorem and Chiral Transport Phenomena*. 2015. arXiv: 1502.01547.

[57] Y. Akamatsu and N. Yamamoto. “Chiral Plasma Instabilities”. *Phys. Rev. Lett.* 111 (2013), 052002. arXiv: 1302.2125.

[58] P. Romatschke. “Do nuclear collisions create a locally equilibrated quarkgluon plasma?” *Eur. Phys. J. C* 77 (2017), 21. arXiv: 0907.1396.

[59] M. Marino. *Instantons and Large N: An Introduction to Non-Perturbative Methods in Quantum Field Theory*. Cambridge University Press, 2015. ISBN: 1107068525.

[60] G. Basar and G. V. Dunne. “Resurgence and the Nekrasov-Shatashvili Limit: Connecting Weak and Strong Coupling in the Mathieu and Lam’e Systems”. *JHEP* 1502 (2015), 160. arXiv: 1501.05671.

[61] P. de Forcrand et al. “The lattice QCD phase diagram in and away from the strong coupling limit”. *Phys. Rev. Lett.* 113 (2014), 152002. arXiv: 1406.4397.

[62] D. J. Gross and E. Witten. “Possible third-order phase transition in the large-N lattice gauge theory”. *Phys. Rev. D* 21 (1980), 446–453. URL: http://link.aps.org/doi/10.1103/PhysRevD.21.446.

[63] S. R. Wadia. *A Study of U(N) Lattice Gauge Theory in 2-dimensions*. 1979. arXiv: 1212.2906.

[64] S. R. Wadia. “$N = \infty$ phase transition in a class of exactly soluble model lattice gauge theories”. *Phys. Lett. B* 93 (1980), 403–410. URL: http://dx.doi.org/10.1016/0370-2693(80)90353-6.

[65] H. Neuberger. “Non-perturbative contributions in models with a non-analytic behavior at infinite N”. *Nucl. Phys. B* 179 (1981), 253–282. URL: http://dx.doi.org/10.1016/0550-3213(81)90238-8.

[66] M. R. Douglas and V. A. Kazakov. “Large N Phase Transition in Continuum QCD_2”. *Phys. Lett. B* 319 (1993), 219. arXiv: hep-th/9305047.

[67] D. J. Gross and A. Matytsin. “Instanton Induced Large N Phase Transitions in Two and Four Dimensional QCD”. *Nucl. Phys. B* 429 (1994), 50–74. arXiv: hep-th/9404004.

[68] H. Neuberger. “Instantons as a bridgehead at $N = \infty$”. *Phys. Lett. B* 94 (1980), 199–202. URL: http://dx.doi.org/10.1016/0370-2693(80)90858-8.

[69] A. Behtash et al. “Hidden topological angles in path integrals”. *Phys. Rev. Lett.* 115 (2015), 041601. arXiv: 1502.06624.

[70] Ya. Goldschmidt. “1/N expansion in two-dimensional lattice gauge theory”. *J.Math.Phys.* 21 (1980), 1842. URL: http://scitation.aip.org/content/aip/journal/jmp/21/7/10.1063/1.524600.

[71] I. Aniceto and R. Schiappa. “Nonperturbative Ambiguities and the Reality of Resurgent Transseries”. *Commun.Math.Phys.* 335 (2015), 183–245. arXiv: 1308.1115.

[72] T. Eguchi and H. Kawai. “Reduction of dynamical degrees of freedom in the large-N gauge theory”. *Phys. Rev. Lett.* 48.16 (1982), 1063–1066. URL: http://link.aps.org/doi/10.1103/PhysRevLett.48.1063.

[73] A. Gonzalez-Arroyo and M. Okawa. “A twisted model for large N lattice gauge theory”. *Phys. Lett. B* 120 (1983), 174–178. URL: http://dx.doi.org/10.1016/0370-2693(83)90647-0.

[74] A. Gonzalez-Arroyo and M. Okawa. “Large N reduction reduction with the twisted Eguchi-Kawai model”. *JHEP* 07 (2010), 043. arXiv: 1005.1981.

[75] G. Bhanot, U. M. Heller, and H. Neuberger. “The quenched Eguchi-Kawai model”. *Phys. Lett. B* 113 (1982), 47–50. URL: http://dx.doi.org/10.1016/0370-2693(82)90106-X.

[76] R. Narayanan and H. Neuberger. “Large N reduction in the continuum three dimensional Yang-Mills theory”. *Phys.Rev.Lett.* 91 (2003), 081601. DOI: 10.1103/PhysRevLett.91.081601. arXiv: hep-lat/0303023.

[77] J. Kiskis, R. Narayanan, and H. Neuberger. “Does the crossover from perturbative to nonperturbative physics in QCD become a phase transition at infinite N?” *Phys.Lett.B* 574 (2003), 65–74. DOI: 10.1016/j.physletb.2003.08.070. arXiv: hep-lat/0308033.

[78] Tatsuo Azeyanagi et al. “Phase structure of twisted Eguchi-Kawai model”. *JHEP* 0801 (2008), 025. arXiv: 0711.1925.

[79] M. Unsal and L. G. Yaffe. “Center-stabilized Yang-Mills theory: confinement and large N volume independence”. *Phys. Rev. D* 78 (2008), 065035. arXiv: 0803.0344. URL: https://doi.org/10.1103/PhysRevD.78.065035.

[80] P. Kovtun, M. Unsal, and L. G. Yaffe. “Volume independence in large Nc QCD-like gauge theories”. *JHEP* 0706 (2007), 019. arXiv: hep-th/0702021. URL: https://doi.org/10.1088/1126-6708/2007/06/019.

[81] Tin Sulejmanpasic. “Global symmetries, volume independence and continuity”. *Phys.Rev.Lett.* 118 (2017), 011601. DOI: 10.1103/PhysRevLett.118.011601. arXiv: 1610.04009.

[82] P. Orland. “Summing Planar Diagrams by an Integrable Bootstrap”. *Phys. Rev. D* 84 (2011), 105005. arXiv: 1108.0058.

[83] P. Orland. “Summing Planar Diagrams by an Integrable Bootstrap II”. *Phys. Rev. D* 86 (2012), 045023. arXiv: 1205.1763.

[84] A. C. Cubero and P. Orland. “Correlation Functions of the SU(infinity) Principal Chiral Model”. *Phys. Rev. D* 88 (2013), 025044. arXiv: 1306.1930.

[85] P. Orland. “Seeing asymptotic freedom in an exact correlator of a large-N matrix field theory”. *Phys. Rev. D* 90 (2014), 125038. arXiv: 1410.2627.

[86] E. Katzav and P. Orland. “The universal coefficient of the exact correlator of a large-N matrix field theory”. *Phys. Rev. D* 94 (2016), 065041. arXiv: 1608.00262.

[87] A. C. Cubero. “Nontrivial Thermodynamics in ’t Hooft’s Large-N Limit”. *Phys. Rev. D* 91 (2015), 105025. arXiv: 1503.06139.

[88] Martin Lüscher. “Properties and uses of the Wilson Flow in lattice QCD”. *JHEP* 1008 (2010), 071. DOI: 10.1007/JHEP08(2010)071. arXiv: 1006.4518.

[89] N. Cabibbo and E. Marinari. “A new method for updating SU(N) matrices in computer simulations of gauge theories”. *Phys. Lett. B* 119 (1982), 387–390. URL: http://dx.doi.org/10.1016/0370-2693(82)90696-7.

[90] S. L. Adler. “Over-relaxation method for the Monte Carlo evaluation of the partition function for multiquadratic actions”. *Phys. Rev. D* 23 (1981), 2901. URL: https://doi.org/10.1103/PhysRevD.23.2901.

[91] P. Rossi and E. Vicari. “Two dimensional SU(N)xSU(N) Chiral Models on the Lattice (II): the Green’s Function”. *Phys. Rev. D* 49 (1994), 6072. arXiv: hep-lat/9401029.

[92] P. Rossi and E. Vicari. “Two dimensional SU(N) x SU(N) chiral models on the lattice”. *Phys. Rev. D* 49 (1994), 1621. arXiv: hep-lat/9307014.

[93] M. Campostrini, P. Rossi, and E. Vicari. “Large-N phase transition in lattice 2-d principal chiral models”. *Phys. Rev. D* 52 (1995), 395. arXiv: hep-lat/9412102.

[94] P. V. Buividovich and A. Davody. *Diagrammatic Monte-Carlo for weak-coupling expansion of non-Abelian lattice field theories: large-N $U(N) \times U(N)$ principal chiral model*. Accepted to Phys.Rev.D. 2017. arXiv: 1705.03368.

[95] B. Lucini, M. Teper, and U. Wenger. “Properties of the deconfining phase transition in SU(N) gauge theories”. *JHEP* 0502 (2005), 033. arXiv: hep-lat/0502003. URL: http://dx.doi.org/10.1088/1126-6708/2005/02/033.

[96] G. Bhanot et al. “First-order transitions and the multihistogram method”. *Nucl. Phys. B* 378 (1992), 633–651. URL: http://dx.doi.org/10.1016/0550-3213(92)90611-E.

[97] M. Unsal. “Quantum phase transitions and new scales in QCD-like theories”. *Phys. Rev. Lett.* 102 (2009), 182002. arXiv: 0807.0466. URL: http://dx.doi.org/10.1103/PhysRevLett.102.182002.

[98] Karen Uhlenbeck. “Harmonic maps into Lie groups: classical solutions of the chiral model”. *J. Differential Geom.* 30.1 (1989), 1–50.

[99] Wieland Brendel et al. “Instanton constituents and fermionic zero modes in twisted CP(N) models”. *Phys.Lett.B* 676 (2009), 116–125. DOI: 10.1016/j.physletb.2009.04.055. arXiv: 0902.2328.

[100] E.M. Ilgenfritz, M. Müller-Preussker, and D. Peschka. “Calorons in SU(3) lattice gauge theory”. *Phys.Rev.D* 71 (2005), 116003. arXiv: hep-lat/0503020.

[101] M. Cristoforetti, F. Di Renzo, and L. Scorzato. “High density QCD on a Lefschetz thimble?” *Phys. Rev. D* 86 (2012), 074506. arXiv: 1205.3996.

[102] M. Cristoforetti et al. *PoS LATTICE2013* 197 (2014).

[103] M. Cristoforetti et al. *Phys. Rev. D* 89 (2014), 114505.

[104] F. Di Renzo and G. Eruzzi. *Phys. Rev. D* 92 (2015), 085030.

[105] A. Mukherjee, M. Cristoforetti, and L. Scorzato. *Phys. Rev. D* 88 (2013), 051502.

[106] H. Fujii, S. Kamata, and Y. Kikukawa. *JHEP* 12 (2015), 125.

[107] K. Fukushima and Y. Tanizaki. *PTEP 2015* 111A01 (2015).

[108] A. Alexandru, G. Basar, and P. F. Bedaque. *Phys. Rev. D* 93 (2016), 014504.

[109] A. Mukherjee and M. Cristoforetti. *Phys. Rev. B* 90 (2014), 035134.

[110] A. Alexandru et al. *JHEP* 05 (2016), 053.

[111] J. Nishimura and S. Shimasaki. *JHEP* 06 (2017), 023.

[112] A. Alexandru et al. *Phys. Rev. D* 96 (2017), 094505. arXiv: arXiv:1709.01971.

[113] Y. Tanizaki, H. Nishimura, and Jacobus J.M. Verbaarschot. *JHEP* 100 (2017), 1710. DOI: 10.1007/JHEP10(2017)100. arXiv: arXiv:1706.03822.

[114] Y. Mori, K. Kashiwa, and A. Ohnishi. *Phys. Rev. D* 96 (2017), 111501. arXiv: arXiv:1705.05605.

[115] Y. Mori, K. Kashiwa, and A. Ohnishi. *KUNS-2704, YITP-17-98* (2017). arXiv: arXiv:1709.03208.

[116] A. Alexandru et al. *Phys. Rev. D* 95 (2017), 014502.

[117] Y. Tanizaki, Y. Hidaka, and T. Hayata. *New. J. Phys.* 18 (2016), 033002.

[118] M. Fukuma and N. Umeda. *KUNS-2666* (2017). arXiv: arXiv:1703.00861.

[119] A. Alexandru et al. *Phys. Rev. D* 96 (2017), 034513.

[120] P. V. Buividovich and M. I. Polikarpov. *Phys. Rev. B* 86 (2012), 245117.

[121] M. V. Ulybyshev et al. *Phys. Rev. Lett.* 111 (2013), 056801.

[122] D. Smith and L. von Smekal. *Phys. Rev. B* 89 (2014), 195429.

[123] J. E. Hirsh. *Phys. Rev. B* 28 (1983), 4059.

[124] J. E. Hirsh. *Phys. Rev. B* 31 (1985), 4403.

[125] T. Schäfer et al. *Phys. Rev. B* 91 (2015), 125109.

[126] D. Rost et al. *Phys. Rev. B* 86 (2012), 155109.

[127] P. V. Buividovich and M. V. Ulybyshev. *Int. J. Mod. Phys. A* 31 (2016), 1643008.

[128] M. Hohenadler et al. *Phys. Rev. B* 90 (2014), 085146.

[129] M. V. Ulybyshev, C. Winterowd, and S. Zafeiropoulos. *Phys. Rev. B* 96 (2017), 205115.

[130] M. Körner et al. *Phys. Rev. B* 96 (2017), 195408.

[131] C. Wu and S. C. Zhang. *Phys. Rev. B* 71 (2005), 155115.

[132] S. R. White, R. L. Sugar, and R. T. Scalettar. *Phys. Rev. B* 38 (1988), 11665.

[133] S. Beyl, F. Goth, and F. Assaad. *Phys. Rev. B* 97 (2018), 085144. arXiv: arXiv:1708.03661.

[134] T. DeGrand and C. DeTar. *Latice methods for quantum chromodynamics*. World Scientific, 2006.

[135] M. V. Ulybyshev and M. I. Katsnelson. *Phys. Rev. Lett.* 114 (2015), 246801.

[136] I. Lifshitz. *Sov. Phys. JETP* 11 (1960), 1130.

[137] T. O. Wehling et al. *Phys. Rev. Lett.* 106 (2011), 236805.

[138] R. Blankenbecler, D. J. Scalapino, and R. L. Sugar. *Phys. Rev. D* 24 (1981), 2278.

[139] P. V. Buividovich and M. V. Ulybyshev. "Numerical study of chiral plasma instability within the classical statistical field theory approach". *Phys. Rev. D* 94 (2016), 025009. arXiv: 1509.02076.

[140] N. Yamamoto. "Chiral Shock Waves". *Phys.Rev.Lett.* 118 (2017), 181601. arXiv: 1609.07030.

[141] N. Tanji, N. Mueller, and J. Berges. "Transient anomalous charge production in strong-field QCD". *Phys. Rev. D* 93 (2016), 074507. arXiv: 1603.03331.

[142] N. Mueller, S. Schlichting, and S. Sharma. "Chiral magnetic effect and anomalous transport from real-time lattice simulations". *Phys. Rev. Lett.* 117 (2016), 142301. arXiv: 1606.00342.

[143] M. Creutz, I. Horvath, and H. Neuberger. "A new fermion Hamiltonian for lattice gauge theory". *Nucl.Phys.Proc.Suppl.* 106 (2002), 760–762. arXiv: hep-lat/0110009.

[144] D. E. Kharzeev and H.-U. Yee. “Chiral Magnetic Wave”. *Phys. Rev. D* 83 (2011), 085007. arXiv: 1012.6026.

[145] F. Gelis and N. Tanji. “Formulation of the Schwinger mechanism in classical statistical field theory”. *Phys. Rev. D* 87 (2013), 125035. arXiv: 1303.4633.

[146] V. Kasper, F. Hebenstreit, and J. Berges. “Fermion production from real-time lattice gauge theory in the classical-statistical regime”. *Phys. Rev. D* 90 (2014), 025016. arXiv: 1403.4849.

[147] M. H. Al-Hashimi and U.-J. Wiese. “Discrete Accidental Symmetry for a Particle in a Constant Magnetic Field on a Torus”. *Ann.Phys.* 324 (2009), 343–360. arXiv: 0807.0630.

[148] M. Ammon et al. “Holographic quenches and anomalous transport”. *JHEP* 09 (2016), 131. arXiv: 1607.06817.

[149] D. J. Gross and W. Taylor. “Two-dimensional QCD is a string theory”. *Nucl. Phys. B* 400 (1993), 181–208. arXiv: hep-th/9301068.

[150] Anees Ahmed and Gerald V. Dunne. “Non-perturbative large N trans-series for the Gross–Witten–Wadia beta function”. *Physics Letters B* 785 (2018), 342–346. arXiv: 1808.05236.

[151] M. Mace et al. “Non-equilibrium study of the Chiral Magnetic Effect from real-time simulations with dynamical fermions”. *Phys. Rev. D* 95 (2017), 036023. eprint: 1612.02477. URL: http://dx.doi.org/10.1103/PhysRevD.95.036023.

[152] E. W. Weisstein. *Halley’s Method.* From MathWorld–A Wolfram Web Resource. URL: http://mathworld.wolfram.com/HalleysMethod.html.